1999

Theoretical study of spin-orbit coupling in molecules

Dmitri G. Fedorov
Iowa State University

INFORMATION TO USERS

This manuscript has been reproduced from the microfilm master. UMI films the text directly from the original or copy submitted. Thus, some thesis and dissertation copies are in typewriter face, while others may be from any type of computer printer.

The quality of this reproduction is dependent upon the quality of the copy submitted. Broken or indistinct print, colored or poor quality illustrations and photographs, print bleedthrough, substandard margins, and improper alignment can adversely affect reproduction.

In the unlikely event that the author did not send UMI a complete manuscript and there are missing pages, these will be noted. Also, if unauthorized copyright material had to be removed, a note will indicate the deletion.

Oversize materials (e.g., maps, drawings, charts) are reproduced by sectioning the original, beginning at the upper left-hand corner and continuing from left to right in equal sections with small overlaps. Each original is also photographed in one exposure and is included in reduced form at the back of the book.

Photographs included in the original manuscript have been reproduced xerographically in this copy. Higher quality 6" x 9" black and white photographic prints are available for any photographs or illustrations appearing in this copy for an additional charge. Contact UMI directly to order.

UMI®

Bell & Howell Information and Learning
300 North Zeeb Road, Ann Arbor, MI 48106-1346 USA
800-521-0600

Theoretical study of spin-orbit coupling in molecules

by

Dmitri G. Fedorov

A dissertation submitted to the graduate faculty

in partial fulfillment of the requirements for the degree of

DOCTOR OF PHILOSOPHY

Major: Physical Chemistry

Major Professor: Mark S. Gordon

Iowa State University

Ames, Iowa

1999

Graduate College

Iowa State University

This is to certify that the Doctoral Dissertation of

Dmitri G. Fedorov

has met the dissertation requirements of Iowa State University

Signature was redacted for privacy.

Committee Member

Signature was redacted for privacy.

Committee Member

Signature was redacted for privacy.

Committee Member

Signature was redacted for privacy.

Committee Member

Signature was redacted for privacy.

Major Professor

Signature was redacted for privacy.

For the Major Program

Signature was redacted for privacy.

For the Graduate College

TABLE OF CONTENTS

GLOSSARY

AO, Atomic Orbitals. One-electron functions whose square is the density of an electron in centred on an atom.

CAS, Complete Active Space. A method to simultaneously optimise MOs and CI coeffcients of CSFs (or determinants) built upon these MOs. All occupations within a chosen space are considered (with the possible restriction imposed by symmetry).

CI, Configurational Interaction. Wavefunction composed of Slater determinants.

CSF, Configurational State Function. Spin-adapted (i.e. eigenfunction of $\hat{S}^2$ operator) linear combination of Slater determinants.

Discoincidence, a pair of Slater determinants that differ by one orbital (in each determinant). This orbital is said to be discoincident.

FOCI, First Order CI. Wavefunction composed of all single excitations from CAS into virtual space.

Hermiticity, Hermitian character of an operator.

Integral convention: physical, same as scalar product: $\langle ab|A|cd\rangle = a^\dagger b^\dagger Acd$.

Irrep, irreducible representation.

LCAO, Linear Combination of Atomic Orbitals. A generally used approach of expanding MOs in terms of linear combinations of AOs.

MO, Molecular Orbitals. One-electron functions whose square is the density of an electron in a molecule.

Scalar product convention: physical or Dirac $\langle a|b\rangle = a^\dagger b$.

SCF, Self Consistent Field Approach. The backbone of a very large class of modern quantum chemistry methods.

SOCI, Second Order CI. Wavefunction composed of all single and double excitations from CAS into the virtual space.

SOC, Spin-Orbit Coupling. A diabatic relativistic interaction of angular and spin momenta.

SOCC, Spin-Orbit Coupling Constant. Determines the magnitude of SOC between a pair of states.

ACKNOWLEDGMENTS

The helpful guidance of my scientific advisor is gratefully acknowledged. The uncountable answered questions and discussions with Michael Schmidt are greatly appreciated. Shiro Koseki, Kenneth Dyall, Peter Pyykkö and David Yarkony are thanked for their collaboration and scientific interaction. Thomas Furlani's providing the supplementary notes for his thesis proved to be very beneficial.

ABSTRACT

Theoretical models to study spin-obit coupling with multi-configurational wavefunctions have been developed both methodologically and implemented into the widely distributed quantum chemistry package GAMESS. Various aspects of making the spin-orbit coupling studies more efficient and thus more available, such as extensive usage of symmetry and parallelisation have been studied. A theoretical development of one, two and partial two electron approaches to spin-orbit coupling is given and tested on a representative set of molecules. A new accurate method to study the vibrational structure of molecules, limited in the current formulation to diatomics, has been proposed. Two chemically interesting systems have been studied, the reaction path of titanium cation and ethane, and the vibrational structure of CO^+ and O_2^+.

CHAPTER I. GENERAL INTRODUCTION

1. Introduction

One of the key ideas in the scientific approach of theoretical understanding of the natural phenomena is the art of making approximations. One can derive beautiful and completely general equations describing nature in its totality, however, it is perfectly clear that any finite expression represents a finite part of the infinite complexity of the natural phenomena. The general equations lack the ability to describe the phenomena exactly. Still, even the limited form of scientific wisdom expressed in many beautiful equations does not permit a general and exact solution to these equations to be found. One of the key wheels perpetuating scientific thought is the ability to make and break approximations. An approximation is only a first step intending to probe the bulk of the interaction. The second step necessarily is the understanding of under what conditions this approximation is applicable and what are the forces representing the breakdown of the approximation. Only then can one confidently use the approximation and break it when deemed important.

One of the pivotal approximations currently established in quantum chemistry is the adiabatic approximation that proved to be the fundamental step in the quantum theory permitting the transition from study of atomic structure into molecular studies. The basis of this approximation is the difference by a factor of 1837 in masses of electron and proton. This effectively establishes the independence of electronic and nuclear movement. This approximation proved to work exceptionally well, so that the majority of chemical phenomena can be described with sufficient accuracy. However, there are classes of chemical phenomena that do violate the approximation. They include photodissociation[1], charge transfer and in fact all chemical phenomena become increasingly affected by

relativistic effects as the atomic weight becomes heavier. These relativistic effects can be separated into scalar and spin-mixing parts[2]. The latter can be further separated into spin-spin and spin-orbit coupling parts and both belong to the realm of the interactions breaking the adiabatic approximation. Other important classes include Renner-Teller[3] and Jahn-Teller[4] effects.

This work will be concerned with the spin-orbit coupling interaction that can be derived as an approximation to the Dirac equation,, when one reduces the four-component Dirac equation into a two and then one component equation having the form of a Schrödinger equation with extra terms one of which represents the spin-orbit coupling[5].

An effect of spin-orbit coupling on adiabatic levels can be illustrated with the example of a $^2\Pi$ state of a linear molecule, as discussed in detail below (CO^+). An adiabatic spin-free calculation produces two degenerate energy levels, usually denoted by Π_x and $\Pi_y(M_L=\pm1)$. A doublet has two spin components, $M_s=\pm1/2$. Thus, there are four adiabatic levels. The diabatic coupling (SOC) lifts this four-fold degeneracy and produces two doubly degenerate levels, according to the angular momentum addition rule, since $M_J=M_L+M_S$ is a good quantum number ($\hat{J}_z$ commutes with the Hamiltonian) and one gets four values of $M_J=\pm1/2$ and $\pm3/2$. The M_J levels equal in absolute values and different by the sign represent the Kramer's time-reversal degeneracy[6] and are degenerate in energy. The coupling of levels is illustrated below:

$$\begin{bmatrix} E_{\Pi_x} & 0 & 0 & 0 \\ 0 & E_{\Pi_x} & 0 & 0 \\ 0 & 0 & E_{\Pi_y} & 0 \\ 0 & 0 & 0 & E_{\Pi_y} \end{bmatrix} \xrightarrow{\hat{H}_{so}} \begin{bmatrix} E_{\Pi_x} & \langle \Pi_x^{1/2}|\hat{H}_{so}|\Pi_x^{-1/2}\rangle & \langle \Pi_x^{1/2}|\hat{H}_{so}|\Pi_y^{1/2}\rangle & \langle \Pi_x^{1/2}|\hat{H}_{so}|\Pi_y^{-1/2}\rangle \\ \langle \Pi_x^{-1/2}|\hat{H}_{so}|\Pi_x^{1/2}\rangle & E_{\Pi_x} & \langle \Pi_x^{-1/2}|\hat{H}_{so}|\Pi_y^{1/2}\rangle & \langle \Pi_x^{-1/2}|\hat{H}_{so}|\Pi_y^{-1/2}\rangle \\ \langle \Pi_y^{1/2}|\hat{H}_{so}|\Pi_x^{1/2}\rangle & \langle \Pi_y^{1/2}|\hat{H}_{so}|\Pi_x^{-1/2}\rangle & E_{\Pi_y} & \langle \Pi_y^{1/2}|\hat{H}_{so}|\Pi_y^{-1/2}\rangle \\ \langle \Pi_y^{-1/2}|\hat{H}_{so}|\Pi_x^{1/2}\rangle & \langle \Pi_y^{-1/2}|\hat{H}_{so}|\Pi_x^{-1/2}\rangle & \langle \Pi_y^{-1/2}|\hat{H}_{so}|\Pi_y^{1/2}\rangle & E_{\Pi_y} \end{bmatrix}$$

Some of the matrix elements are zero by symmetry. In the case of linear molecules and Π terms, only the following must be calculated:

$$\begin{bmatrix} E_{\Pi_x} & 0 & A & 0 \\ 0 & E_{\Pi_x} & 0 & -A \\ A^* & 0 & E_{\Pi_y} & 0 \\ 0 & -A^* & 0 & E_{\Pi_y} \end{bmatrix} \quad \text{and} \quad A = \left\langle \Pi_x^{1/2} \middle| \hat{H}_{so} \middle| \Pi_y^{1/2} \right\rangle$$

The eigenvalues of the matrix are two doubly degenerate values: $E_{\pm}=E_{\Pi}\pm|A|$.

An important thing to notice here is the spin-orbit coupling splitting, defined as E_+-E_-; although it appears as a difference, in fact it is equal to 2|A|. Similarly, the spin-orbit coupling constant is defined as a sum of squares of matrix elements. Thus the spin-orbit coupling effects are fundamentally absolute in nature, that is they are not relative to something, with a sharp contrast to energy which is only defined up to a constant. This has a deep and profound effect upon practical finite precision calculations: energy requires high quality basis sets and large CI expansions in order to accurately describe energy splitting, whereas spin-orbit coupling itself as a correction does not require such computationally demanding resources.

So in this case the symmetry analysis allows one to reduce the amount of work required to one matrix element. This exemplifies the usefulness of a thorough symmetry analysis.

The eigenvalues of this H_{so} matrix represent the diabatic energy levels and the splitting between them (absent at the adiabatic level of theory). Although these effects are small (for light elements) they are large enough to be seen experimentally.

2. Dissertation Organisation

In Chapter II the existing and developed general approaches to calculating spin-orbit coupling interactions for molecules are given. In Chapter III a systematic study of the affects and uses of symmetry for spin-orbit coupling is conducted. In Chapters IV and V the

developed ability to conduct the study of spin-orbit coupling is further applied to the practical work directly linked to the chemical phenomena. Applications of spin-orbit coupling are given in Chapters VI and VII. The general conclusions are drawn in Chapter VIII.

Chapters I and VIII contain the introduction and conclusions, respectively. Chapters II, III, VI and VII are to submitted to journals. Chapters IV and V contain supplementary material used throughout the dissertation.

References

[1] J. Michl and V. Bonacic-Koutecky, Electronic aspects of organic photochemistry (Wiley, New York, 1990)

[2] K. Dyall, J. Chem. Phys, **100**, 2118 (1994)

[3] C. Jungen and A.J. Merer In Modern Spectroscopy: Modern research; Ed. by K.N. Rao (Academic, New York, 1976)

[4] I. B. Bersuker, The Jahn-Teller effect: a bibliographic review (Plenum, New York, 1984)

[5] H. A. Bethe, E. E. Salpeter, Quantum Mechanics of the one and two electron atoms (Plenum, New York, 1977).

[6] D.M.Brink and G.R.Satchler Angular Momentum (Charedon Press, Oxford, 1968)

CHAPTER II. A STUDY OF THE RELATIVE IMPORTANCE OF ONE AND TWO ELECTRON CONTRIBUTIONS TO SPIN-ORBIT COUPLING

A paper to be submitted to *J. Chem.. Phys.*

Dmitri G. Fedorov, Mark S. Gordon

Abstract

The existing methods to estimate the magnitude of spin-orbit coupling for arbitrary molecules and multi-configurational wavefunctions are reviewed. The form-factor method is extended from the original singlet-triplet formulation into arbitrary multiplicities. A simplified version of the mean-field method is formulated and tested versus the full two-electron operator on a set of representative molecules. The change of the one and two electron spin-orbit coupling down the Periodic Table is investigated.

1. Introduction

As computational capabilities improve, the ability to do more accurate calculations and study finer features of molecular structure is facilitated. One of the features that has begun to be widely studied relatively recently for molecules rather than atoms is spin-orbit coupling (SOC). It is one of several interactions violating the commonly used adiabatic approximation and as such, it provides valuable information about dynamics of processes otherwise forbidden (such as transitions at energy surface crossings). As a consequence of

relativistic effects, as can be seen directly from the reduction of the full relativistic Dirac equation, it provides a perturbative correction to the energy levels, generally growing with the nuclear charge. Whereas the general theoretical aspects of spin-orbit coupling have been known for a long time, there has been a lack of generally available tools with which it can be calculated.

In this work a general hierarchy of spin-orbit coupling methods is described. These methods have been developed and implemented into the electronic structure code GAMESS[1]. An approximate one-electron method developed by Koseki in GAMESS was previously described for both main group[2] and transition elements[3]. Veseth[4] and Ross *et al* [5] studied spin-orbit coupling for a number of atoms. Although full two-electron Pauli-Breit SOC calculations (vide infra) have been done by many researchers[6,7,18], their codes have not been generally available. As a result of the present work general SOC calculations can now be performed with GAMESS, as described below. Several advances in calculation methods have been made. The code is fully capable of running in parallel with TCGMSG[8] and MPI[9] libraries.

2. General description of the methods

The Pauli-Breit spin-orbit coupling operator is given by[10]:

$$\hat{H}_{so} = \frac{\Omega^2}{2}\left\{\sum_{i=1}^{N_{el}}\sum_{\alpha=1}^{N_{atom}}\frac{Z_\alpha}{\left|\bar{r}_i-\bar{r}_\alpha\right|^3}\left[\left(\bar{r}_i-\bar{r}_\alpha\right)\times\bar{p}_i\right]\bullet\bar{S}_i-\sum_{i=1}^{N_{el}}\sum_{j\neq i}^{N_{el}}\frac{1}{\left|\bar{r}_i-\bar{r}_j\right|^3}\left[\left(\bar{r}_i-\bar{r}_j\right)\times\bar{p}_i\right]\bullet\left[\bar{S}_i+2\bar{S}_j\right]\right\} \qquad (1)$$

where:

Ω is the fine structure constant,

Z_α are the nuclear charges,

r_i and r_α are the electron and nuclear coordinates respectively,

$\hat{p}_i$ is the electron momentum operator,

$\hat{S}_i$ is the electron spin operator.

The first double sum is known as the one and the second as the two-electron SOC operators. The computational expenses of SOC calculations are considerably different (by one order of magnitude) for one and two electron operators. In addition, due to the local nature of the operator and the explicit dependence of the one-electron operator upon the nuclear charges, the one-electron contribution to SOC tends to grow rapidly with the nuclear charge, whereas the two-electron part grows much more slowly, due to increased electron density in the regions close to the nuclei. This has motivated the development of several approaches wherein the complexity grows from just one-electron(1E) to the full one and two electron (2E) operators through an intermediate partial two-electron contribution method (P2E).

The following quantity based upon the Fermi Golden Rule is useful for the description of the dynamics of SOC-induced transitions (such as reaction dynamics).

$$C_{S,S'} \equiv \sum_{M_s=-S}^{S} \sum_{M'_s=-S'}^{S'} \left| \left\langle SM_s \left| \hat{H}_{so} \right| S'M'_s \right\rangle \right|^2 = \frac{2S+1}{3} \left\{ \left\langle S \left| \hat{\mathcal{L}}_x \right| S' \right\rangle^2 + \left\langle S \left| \hat{\mathcal{L}}_y \right| S' \right\rangle^2 + \left\langle S \left| \hat{\mathcal{L}}_y \right| S' \right\rangle^2 \right\} = \frac{2S+1}{3} \left\langle S \left| \hat{\mathcal{L}} \right| S' \right\rangle^2 \quad (2)$$

(Dirac notation is used throughout, $\hat{\mathcal{L}}$ denotes the molecular angular momentum operator, defined below). This quantity is hence called the SOC constant (SOCC). Note that S' is either equal to S or to S+1, so there is no real asymmetry in the formula. More details are given below.

Since the many modern quantum-chemical methods are based upon Slater determinants, with the total wavefunction being a linear combination thereof, the methods below are based on calculation of spin-orbit coupling matrix elements between two determinants. Spin-adapted linear combinations of determinants are known as CSFs. Two

different approaches can be taken. Given the total wavefunction and an operator $\hat{A}$, consider $\left\langle \Psi_1 \middle| \hat{A} \middle| \Psi_2 \right\rangle$:

- Direct approach ($|\Psi\rangle = \sum_I C_I \nu_I$ The individual matrix elements between two determinants or CSFs $\left\langle D_I \middle| \hat{A} \middle| D_J \right\rangle$ are calculated one by one using the Slater rules, which reduce a matrix element to a sum of MO integrals.
- Indirect approach $\left\langle \Psi_1 \middle| \hat{A} \middle| \Psi_2 \right\rangle = Tr[AP] = \sum_{i,j} A_{ij} P_{ji}$ or $\sum_{ijkl} A_{ijkl} P_{lkji}$ for 1 and 2 electron operators. Here, Ψ can be a single determinant, a CSF or their linear combination, A are integrals in the basis of MOs (i.e. $A_{ij} = \left\langle \varphi_i \middle| \hat{A} \middle| \varphi_j \right\rangle$) and P is the generalised density.

The advantage of the indirect method is that it does not require storing of the 2e integrals usually kept in memory in the direct method. The penalty for this advantage is having to calculate, sort and store the form-factors (vide infra), from which the generalised density is calculated. This effectively restricts the practical applicability of the indirect approach to the complete active space (CAS) type of wavefunction. Thus, the indirect method is best used with small active spaces and large basis sets, whereas the direct approach may not be able to handle large basis sets due to limited computer memory.

An intermediate method also exists, known as the symbolic matrix element method, wherein the CSFs are divided into classes according to occupation schemes, and each scheme is then treated with the indirect approach . While found to work well, this method is not considered below as its practical implementation requires an appropriate underlying configurational interaction (CI) scheme currently not available in GAMESS. The foregoing discussion is summarised in Table 1.

Except for computation of the full 1e and 2e matrix elements, the indirect approach is at a disadvantage compared with the direct method, so it has not been implemented for the

other approaches. The indirect one and two-electron operator approach requires exponentially growing resources as the number of active orbitals (i.e., all variably occupied orbitals) increases, so the actual implementation is still limited to 26 active orbitals at most (denoted by * in Table 1).

Table 1. Summary of SOC code development in GAMESS.

	In GAMESS originally			In GAMESS after this work		
	1E	P2E	2E	1E	P2E	2E
direct	general	none	none	general	general	general
indirect	none	none	limited	none	none	general(*)

Throughout this work, it is assumed that the two sets of molecular orbitals (MOs) (the sets for bra and ket) are biorthogonal with identical core (doubly occupied space in all configurations). It is only possible to biorthogonalise MO sets for a pair of multiplicities in the CAS case[11](or Full CI, FCI). In all other cases identical MO sets have to be used to avoid having to deal with non-orthogonal orbitals. In principle, it is possible to work with non-orthogonal orbitals[12], with the computational expense increased by an order of magnitude. Then a one-electron SOC non-orthogonal calculation would cost as much as a two-electron one with orthogonal orbitals.

3. Symmetry Summary

By application of the Wigner-Eckart theorem[13] and by using the hermiticity of $\hat{H}_{so}$, it is possible to reduce the number of matrix elements to be calculated from (2S+1)(2S'+1)

where S and S' are the bra and ket $\hat{S}^2$ eigenvalues, to at most two[14]. Application of symmetry selection rules can further reduce this number. It has been found that the double group does not offer any advantage over the point group formalism[14], if the matrix elements are calculated in the real-valued CI state basis. The matrix elements reduce to:

$$\left\langle \alpha\Gamma i S M_s \left| \hat{H}_{so} \right| \alpha'\Gamma' i' S' M_s' \right\rangle = \sum_{q=-1}^{1} (S', 1, M_s', -q \mid S, M_s) \left\langle \alpha\Gamma i S \left| \hat{\mathcal{L}}_q \hat{S} \right| \alpha'\Gamma' i' S' \right\rangle (-1)^q \tag{3}$$

where α, Γ and i are the symmetry labels of the CI states and $(S',1,M_s',q|S,M_s)$ is a Clebsch-Gordan coefficient. $\left\langle \alpha\Gamma i S \left| \hat{\mathcal{L}}_q \hat{S} \right| \alpha'\Gamma' i' S' \right\rangle$ is a so called reduced matrix element (RME), with the property that RME(q=1) and RME(q=-1) are connected by a simple relation, so that only two need to be explicitly calculated (e.g., q=0 and q=1). An important consequence of this formula is that for a pair of states (e.g., determinants) only one q in the above sum survives, namely $q=M_s'-M_s$.

The point group selection rules are deduced from the product $\Gamma \times \Gamma_{\mathcal{L}_q} \times \Gamma'$ of the irreducible representations, to which bra, angular momentum $\mathcal{L}_q$ and ket belong. Matrix elements between two singlets and for bra equal to ket (real-valued states) are zero.

It is worth keeping in mind that usually the CI states are not pure symmetry-wise, i.e. they belong to several irreducible representations with different weights, so the point group symmetry rules hold only approximately if a state is assumed to belong to only one of them.

Integral index permutational symmetry is discussed below when the integrals are defined for the indirect method.

4. Indirect Method

Furlani derived and coded a limited version of this method as a part of his PhD thesis[15]. The method itself was derived for singlet and triplet states only. The code was

limited to 10 active orbitals and up to d-functions.

Close examination of the derivations reveals that for the general case of arbitrary multiplicities the following holds for $\langle SM_s|\hat{H}_{so}|S'M_s'\rangle$:

- the matrix element is zero if $|S-S'|>1$ or $|M_s-M_s'|>1$
- if $M_s=M_s'$, then the formulae for singlet and triplet $M_s=0$ can be used to calculate such a matrix element
- if $M_s'-M_s=\pm1$, the formulae for singlet and triplet $Ms=\pm1$ are to be used.

A brief review of the generalised method is now given. Ψ is taken to be a linear combination of CSFs with coefficients q, each of which is a linear combination of Slater determinants Δ with coefficients C.

$$\left\langle \Psi(S,M_s)\middle|\hat{H}_{so}\middle|\Psi(S',M_s')\right\rangle = \sum_{I=1}^{N_{CSF}}\sum_{J=1}^{N'_{CSF}} q_I q_J' \sum_{K=1}^{N_{DET}}\sum_{L=1}^{N'_{DET}} C_K^{M_s} C_L^{M_s'} \left\langle \Delta_K^{M_s}\middle|\hat{H}_{so}\middle|\Delta_L^{M_s'}\right\rangle =$$

$$\sum_{I=1}^{N_{CSF}}\sum_{J=1}^{N'_{CSF}} q_I q_J \left\{ \sum_{i=1}^{N_a}\sum_{j=1}^{N_a} \Gamma_{ij}^{IJ} \left\langle \varphi_i^{M_s}\middle|\hat{l}_{so}^{(1)}\middle|\varphi_j^{M_s'}\right\rangle \prod_{\substack{k=1\\k\neq j}}^{N_e} \left\langle \varphi_{k(K)}^{M_s}\middle|\varphi_{k(L)}^{M_s'}\right\rangle - \sum_{i,j=1}^{N}\sum_{k,l=1}^{N} \Gamma_{ijkl}^{IJ} \left\langle \varphi_i^{M_s}\varphi_j^{M_s}\middle|\hat{l}_{so}^{(2)}\middle|\varphi_k^{M_s'}\varphi_l^{M_s'}\right\rangle \prod_{\substack{m=1\\m\neq j}}^{N_e} \left\langle \varphi_{m(K)}^{M_s}\middle|\varphi_{m(L)}^{M_s'}\right\rangle \right\} = \quad (4)$$

$$\sum_{i=1}^{N_a}\sum_{j=1}^{N_a} \Gamma_{ij}^{\Delta M_s} \left\langle \varphi_i^{M_s}\middle|\hat{l}_{so}^{(1)}\middle|\varphi_j^{M_s'}\right\rangle - \sum_{i,j=1}^{N}\sum_{k,l=1}^{N'} \Gamma_{ijkl}^{\Delta M_s} \left\langle \varphi_i^{M_s}\varphi_j^{M_s}\middle|\hat{l}_{so}^{(2)}\middle|\varphi_k^{M_s'}\varphi_l^{M_s'}\right\rangle$$

where $\hat{l}_{so}$ is what is left of the one and two electron spin-orbit coupling operators after taking the scalar product over the spin variables, k(L) denotes an orbital with ordinal number k in a determinant L. N is the total number of doubly occupied core (N_c) and active(N_a) orbitals, $N=2N_c+N_a$, N_e is the number of electrons in the active space, $\Delta M_s=M_s'-M_s(|\Delta M_s|\leq1)$.

The quantities Γ_{ij}^{IJ} and Γ_{ijkl}^{IJ} are known as the one and two-electron form-factors (FFs) (both are ΔM_s dependent), and $\Gamma_{ij}^{\Delta M_s}$ and $\Gamma_{ijkl}^{\Delta M_s}$ are the one and two-electron generalised density, respectively:

$$\Gamma_{ij}^{\Delta M_s} \equiv \sum_{I=1}^{N_{CSF}}\sum_{J=1}^{N'_{CSF}} q_I q_J \Gamma_{ij}^{IJ} \quad and \quad \Gamma_{ijkl}^{\Delta M_s} \equiv \sum_{I=1}^{N_{CSF}}\sum_{J=1}^{N'_{CSF}} q_I q_J \Gamma_{ijkl}^{IJ} \qquad (5)$$

The FFs are derived from application of the Slater rules to pairs of determinants Δ_K and Δ_I and comparison of the left and right hand sides.

The main properties of the form-factors are:

1. Γ_{ij}^{IJ} and Γ_{ijkl}^{IJ} are dependent only upon N_e and N_a and are sparse.
2. Γ_{ij}^{IJ} are zero unless both i and j are in the active space
3. Γ_{ijkl}^{IJ} are zero unless (i) all indices are in the active space or (ii) two indices are from the core and two from the active space (of which there are four combinations). In the latter case they are independent of the core indices[1] and are proptional to Γ_{ij}^{IJ}.

The MOs φ are taken as linear combination of atomic orbitals (AO) χ, and by using the index permutational symmetry the final result for the matrix element in Eq. (4) is:

$$\left\langle \Psi(S,M_s)\middle|\hat{H}_{so}\middle|\Psi(S',M_s')\right\rangle = \sum_{\gamma=1}^{N_{AO}}\sum_{\rho=1}^{\gamma-1}\sum_{\alpha=1}^{N_{atom}}\left\langle \chi_\gamma\middle|\hat{\ell}^{(1)}_{\Delta M_s}(1,\alpha)\middle|\chi_\rho\right\rangle \tilde{D}^1_{\gamma\rho} - \sum_{\gamma=1}^{N_{AO}}\sum_{\nu=1}^{N_{AO}}\sum_{\rho=1}^{\gamma-1}\sum_{\mu=1}^{\nu}\left\langle \chi_\gamma\chi_\nu\middle|\hat{\ell}^{(2)}_{\Delta M_s}\middle|\chi_\rho\chi_\mu\right\rangle \tilde{D}^2_{\gamma\nu\rho\mu} \quad (6)$$

$$\text{where} \quad \hat{\ell}^{(1)}_{\Delta M_s}(i,\alpha) = \frac{Z_\alpha}{\left|\bar{r}_i-\bar{r}_\alpha\right|^3}\left[\left(\bar{r}_i-\bar{r}_\alpha\right)\times\bar{p}_i\right]_{\Delta M_s}, \qquad \hat{\ell}^{(2)}_{\Delta M_s}(i,j) = \frac{1}{\left|\bar{r}_i-\bar{r}_j\right|^3}\left[\left(\bar{r}_i-\bar{r}_j\right)\times\bar{p}_i\right]_{\Delta M_s} \quad \text{and}$$

$$\begin{aligned} &\hat{\ell}^{(1)}_q(i) \equiv \sum_\alpha \hat{\ell}^{(1)}_q(i,\alpha), \quad \hat{\ell}^{(1)}_q \equiv \hat{\ell}^{(1)}_q(1), \quad \hat{\ell}^{(2)}_q \equiv \hat{\ell}^{(2)}_q(1,2) \\ &\hat{L}_q \equiv \hat{L}^{(1)}_q + \hat{L}^{(2)}_q, \quad \hat{L}^{(1)}_q \equiv \sum_i \hat{\ell}^{(1)}_q(i), \quad \hat{L}^{(2)}_q \equiv \sum_{i\neq j}\hat{\ell}^{(2)}_q(i,j) \end{aligned} \quad (7)$$

Note that for atoms $\hat{L}_q = \hat{L}^{(1)}_q$, where $\hat{L}_q$ is the total electronic angular momentum.

$$D^a_{\gamma\rho} \equiv \sum_{i,j=1}^{N_a}\Gamma_{ij}^{\Delta M_s} c^{M_s}_{\gamma i} c^{M_s'}_{\rho j}, \quad \tilde{D}^1 = D^a - D^{a\dagger}, \quad D^c_{\gamma\rho} \equiv \sum_{i,j=1}^{N_c} c_{\gamma i}c_{\rho j}, \quad B_{\gamma\nu\rho\mu} \equiv \sum_{i,j,k,l=1}^{N_a}\Gamma_{ijkl}^{\Delta M_s} c^{M_s}_{\gamma i} c^{M_s}_{\nu j} c^{M_s'}_{\rho k} c^{M_s'}_{\mu l}$$

$$\tilde{D}^2_{\gamma\nu\rho\mu} = \frac{1}{1+\delta_{\nu\mu}}\left[4D^c_{\nu\mu}\tilde{D}^1_{\gamma\rho} + 3D^c_{\gamma\nu}\tilde{D}^1_{\rho\mu} + 3D^c_{\nu\rho}\tilde{D}^1_{\mu\gamma} + 3D^c_{\gamma\mu}\tilde{D}^1_{\rho\nu} + 3D^c_{\mu\rho}\tilde{D}^1_{\nu\gamma} + B_{\gamma\nu\rho\mu} + B_{\gamma\mu\rho\nu} - B_{\rho\nu\gamma\mu} - B_{\rho\mu\gamma\nu}\right] \quad (8)$$

(following Furlani's convention with a few extra definitions for use below).

---

[1] Note: this is analogous to the direct method: these core-active form-factors correspond to the partial two-electron direct method considered below.

The c are MO→AO expansion coefficients for the active orbitals; c without superscript refers to the core orbitals (assumed to be independent of M_s). The superscripts "c" and "a" refers to core and active, respectively. Rapidly growing computational expenses can be seen in Table 2.

Table 2. The rapidly growing number of FFs.

CAS [m/n]	# singlet CSFs	# triplet CSFs	# 1e FFs	# 2e FFs	FF disk, bytes
[2/2]	3	1	8	16	192
[4/4]	20	15	320	2,896	76,800
[6/6]	175	51	3368	78,810	6,693,488
[8/8]	1764	2352	294370	12,282,038	232,448,352
[10/10]	19074	29700	8214402	536,127,134	4,656,497,344

[m/n] denotes m electrons in n orbitals.

It should be noted that the FFs are first generated and then sorted by MO indices. The number of FFs for a given set of MO indices is not known a priori, but the code has to allocate space before the generation starts. This can be done in two ways. One is to allocate a sufficiently large amount of space, however this increases the size of the disk file. Another option is to first generate the form factors and save the number of form factors for each set of indices while not saving the FFs themselves. Then the proper space is allocated and during the second run the FFs are actually generated and sorted. In Table 2 the last line ([10/10]) shows the disk space associated with the second (disk saving) option; all other lines reflect the fixed space option.

5. Direct methods

a) Introductory definitions

Similarly to the indirect case(Eq. 4),

$$\left\langle \Psi(S,M_s)\middle|\hat{H}_{so}\middle|\Psi(S',M_s')\right\rangle = \sum_{I=1}^{N_{CSF}}\sum_{J=1}^{N'_{CSF}} q_I q'_J \sum_{K=1}^{N_{DET}}\sum_{L=1}^{N'_{DET}} C_K C'_L \left\langle \Delta_K\middle|\hat{H}_{so}\middle|\Delta'_L\right\rangle \tag{9}$$

The Slater rules are now applied dynamically, for each pair of determinants. While there may be a very large number of them, it has to be recognised that for large CI expansions many products of CSF coefficients will be very small in magnitude. Keeping in mind that these coefficients themselves are obtained with finite precision, one is justified in omitting contributions from such very small coefficients. This is achieved via introduction of a threshold value; the details are given below.

First, consider the basic schematic equation:

$$\left\langle \Delta\middle|\hat{H}_{so}\middle|\Delta'\right\rangle = H^{1e}_{act-act} + H^{2e}_{core-act} + H^{2e}_{act-act} \tag{10}$$

($H^{1e}_{core-core} + H^{1e}_{core-act} + H^{2e}_{core-core}$ is zero as shown below). The three indirect methods can be defined as follows:

One-electron method: $\left\langle \Delta\middle|\hat{H}_{so}\middle|\Delta'\right\rangle = H^{1e}_{act-act}$

Partial two-electron method: $\left\langle \Delta\middle|\hat{H}_{so}\middle|\Delta'\right\rangle = H^{1e}_{act-act} + H^{2e}_{core-act}$

Two-electron method: $\left\langle \Delta\middle|\hat{H}_{so}\middle|\Delta'\right\rangle = H^{1e}_{act-act} + H^{2e}_{core-act} + H^{2e}_{act-act}$

It is shown below that $H^{2e}_{core-act}$ becomes pseudo-one-electron after summing over the core. The exact algebraic definitions of all of these quantities are given below. The one-electron method is usually implemented by introducing semi-empirical parameters (charges),

Z_{eff}, in order to make up for the neglect of the two-electron terms. It is shown below that the partial two-electron method provides reasonable accuracy without the need for fitted parameters.

Recall the Slater rules for a pair of determinants. First, the spin-orbitals in the second determinant are reordered in such a way as to put them in the same order as the first determinant, with different (discoincident) orbitals being placed at the end. The number of these discoincident orbitals needs to be less than or equal to the number of coupled particles in the operator (i.e., one or two), for a matrix element to be non-zero. For the partial two-electron method (P2E) the number of discoincidences should be less than or equal to one, because two discoincidences can only come from two active orbitals and this term is omitted in the P2E method. The cases for 0, 1, and 2 discoincidences are given below (note that only one spin-discoincidence is allowed, as the spin operators couple only one electron):

$$\begin{aligned}
\left\langle \Delta \middle| \hat{H}_{so} \middle| \Delta \right\rangle &= \sum_{\mu=1}^{N_e} \left\langle \psi_\mu \middle| \hat{h}_{so}^1 \middle| \psi'_\mu \right\rangle O_\mu + \sum_{\mu,\nu=1}^{N_e} \left[\left\langle \psi_\mu \psi_\nu \middle| \hat{h}_{so}^2 \middle| \psi'_\mu \psi'_\nu \right\rangle + \left\langle \psi_\nu \psi_\mu \middle| \hat{h}_{so}^2 \middle| \psi'_\nu \psi'_\mu \right\rangle - \left\langle \psi_\mu \psi_\nu \middle| \hat{h}_{so}^2 \middle| \psi'_\nu \psi'_\mu \right\rangle - \left\langle \psi_\nu \psi_\mu \middle| \hat{h}_{so}^2 \middle| \psi'_\mu \psi'_\nu \right\rangle \right] O_{\mu\nu} \\
\left\langle \Delta^\nu \middle| \hat{H}_{so} \middle| \Delta^\sigma \right\rangle &= \left\langle \psi_\nu \middle| \hat{h}_{so}^1 \middle| \psi'_\sigma \right\rangle O_\nu + \sum_{\mu=1}^{N_e} \left[\left\langle \psi_\mu \psi_\nu \middle| \hat{h}_{so}^2 \middle| \psi'_\mu \psi'_\sigma \right\rangle + \left\langle \psi_\nu \psi_\mu \middle| \hat{h}_{so}^2 \middle| \psi'_\sigma \psi'_\mu \right\rangle - \left\langle \psi_\mu \psi_\nu \middle| \hat{h}_{so}^2 \middle| \psi'_\sigma \psi'_\mu \right\rangle - \left\langle \psi_\nu \psi_\mu \middle| \hat{h}_{so}^2 \middle| \psi'_\mu \psi'_\sigma \right\rangle \right] O_{\mu\nu} \\
\left\langle \Delta^{\mu\nu} \middle| \hat{H}_{so} \middle| \Delta^{\rho\sigma} \right\rangle &= \left[\left\langle \psi_\mu \psi_\nu \middle| \hat{h}_{so}^2 \middle| \psi'_\rho \psi'_\sigma \right\rangle + \left\langle \psi_\nu \psi_\mu \middle| \hat{h}_{so}^2 \middle| \psi'_\sigma \psi'_\rho \right\rangle - \left\langle \psi_\mu \psi_\nu \middle| \hat{h}_{so}^2 \middle| \psi'_\sigma \psi'_\rho \right\rangle - \left\langle \psi_\nu \psi_\mu \middle| \hat{h}_{so}^2 \middle| \psi'_\rho \psi'_\sigma \right\rangle \right] O_{\mu\nu}
\end{aligned} \tag{11}$$

Orbital overlaps $O_\mu \equiv \prod_{\nu \neq \mu}^{N_e} \left\langle \psi_\nu \middle| \psi'_\nu \right\rangle$ and $O_{\mu\nu} \equiv \prod_{\rho \neq \nu,\mu}^{N_e} \left\langle \psi_\rho \middle| \psi'_\rho \right\rangle$ do not include core overlaps equal to one. By convention, the Greek indices are used for molecular spin-orbitals $\psi=\varphi\sigma$ and Roman indices for molecular orbitals φ. Greek indices are also used for atomic orbitals. Δ^ν and Δ^σ denote determinants different by one spin-orbital (ν and σ).

It is worth remembering that SOC between two identical states is zero by hermiticity, therefore in case of orthogonal (rather than biorthogonal) orbitals for bra and ket states the case of zero discoincidence need not be concerned with because the contribution vanishes by symmetry.

b) Spin summation

From the symmetry rules it is seen that only one specific q survives from the sum (Eq. 3), i.e., $\hat{h}_{so} \rightarrow \hat{l}_q \hat{s}_q$ where q=M_s'-M_s for a matrix element <$SM_s|\hat{H}_{so}|S'M_s'$>. Each spin-orbital (with a Greek index) is now written as a product of an orbital times the spin function σ (α or β), and the summation index is changed to Roman to signify this. It is then possible to take scalar products over the spin variables. The equations are simplified considerably, especially for the core orbitals.

The following elementary form-factors are introduced as matrix elements of spin-operators in the spin-function basis (σ_i denotes the spin part of i-th orbital). These elementary form-factors are similar to the form-factors Γ introduced for the indirect method except that they effectively connect two determinants rather than CSFs and γ are unsorted.

$$\gamma_{ij}^{\Delta M_s} \equiv \left\langle \sigma_i \middle| \hat{s}_{-\Delta M_s} \middle| \sigma_j \right\rangle$$
$$\gamma_{ijkl}^{\Delta M_s} \equiv \left\langle \sigma_i(1)\sigma_j(2) \middle| \{\hat{s}(1)+2\hat{s}(2)\}_{-\Delta M_s} \middle| \sigma_k(1)\sigma_l(2) \right\rangle = \left\langle \sigma_i \middle| \hat{s}_{-\Delta M_s} \middle| \sigma_k \right\rangle \delta_{jl} + 2\left\langle \sigma_j \middle| \hat{s}_{-\Delta M_s} \middle| \sigma_l \right\rangle \delta_{ik} = \gamma_{ik}^{\Delta M_s} \delta_{jl} + 2\gamma_{jl}^{\Delta M_s} \delta_{ik} \tag{12}$$

They are straightforward to calculate, e.g.

$$\gamma_{\alpha\alpha}^{0} \equiv \left\langle \alpha \middle| \hat{s}_z \middle| \alpha \right\rangle = 1/2$$
$$\gamma_{\alpha\beta\alpha\alpha}^{1} \equiv \left\langle \alpha(1)\beta(2) \middle| \hat{s}_-(1) + 2\hat{s}_-(2) \middle| \alpha(1)\alpha(2) \right\rangle = \left\langle \alpha \middle| \hat{s}_- \middle| \alpha \right\rangle \left\langle \beta \middle| \alpha \right\rangle + 2\left\langle \alpha \middle| \alpha \right\rangle \left\langle \beta \middle| \hat{s}_- \middle| \alpha \right\rangle = 0 + 2 = 2$$

There are only 16 of these for each ΔM_s, for ΔM_s=0, see Table 3.

Consider the one-electron case for zero discoincidence. ΔM_s is 0 in this case, so $\gamma_{\alpha\alpha}^{0} = -\gamma_{\beta\beta}^{0} = 1/2$ and

$$\begin{aligned} H_{core-core}^{1e} &= \sum_{\mu=1}^{N_c} \left\langle \psi_\mu \middle| \hat{h}_{so}^1 \middle| \psi_\mu' \right\rangle O_\mu = \sum_{i=1}^{N_c} \left[\left\langle \varphi_i \alpha \middle| \hat{\ell}_z^1 \hat{s}_z \middle| \varphi_i' \alpha \right\rangle O_i + \left\langle \varphi_i \beta \middle| \hat{\ell}_z^1 \hat{s}_z \middle| \varphi_i' \beta \right\rangle O_i \right] \\ &= \sum_{i=1}^{N_c} \left[\frac{1}{2} \left\langle \varphi_i \middle| \hat{\ell}_z^1 \middle| \varphi_i' \right\rangle O_i - \frac{1}{2} \left\langle \varphi_i \middle| \hat{\ell}_z^1 \middle| \varphi_i' \right\rangle O_i \right] = 0 \end{aligned} \tag{13}$$

Table 3. Complete $\gamma^0_{\mu\nu\rho\sigma}$ table.

	|αα>	|αβ>	|βα>	|ββ>
<αα|	3/2	1/2	1	0
<αβ|	1/2	-1/2	0	-1
<βα|	1	0	1/2	-1/2
<ββ|	0	-1	-1/2	-3/2

Thus, any doubly-occupied orbital (including **all** core orbitals) does not contribute to the one-electron spin-orbit coupling term. Similarly, the two-electron core-core contribution vanishes. $H^{1e}_{core-act} = 0$ because overlaps between core and active orbitals $<\varphi_c|\varphi_a>=0$.

The following integral quantities are introduced:

$$A_{ij} \equiv \left\langle \varphi_i \middle| \hat{\ell}^{(1)}_{\Delta M_s} \middle| \varphi'_j \right\rangle, \quad A_{ijkl} \equiv \left\langle \varphi_i \varphi_j \middle| \hat{\ell}^{(2)}_{\Delta M_s} \middle| \varphi'_k \varphi'_l \right\rangle$$

$$A^{caca}_{ij} \equiv \sum_{c=1}^{N_c} \left\langle \varphi_c \varphi_i \middle| \hat{\ell}^{(2)}_{\Delta M_s} \middle| \varphi_c \varphi'_j \right\rangle, \quad A^{acac}_{ij} \equiv \sum_{c=1}^{N_c} \left\langle \varphi_i \varphi_c \middle| \hat{\ell}^{(2)}_{\Delta M_s} \middle| \varphi'_j \varphi_c \right\rangle \tag{14}$$

$$A^{caac}_{ij} \equiv \sum_{c=1}^{N_c} \left\langle \varphi_c \varphi_i \middle| \hat{\ell}^{(2)}_{\Delta M_s} \middle| \varphi'_j \varphi_c \right\rangle, \quad A^{acca}_{ij} \equiv \sum_{c=1}^{N_c} \left\langle \varphi_i \varphi_c \middle| \hat{\ell}^{(2)}_{\Delta M_s} \middle| \varphi_c \varphi'_j \right\rangle$$

The superscripts c and a refer to core and active spaces, respectively.

Symmetry properties of the integrals are:

$$A_{ij} = -A_{ji}$$
$$A_{ijkl} = -A_{kjil} \quad and \quad A_{ijkl} = A_{ilkj} \tag{15}$$

(i.e. antisymmetric and symmetric for the first and second particle, respectively). This property holds for core integrals, too, so $A^{caca}_{ij} \equiv 0$.

In the code, $\hat{\ell}_{\pm}$ operators (defined as in the indirect case) are written as $\mp\left(\hat{\ell}_x \pm \hat{\ell}_y\right)/\sqrt{2}$, and the program actually calculates matrix elements of -i $\hat{\ell}_x$, -i $\hat{\ell}_y$ and -i $\hat{\ell}_z$ operators (multiplied by imaginary unity i to get real-valued integrals, as **l**=[**r** x **p**] and **p**=-i∇. Note that ∇ is antihermitian, whereas **p** is Hermitian). Subsequently, $\hat{\ell}_{\pm}$ are reconstructed.

It is possible to rewrite the matrix elements as:

$$\begin{aligned}
\left\langle \Delta \middle| \hat{H}_{so} \middle| \Delta \right\rangle &= \sum_{i=1}^{N_a} A_{ii}\gamma_{ii}^{\Delta M_s} O_i + 2\sum_{i=1}^{N_a} \left\{ \begin{array}{l} A_{ii}^{caca}\left[\gamma_{\alpha i\alpha i}^{\Delta M_s} + \gamma_{\beta i\beta i}^{\Delta M_s}\right] + A_{ii}^{acac}\left[\gamma_{i\alpha i\alpha}^{\Delta M_s} + \gamma_{i\beta i\beta}^{\Delta M_s}\right] - \\ A_{ii}^{caac}\left[\gamma_{\alpha ii\alpha}^{\Delta M_s} + \gamma_{\beta ii\beta}^{\Delta M_s}\right] - A_{ii}^{acca}\left[\gamma_{i\alpha\alpha i}^{\Delta M_s} + \gamma_{i\beta\beta i}^{\Delta M_s}\right] \end{array} \right\} O_i \\
&+ \sum_{i,j=1}^{N_a} \left[A_{ijij}\gamma_{ijij}^{\Delta M_s} + A_{jiji}\gamma_{jiji}^{\Delta M_s} - A_{ijji}\gamma_{ijji}^{\Delta M_s} - A_{jiij}\gamma_{jiij}^{\Delta M_s}\right] O_{ij} \\
\left\langle \Delta^j \middle| \hat{H}_{so} \middle| \Delta^l \right\rangle &= A_{jl}\gamma_{jl}^{\Delta M_s} O_j + \left\{ \begin{array}{l} A_{jl}^{caca}\left[\gamma_{\alpha j\alpha l}^{\Delta M_s} + \gamma_{\beta j\beta l}^{\Delta M_s}\right] + A_{jl}^{acac}\left[\gamma_{j\alpha l\alpha}^{\Delta M_s} + \gamma_{j\beta l\beta}^{\Delta M_s}\right] - \\ A_{jl}^{caac}\left[\gamma_{\alpha jl\alpha}^{\Delta M_s} + \gamma_{\beta jl\beta}^{\Delta M_s}\right] - A_{\nu\sigma}^{acca}\left[\gamma_{j\alpha\alpha l}^{\Delta M_s} + \gamma_{j\beta\beta l}^{\Delta M_s}\right] \end{array} \right\} O_j \\
&+ \sum_{i=1}^{N_c} \left[A_{ijil}\gamma_{ijil}^{\Delta M_s} + A_{jili}\gamma_{jili}^{\Delta M_s} - A_{ijli}\gamma_{ijli}^{\Delta M_s} - A_{jiil}\gamma_{jiil}^{\Delta M_s}\right] O_{il} \\
\left\langle \Delta^{ij} \middle| \hat{H}_{so} \middle| \Delta^{kl} \right\rangle &= \left[A_{ijkl}\gamma_{ijkl}^{\Delta M_s} + A_{jilk}\gamma_{jilk}^{\Delta M_s} - A_{ijlk}\gamma_{ijlk}^{\Delta M_s} - A_{jikl}\gamma_{jikl}^{\Delta M_s}\right] O_{ij}
\end{aligned} \tag{16}$$

Note that a factor of 2 appears because of symmetry in sums:

$$\sum_{i=1}^{N_c}\sum_{j=1}^{N_c} \rightarrow \sum_{i=1}^{N_a}\sum_{j=1}^{N_c} + \sum_{i=1}^{N_c}\sum_{j=1}^{N_a} = 2\sum_{i=1}^{N_a}\sum_{j=1}^{N_c}$$

With a little algebra it can be seen that:

$$\begin{aligned}
\gamma_{\alpha i\alpha j}^{\Delta M_s} + \gamma_{\beta i\beta j}^{\Delta M_s} &= 4\gamma_{ij}^{\Delta M_s} \\
\gamma_{i\alpha j\alpha}^{\Delta M_s} + \gamma_{i\beta j\beta}^{\Delta M_s} &= 2\gamma_{ij}^{\Delta M_s} \\
\gamma_{\alpha ij\alpha}^{\Delta M_s} + \gamma_{\beta ij\beta}^{\Delta M_s} &= 3\gamma_{ij}^{\Delta M_s} \\
\gamma_{i\alpha\alpha j}^{\Delta M_s} + \gamma_{i\beta\beta j}^{\Delta M_s} &= 3\gamma_{ij}^{\Delta M_s}
\end{aligned} \tag{17}$$

Thus the expressions for the matrix elements are simplified to (using $A_{ij}^{caca} \equiv 0$) :

$$\left\langle \Delta \middle| \hat{H}_{so} \middle| \Delta \right\rangle = \sum_{i=1}^{N_a} \left\{ A_{ii} \gamma_{ii}^{\Delta M_s} O_i + 2\left(A_{ii}^{acac} 2\gamma_{ii}^{\Delta M_s} O_i - A_{ii}^{caac} 3\gamma_{ii}^{\Delta M_s} O_i - A_{ii}^{acca} 3\gamma_{ii}^{\Delta M_s} O_i \right) \right\}$$
$$+ \sum_{i,j=1}^{N_a} \left[A_{ijij} \gamma_{ijij}^{\Delta M_s} + A_{jiji} \gamma_{jiji}^{\Delta M_s} - A_{ijji} \gamma_{ijji}^{\Delta M_s} - A_{jiij} \gamma_{jiij}^{\Delta M_s} \right] O_{ij}$$
$$\left\langle \Delta^j \middle| \hat{H}_{so} \middle| \Delta^l \right\rangle = A_{jl} \gamma_{jl}^{\Delta M_s} O_j + A_{jl}^{acac} 2\gamma_{jl}^{\Delta M_s} O_j - A_{jl}^{caac} 3\gamma_{jl}^{\Delta M_s} O_j - A_{jl}^{acca} 3\gamma_{jl}^{\Delta M_s} O_j \qquad (18)$$
$$+ \sum_{i=1}^{N_a} \left[A_{ijil} \gamma_{ijil}^{\Delta M_s} + A_{jili} \gamma_{jili}^{\Delta M_s} - A_{ijli} \gamma_{ijli}^{\Delta M_s} - A_{jiil} \gamma_{jiil}^{\Delta M_s} \right] O_{il}$$
$$\left\langle \Delta^{ij} \middle| \hat{H}_{so} \middle| \Delta^{kl} \right\rangle = \left[A_{ijkl} \gamma_{ijkl}^{\Delta M_s} + A_{jilk} \gamma_{jilk}^{\Delta M_s} - A_{ijlk} \gamma_{ijlk}^{\Delta M_s} - A_{jikl} \gamma_{jikl}^{\Delta M_s} \right] O_{ij}$$

and finally one arrives at the final formulæ:

$$\left\langle \Delta \middle| \hat{H}_{so} \middle| \Delta \right\rangle = \sum_{i=1}^{N_a} \left\{ A_{ii} \gamma_{ii}^{\Delta M_s} O_i + 2A_{ii}^{ca} \gamma_{ii}^{\Delta M_s} O_i \right\} + \sum_{i,j=1}^{N_a} \left[A_{ijij} \gamma_{ijij}^{\Delta M_s} + A_{jiji} \gamma_{jiji}^{\Delta M_s} - A_{ijji} \gamma_{ijji}^{\Delta M_s} - A_{jiij} \gamma_{jiij}^{\Delta M_s} \right] O_{ij}$$
$$\left\langle \Delta^j \middle| \hat{H}_{so} \middle| \Delta^l \right\rangle = A_{jl} \gamma_{jl}^{\Delta M_s} O_j + A_{jl}^{ca} \gamma_{jl}^{\Delta M_s} O_j + \sum_{i=1}^{N_a} \left[A_{ijil} \gamma_{ijil}^{\Delta M_s} + A_{jili} \gamma_{jili}^{\Delta M_s} - A_{ijli} \gamma_{ijli}^{\Delta M_s} - A_{jiil} \gamma_{jiil}^{\Delta M_s} \right] O_{il} \qquad (19)$$
$$\left\langle \Delta^{ij} \middle| \hat{H}_{so} \middle| \Delta^{kl} \right\rangle = \left[A_{ijkl} \gamma_{ijkl}^{\Delta M_s} + A_{jilk} \gamma_{jilk}^{\Delta M_s} - A_{ijlk} \gamma_{ijlk}^{\Delta M_s} - A_{jikl} \gamma_{jikl}^{\Delta M_s} \right] O_{ij}$$

where $A_{ij}^{ca} \equiv 2A_{ij}^{acac} - 3A_{ij}^{caac} - 3A_{ij}^{acca}$

Now it can be seen that the core-active two-electron contribution may be formally expressed in exactly the same fashion as one-electron active-active term.

$$H_{act-act}^{1e} = \sum_{i=1}^{N_a} A_{ii} \gamma_{ii}^{\Delta M_s} O_i$$
$$H_{core-act}^{2e} = 2\sum_{i=1}^{N_a} A_{ii}^{ca} \gamma_{ii}^{\Delta M_s} O_i \qquad (20)$$
$$H_{act-act}^{2e} = \sum_{i,j=1}^{N_a} \left[A_{ijij} \gamma_{ijij}^{\Delta M_s} + A_{jiji} \gamma_{jiji}^{\Delta M_s} - A_{ijji} \gamma_{ijji}^{\Delta M_s} - A_{jiij} \gamma_{jiij}^{\Delta M_s} \right] O_{ij}$$

for zero discoincidence and similarly for one and two discoincidences.

c) SOC integrals

The atomic integrals are calculated by the integral code developed by Furlani[15] for his form factor method (in the AO basis). The code has been slightly modified to allow up to g-type orbitals in the basis set.

The usage of AO integrals is different between direct and indirect methods. The indirect method is AO-integral based, i.e. each integral is multiplied by the density and added to the matrix element being calculated. The direct methods store the AO integrals on disk: the one-electron integrals are stored as a triangular matrix and the non-zero two-electron integrals are stored as an integral list, with orbital labels.

Transformation into the MO basis is accomplished for active orbitals in the standard way by doing two and four index transformations.

$$\begin{aligned} A_{ij} &\equiv \left\langle \varphi_i \middle| \hat{\ell}^{(1)}_{\Delta M_s} \middle| \varphi'_j \right\rangle = \sum_{\mu,\nu=1}^{N_{AO}} c^*_{\mu i} c'_{\nu j} \left\langle \chi_i \middle| \hat{\ell}^{(1)}_{\Delta M_s} \middle| \chi_j \right\rangle \\ A_{ijkl} &= \left\langle \varphi_i \varphi_j \middle| \hat{\ell}^{(2)}_{\Delta M_s} \middle| \varphi'_k \varphi'_l \right\rangle = \sum_{\mu\nu\rho\sigma}^{N_{AO}} c^*_{\mu i} c^*_{\nu j} c'_{\rho k} c'_{\sigma l} \left\langle \chi_i \chi_j \middle| \hat{\ell}^{(2)}_{\Delta M_s} \middle| \chi_k \chi_l \right\rangle \end{aligned} \tag{21}$$

where $c_{\mu i}$ are LCAO coefficients. The core-active transformations are reduced from four to two indices by doing the core summation:

$$\begin{aligned} A^{ca}_{ij} &\equiv 2A^{acac}_{ij} - 3A^{caac}_{ij} - 3A^{acca}_{ij} \\ &= 2\sum_{c=1}^{N_c} \left\langle \varphi_i \varphi_c \middle| \hat{\ell}^{(2)}_{\Delta M_s} \middle| \varphi'_j \varphi_c \right\rangle - 3\sum_{c=1}^{N_c} \left\langle \varphi_c \varphi_i \middle| \hat{\ell}^{(2)}_{\Delta M_s} \middle| \varphi'_j \varphi_c \right\rangle - 3\sum_{c=1}^{N_c} \left\langle \varphi_i \varphi_c \middle| \hat{\ell}^{(2)}_{\Delta M_s} \middle| \varphi_c \varphi'_j \right\rangle \\ &= \sum_{c=1}^{N_c} \sum_{\mu\nu\rho\sigma}^{N_{AO}} \left\{ 2c^*_{\mu i} c^*_{\nu c} c'_{\rho j} c_{\sigma c} - 3c^*_{\mu c} c^*_{\nu i} c'_{\rho j} c_{\sigma c} - 3c^*_{\mu i} c^*_{\nu c} c_{\rho c} c'_{\sigma j} \right\} \left\langle \chi_\mu \chi_\nu \middle| \hat{\ell}^{(2)}_{\Delta M_s} \middle| \chi_\rho \chi_\sigma \right\rangle \\ &= \sum_{\mu\nu\rho\sigma}^{N_{AO}} \left\{ 2D^c_{\nu\sigma} c^*_{\mu i} c'_{\rho j} - 3D^c_{\mu\sigma} c^*_{\nu i} c'_{\rho j} - 3D^c_{\nu\rho} c^*_{\mu i} c'_{\sigma j} \right\} A_{\mu\nu\rho\sigma} \end{aligned} \tag{22}$$

where the sum over the core yielded the core density, D^c.

$$A_{ij}^{ca} = 2\sum_{\mu\rho}^{N_{AO}} A_{\mu\rho}^{acac} c_{\mu i}^{*} c'_{\rho j} - 3\sum_{\nu\rho}^{N_{AO}} A_{\nu\rho}^{caac} c_{\nu i}^{*} c'_{\rho j} - 3\sum_{\mu\sigma}^{N_{AO}} A_{\mu\sigma}^{acca} c_{\mu i}^{*} c'_{\sigma j} = \sum_{\kappa\lambda}^{N_{AO}} c_{\kappa i}^{*} A_{\kappa\lambda}^{ca} c'_{\lambda j} \tag{23}$$

using the following notation:

$$A_{\mu\rho}^{acac} \equiv \sum_{\nu\sigma}^{N_{AO}} D_{\nu\sigma}^{c} A_{\mu\nu\rho\sigma}, \quad A_{\nu\rho}^{caac} \equiv \sum_{\mu\sigma}^{N_{AO}} D_{\mu\sigma}^{c} A_{\mu\nu\rho\sigma}, \quad A_{\mu\sigma}^{acca} \equiv \sum_{\nu\rho}^{N_{AO}} D_{\nu\rho}^{c} A_{\mu\nu\rho\sigma}$$
$$A_{\kappa\lambda}^{ca} \equiv 2A_{\kappa\lambda}^{acac} - 3A_{\kappa\lambda}^{caac} - 3A_{\kappa\lambda}^{acca} \tag{24}$$

Thus three four-index transformations are converted into three (to contract the core density) plus one (to contract active MO coefficients) two-index transformations, a considerable savings.

d) Effective Core Potentials (ECP)

In the effective core potential method, the core inner shell orbitals are replaced by a potential. The primary contribution to SOC comes from the one-electron part that does not explicitly include core orbitals. However, the shape of the active orbitals in the core region is lost in most ECP implementations, and this decreases the calculated spin-orbit coupling by orders of magnitude for heavier elements. Several approaches have been developed to cope with this problem:

a) Christiansen[16] developed a method wherein the operator itself is changed by utilising relativistic atomic calculations to obtain the effective one-electron spin-orbit coupling operator.

b) Model potentials (MP)[17] instead of ECPs do retain the proper shape in the core region.

c) By using two related basis sets, an all-electron and an ECP set, the integrals calculated for the all electron basis set can be back-transformed for the ECP basis set[18], thus circumventing the core shape problem.

d) Koseki et al[3] further developed an effective nuclear charge method, originally developed in Ref. 19 wherein the true nuclear charges appearing in the one-electron SOC operator are replaced by empirical parameters.

e) Empirical parameters

There are several reasons why it can be desirable to introduce some empirical parameters into the spin-orbit coupling calculations:

1. ECP produces incorrectly shaped orbitals.
2. The first-order perturbative treatment and the omission of other interactions (spin-spin) can be corrected to some extent.
3. In cases for which the two-electron contribution is either fully (1E) or partially (P2E) neglected, these approximations can be partially compensated by the empirical data.

The empirical parameters are optimised using the available atomic and molecular spectral data. The parameters for the first through the third rows of the Periodic Table are available for both ECP and an all-electron basis set[3], to be used with the one-electron method.

f) Thresholds

As pointed out above, thresholds avoid the calculation of very small contributions to SOC, thus saving computational time. One parameter controls all thresholds, denoted by ε below. This parameter establishes relative errors in the matrix elements; for example, if ε is set to 10^{-4} and the matrix element is 100 cm^{-1} then the absolute error introduced by thresholds should be less than .01cm^{-1}. This parameter is used in the following steps:

- CSFs with coefficients smaller than $\frac{\varepsilon}{N_p N_a}$ are ignored (N_p is 2 for the 2E method and 1 for the 1E and the P2E methods).
- In the loop over CSF pairs the calculation proceeds only if the product of two CI coefficients is larger than $\frac{\varepsilon}{N_p N_a^2}$.
- In the loop over determinant pairs the calculation proceeds only if the product of two CI coefficients times the determinant's coefficients times the overlap, $q_I q_J C_K C_L O$, is larger than $\frac{\varepsilon}{N_p N_a^2 N_o}$, where N_o is the number of occupied orbitals in the active space (i.e. N_e for FOCI or SOCI and N_a for CAS or FCI).

If there are several CI states with a given multiplicity, the maximum value of the CI coefficient product over these states is taken.

A benefit of using thresholds is the indirect use of symmetry. In many cases, the symmetry used by GUGA has to be lowered, e.g. in case of non-Abelian groups or when several states of different symmetry are requested for the same multiplicity. In such cases the threshold filters out the CSFs with coefficients equal to zero by symmetry (along with the ones allowed by symmetry but simply small in magnitude). The effect of introducing these thresholds can be seen below in the numerical examples.

g) Computational algorithm in detail

The current algorithm is shown in schematic form in Figure 1. In order to reduce the memory demand, drags and passes are introduced. If sufficient memory is available, there is only one pass and only one drag. If the amount of memory is insufficient to store all integrals at once, at first the code tries to break the 2e SOC $\hat{\ell}_x, \hat{\ell}_y, \hat{\ell}_z$ integrals not forbidden by

Figure 1. SOC algorithm

```
calculate AO SOC integrals.
Loop over bra multiplicities.
    Loop over ket multiplicities
        skip this pair of multiplicities if not allowed by symmetry[a]
        Loop over drags
            Loop over passes
                calculate SOC integrals
                Loop over ket CSFs
                    Loop over bra CSFs
                        skip this pair of CSFs if zero by symmetry[b] or small SOC[c]
                        Loop over bra determinants in the bra CSF
                            Loop over ket determinants in the ket CSF
                                skip this determinant pair if small SOC[c]
                                calculate SOC and properties
                        propagate the CSF matrix element for each pair of CI states[d]
        propagate CI state matrix elements into all combinations of M_s values[e].
        output matrix elements
diagonalise the H_so matrix and output results.
```

[a] Symmetry here refers to the rules due to spin angular momentum and hermiticity, as well as to the point group rules applied to all operators (i.e. SOC and properties) and all CI states.

[b] Here symmetry refers to point group symmetry for a pair of CSFs and all operators, as well as permutation symmetry (the maximum number of allowed discoincidences). The orbital occupations and the number of singly occupied orbitals as provided by GUGA are compared.

[c] Small SOC refers to the threshold values check

[d] This refers to $C^{\dagger}AC'$ transformation where C and C' are bra and ket CI coefficient matrices(expansion of CI states over CSFs, A is the matrix of an operator A in the CSF basis.

[e] The calculated values for SOC $\hat{L}_x, \hat{L}_y, \hat{L}_z$ matrix elements are combined to form matrix elements for each pair of M_s values by means described in the symmetry section.

symmetry into passes. Passes are used to divide the work for the components of $\hat{\ell}$ and drags divide the work for each component of $\hat{\ell}$. The following decision is made in the order of decreasing memory available:

one pass: all of symmetry allowed $\hat{\ell}_x, \hat{\ell}_y, \hat{\ell}_z$

two passes: pass 1: $\hat{\ell}_x, \hat{\ell}_y$; pass 2: $\hat{\ell}_z$

three passes: each $\hat{\ell}_i$ individually in the order x,y,z.

(Note that "forbidden by symmetry" as applied to integrals here refers not to integrals themselves, but to CI states. The meaning is that none of the CI state pairs requested will require these particular $\hat{\ell}$ integrals).

If insufficient memory is available for 2e integrals at the maximum number of passes (three or less if all CI states do not require some integrals), the minimum number of passes is used, and to reduce the amount of memory the integrals themselves are divided into chunks. During each drag, a fraction of 2e MO integrals is kept in memory and zeros are substituted via an index array in place of integrals not in memory).

6. Comparison of the indirect methods

a) general comments

The one electron method is the least resource consuming. The partial two-electron method in practice requires little more resources than the one-electron method. This is true for several reasons:

1. the number of determinant pairs to be considered is the same as for the one-electron method (at most one discoincidence allowed).

2. the four-index integral transformation can be done with the expense of a two-index transformation
3. there is no need to store four-index two-electron integrals in the MO basis **in memory**

Additional expenses include having to calculate two-electron integrals in the AO basis. They can be stored on disk while being calculated and read while doing the four-index transformation. This does not require a noticeable amount of memory, although if available, larger buffers can be used to speed up the calculation. These expenses (integrals and transformation) are usually insignificant, especially when compared to the expenses of the further matrix element calculation for a large CI.

On the other hand, the full two-electron method requires treating many more determinant pairs as the number of discoincidences can be two, the four-index transformation is not trivial and most importantly the two-electron integrals are to be kept in memory (for an efficient program) and their number is $N_a^4/4$ for orthogonal and N_a^4 for biorthogonal orbitals.

When comparing the methods numerically it is worth remembering that the first order perturbative SOC treatment and neglect of other interactions (spin-spin etc) can introduce errors comparable in magnitude to the error of the partial relative to the full two-electron method even for the first row of the Periodic Table.

The partial two-electron method developed here can be compared to the mean-field method[20]. The mean-field method is more general in the treatment of the active-active two-electron contribution. In the partial two-electron method, only the CAS core orbitals (spin-orbital occupation of 1) are included in the two-electron contribution. In the mean-field method, all active orbitals are assigned fixed occupation numbers (between 0 and 1). In both methods, the two-electron part is then summed over the coincident orbitals with these occupation numbers as weight factors. Both methods neglect contributions due to active-active discoincidences. The mean-field method introduces an approximation to the integrals

as well (namely, only one-centre integrals are computed and the rest are discarded; this is justified as the SOC operator is short-ranged). In the present partial two-electron method, no such approximation is made. The extra degree of freedom of the mean-field method (the freedom to choose occupation numbers) may be useful.

In the numerical examples below no empirical parameters are used (true nuclear charges). For the notation in the tables in this section, consult Table 4. The results are obtained with .1% relative error threshold.

b) introductory numerical examples

XH_2, X=C,Si,Ge,Sn,Pb.

Spin-orbit coupling between $^1A_1$ and $^3B_1$ states has been studied for a series of XH_2 molecules. The geometries are for the minimum energy potential surface crossing, as found in the previous ECP-based study[21]. The active space used here is [6/6], i.e. 6 electrons in 6 active orbitals. CASSCF spin-orbit coupling calculations have been performed using biorthogonal orbitals with the core optimised for the singlet. The second order CI (SOCI) SOC calculations were performed with singlet orbitals. Two basis sets have been used. The first (Table 4) is the MINI basis set developed by Huzinaga *et al*[22]. The second is the WTBS minimal basis set for X and cc-ptvz for H, developed by Huzinaga *et al*[23] with two s and two p functions on each heavy atom uncontracted; in addition, one d on Ge, Sn, and Pb and one f on Pb are uncontracted. It is possible to study SOC at both CAS and SOCI level for the second basis set since this is not a minimal basis set. The results obtained using the larger basis are given in Table 5 and Table 6. A study of relativistic effects without separating scalar and vector contributions for similar species was conducted by Dyall[24].

Table 4. "Mini" basis set CAS XH_2 (X=C,Si,Ge,Sn,Pb) results.

	C_{1e} [a] cm^{-1}	C_{P2e} [a] cm^{-1}	C_{2e} [a] cm^{-1}	$\mathcal{E}_{P2e}$ % [b]	M_{1e} [c] cm^{-1}	M_{P2e} [c] cm^{-1}	M_{2e} [c] cm^{-1}
CH_2	26.78	14.89	13.25	12.4	18.937	8.406	9.565
SiH_2	96.38	74.57	73.73	1.1	68.15	15.42	16.01
GeH_2	539.9	481.1	480.4	.2	381.74	41.53	42.09
SnH_2	1226.	1137.	1136.	.05	867.26	63.45	63.86
PbH_2	2149.	2046.	2046.	.02	1519.40	72.50	72.79

[a] C_{1e} , C_{P2e} , C_{2e} denote SOCC for 1E,P2E and 2E SOC correspondingly

[b] $\mathcal{E}_{P2e}$ denotes relative error in C(C_{P2e} relative to C_{2e})

[c] M_{1e} , M_{P2e} , M_{2e} denote absolute values of 1E, P2E and 2E matrix elements. The 1e and 2e matrix elements are always opposite in sign.

Table 5. WTBS basis set CAS XH_2 (X=C,Si,Ge,Sn,Pb) results.

	C_{1e} cm^{-1}	C_{P2e} cm^{-1}	C_{2e} cm^{-1}	$\mathcal{E}_{P2e}$ %	M_{1e} cm^{-1}	M_{P2e} cm^{-1}	M_{2e} cm^{-1}
CH_2	24.34	14.12	12.27	14.6	17.213	7.232	8.540
SiH_2	74.25	57.93	57.11	1.4	52.50	11.54	12.12
GeH_2	367.7	328.10	327.3	.2	260.03	28.03	28.57
SnH_2	813.8	757.0	756.5	.06	575.47	40.18	40.56
PbH_2	2092.	1999.	1999.	.02	1479.22	65.60	65.92

Table 6. WTBS basis set SOCI XH_2 (X=C,Si,Ge,Sn,Pb) results.

	C_{1e} cm^{-1}	C_{P2e} cm^{-1}	C_{2e} cm^{-1}	$\mathcal{E}_{P2e}$ %	M_{1e} cm^{-1}	M_{P2c} cm^{-1}	M_{2e} cm^{-1}
CH_2	23.54	13.66	11.92	15.1	16.645	6.989	8.218
SiH_2	72.31	56.42	55.64	1.4	51.13	11.24	11.79
GeH_2	374.2	333.4	332.7	.2	264.58	28.80	29.32
SnH_2	850.2	789.6	789.1	.07	601.18	42.85	43.23
PbH_2	2242.	2140.	2140.	.02	1585.69	72.06	72.39

Note that for both basis sets and at both levels of theory (CAS, SOCI), the agreement between P2E and 2E methods is quite reasonable for all Group IVA elements, and the relative error decreases with increasing mass. The use of SOCI has only a small effect relative to the CASSCF results.

X^+_2, X=O,S,Se,Te.

For these species, spin-orbit coupling is studied at the CAS level. The basis set is 6-21G[25] (X=O) or 3-21G[25](X=S,Se,Te). The geometry has been optimised at the CAS level. The experimental value for the $^2\Pi_{3/2}$-$^2\Pi_{1/2}$ splitting in O_2^+ is[26] 200.2 cm^{-1} and with a better basis set the theoretical prediction is[26] 195.1 cm^{-1}. The results are presented in Table 7.

As for the XH_2 species, the partial two-electron method is seen to provide reasonable accuracy relative to the full 2E method. The first row of the Periodic Table may require full two-electron treatment if high accuracy is sought after.

Table 7. X_2^+ (X=O,S,Se,Te) CASSCF/split basis results.

	R_{X-X},Å	C_{1e} cm^{-1}	C_{P2e} cm^{-1}	C_{2e} cm^{-1}	$\mathcal{E}_{P2e}$ %	M_{1e} cm^{-1}	M_{P2e} cm^{-1}	M_{2e} cm^{-1}	$^2\Pi_{3/2}$-$^2\Pi_{1/2}$ [a], cm^{-1}
O_2^+	1.267	177.8	117.0	110.2	6.1	125.70	42.98	47.76	155.9
S_2^+	1.869	416.1	338.7	336.2	.74	294.22	54.74	56.51	475.4
Se_2^+	2.150	1470.	1317.	1315.	.15	1039.36	107.85	109.24	1860
Te_2^+	2.585	2643.	2452.	2451.	.05	1869.04	135.16	136.05	3466

[a] $^2\Pi_{3/2}$-$^2\Pi_{1/2}$ splitting obtained with the full two-electron SOC.

c) Effect of orbitals and CI level on SOC

Next, consider the recently studied van der Waals structures of BH_2[27] and AlH_2[28]. Spin-orbit coupling plays an important role in the chemistry of many high energy species, because it is very important for such materials to exhibit sufficiently high barriers to ensure stability. Such barriers can be greatly lowered due to potential energy curve crossing caused by diabatic interactions such as spin-orbit coupling. The geometries used represent the minimum energy crossing of the $^2A_1$ and $^2B_2$ surfaces at the multi-reference CI (MRCI) level of theory. The effect of orbitals and CI level on both the splitting between $^2A_1$ and $^2B_2$ surfaces and spin-orbit coupling with both full and partial two-electron methods has been studied. All valence electrons are included in the active space ([5/6]). The basis set for BH_2 is aug-cc-pVTZ[29] on both B and H, for AlH_2 it is cc-pVTZ[30] on Al and aug-cc-pVTZ on H. The results are summarised in Table 8 and Table 9, for BH_2 and AlH_2, respectively.

Table 8. BH_2 CAS/FOCI/SOCI SOC results.

CI	Orb	$^2B_2$-$^2A_1$ cm^{-1}	C_{1e} cm^{-1}	C_{P2e} cm^{-1}	C_{2e} cm^{-1}	$\mathcal{M}_{1e}$ cm^{-1}	$\mathcal{M}_{P2e}$ cm^{-1}	$\mathcal{M}_{2e}$ cm^{-1}
CAS	^2A_1c	300.6	6.85	3.39	3.01	4.8409	2.4446	2.7157
CAS	^2B_2c	-544.6	6.86	3.42	3.02	4.8495	2.4341	2.7137
CAS	$^2A_1$	7578.5	7.00	3.47	3.05	4.9494	2.4927	2.7920
CAS	$^2B_2$	-3852.7	7.16	3.56	3.14	5.0642	2.5456	2.8410
CAS	$^2A_1$+$^2B_2$	-1058.1	7.02	3.48	3.07	4.9621	2.5046	2.7944
FOCI	$^2A_1$	578.5	6.68	3.32	2.92	4.7255	2.3801	2.6607
FOCI	$^2B_2$	-2962.9	6.75	3.37	2.98	4.7756	2.3940	2.6707
FOCI	$^2A_1$+$^2B_2$	-2599.8	6.76	3.35	2.97	4.7800	2.4111	2.6804
SOCI	$^2A_1$	701.9	6.79	3.37	3.00	4.7994	2.4176	2.6795
SOCI	$^2B_2$	-1499.7	6.81	3.40	3.02	4.8147	2.4120	2.6797
SOCI	$^2A_1$+$^2B_2$	-1160.9	6.78	3.37	3.00	4.7966	2.4168	2.6770

Orb stands for the sets of molecular orbitals:

^2A_1c: two separate MO sets, fully optimised for $^2A_1$ and $^2B_2$ optimised with $^2A_1$ core.

^2B_2c: two separate MO sets, $^2B_2$ fully optimised and $^2A_1$ with $^2B_2$ core.

All other rows represent single MO set, $^2A_1$+$^2B_2$ being two state averaged (50%+50%) orbital set.

$^2B_2$-$^2A_1$ refers to adiabatic splitting between the two levels.

Table 9. AlH_2 CAS/FOCI/SOCI SOC results.

CI	Orb	$^2B_2$-$^2A_1$ cm^{-1}	C_{1e} cm^{-1}	C_{P2e} cm^{-1}	C_{2e} cm^{-1}	M_{1e} cm^{-1}	M_{P2e} cm^{-1}	M_{2e} cm^{-1}
CAS	^2A_1c	337.5	23.77	17.90	17.66	16.8093	4.1529	4.3231
CAS	^2B_2c	177.9	23.12	17.38	17.14	16.3516	4.0595	4.2296
CAS	$^2A_1$	8373.7	30.99	23.36	23.05	21.9145	5.3947	5.6152
CAS	$^2B_2$	-5805.3	29.79	22.31	21.99	21.0682	5.2916	5.5197
CAS	$^2A_1$+$^2B_2$	387.6	31.28	23.56	23.24	22.1195	5.4618	5.6839
FOCI	$^2A_1$	1322.2	26.31	19.68	19.38	18.6018	4.6854	4.8971
FOCI	$^2B_2$	-1282.0	26.97	20.18	19.89	19.0731	4.8031	5.0093
FOCI	$^2A_1$+$^2B_2$	1357.9	28.05	21.04	20.74	19.8357	4.9595	5.1679
SOCI	$^2A_1$	579.6	27.01	20.22	19.93	19.1014	4.8056	5.0060
SOCI	$^2B_2$	-411.7	26.45	19.76	19.48	18.7052	4.7330	4.9330
SOCI	$^2A_1$+$^2B_2$	38.2	27.62	20.69	20.41	19.5293	4.8971	5.0971

The results for these molecules demonstrate the general trend that the choice of orbitals and CI level can have a dramatic impact on the splitting between the two adiabatic levels. Because two similar numbers are subtracted, high accuracy in both is required for an accurate difference. At the same time the spin-orbit coupling is not a property obtained as a difference and thus a much smaller effect of both orbitals and CI level is observed. Nonetheless, the SOC constants predicted by the P2E method are in good agreement with the much more resource consuming full 2E method.

d) Effect of thresholds on SOC

AlH_2 as described above is chosen as a test of the influence of the threshold value upon SOC. $^2A_1$+$^2B_2$ orbitals are used throughout. Timings for SOC calculations represent the wall-clock time. The timing for the default value of the threshold (10^{-4}) and 2E method is set to one. At the CAS level, there are 59 $^2A_1$ and 56 $^2B_2$ CSFs (in C_{2v}). In this case the calculation of two-electron SOC integrals gives the dominant contribution to the timings. At the SOCI level, there are 130411 $^2A_1$ and 130314 $^2B_2$ CSFs (in C_{2v}). The results are represented in Table 10 and Table 11, respectively.

Table 10. Threshold effect on SOC, AlH_2 at CAS level.

ε	# $^2A_1$ CSFs	# $^2B_2$ CSFs	C_{1e} cm^{-1}	C_{P2e} cm^{-1}	C_{2e} cm^{-1}	M_{1e} cm^{-1}	M_{P2e} cm^{-1}	M_{2e} cm^{-1}	P2E time[a]	2E time[a]
10^{-2}	56	55	31.29	23.51	23.25	22.1289	5.4522	5.6865	.95	1.00
10^{-3}	59	56	31.28	23.55	23.24	22.1194	5.4606	5.6839	.94	1.01
10^{-4}	59	56	31.28	23.56	23.24	22.1195	5.4618	5.6839	.94	1.
10^{-5}	59	56	31.28	23.56	23.24	22.1195	5.4617	5.6839	.94	1.01
10^{-6}	59	56	31.28	23.56	23.24	22.1195	5.4617	5.6839	.94	1.00

[a] arbitrary units.

At the 10^{-4} threshold, the preceding CI takes .32 and the 1E method .23 in the units of of 2E method. Thus the P2E method takes comparable time with the 1E method (.26 vs .23), the difference coming from two-electron integrals and four-index transformation.

The results obtained in this subsection demonstrate that the threshold values are set

properly, that is, the relative error in SOC is not greater than the threshold value used. Some feeling for the increase in computational expense (time) as a function of the threshold value is gained as well. It can be seen that the timings for the P2E method is far less dependent upon threshold as compared to the 2E method, at the SOCI level of theory.

Table 11. Threshold influence on SOC, AlH_2 at SOCI level.

ε	# $^2A_1$ CSFs	# $^2B_2$ CSFs	C_{1e} cm^{-1}	C_{P2e} cm^{-1}	C_{2e} cm^{-1}	M_{1e} cm^{-1}	M_{P2e} cm^{-1}	M_{2e} cm^{-1}	P2E time[a]	2E time[a]
10^{-2}	37055	39826	27.56	20.64	20.37	19.4859	4.8821	5.0854	.04	.13
10^{-3}	90586	93769	27.61	20.68	20.40	19.5220	4.8938	5.0951	.13	.42
10^{-4}	122268	123589	27.62	20.69	20.41	19.5293	4.8971	5.0971	.26	1.
10^{-5}	129483	129651	27.62	20.69	20.41	19.5306	4.8976	5.0975	.33	1.84
10^{-6}	130317	130251	27.62	20.69	20.41	19.5308	4.8977	5.0975	.37	2.75

[a] arbitrary units.

e) Comparison with the mean-field method

The PdCl system was investigated with the mean-field method in Ref. 20. The relative error of the mean-field method relative to the full two-electron result ($\mathcal{E}_{2e}$, %) is .02. In Table 12 the results obtained with the methods described in this work, using the MINI basis set and full valence active space [17/10] are given. The geometry has been optimised for the term of interest, $^2\Delta$.

Table 12. SOC in transtion metal systems XCl, where X=Ni, Pd, Pt for the $^2\Delta$ term.

	$R_{X\text{-}Cl}$,Å	C_{1e}	C_{P2e}	C_{2e}	$\mathcal{E}_{P2e}$ %	M_{1e}	M_{P2e}	M_{2e}
NiCl	2.119	1236.	729.9	677.2	7.8	874.049	357.959	395.21
PdCl	2.491	2496.	1792.	1780.	.7	1764.839	497.506	506.147
PtCl	2.523	7018.	5764.	5755.	.1	4962.263	886.487	892.539

As expected, the mean-field method works better than P2E, as it has an extra degree of freedom and treats active-active contributions rather than omit them as the partial method does. The neglect of some two-electron integrals in the mean-field method did cancel the error introduced by neglecting the two discoincidence case. The partial two-electron method appears to provide sufficient accuracy, although for Ni the full two-electron approach may be desired for highly accurate calculations. A very interesting observation is made here: the two-electron contribution for transition metals (at least for the molecules considered in this subsection) is much larger than that for the main group elements in the analogous rows in the periodic table.

f) Magnitude of SOC

The question of whether spin-orbit coupling interaction can be expected to be large or small can be addressed in general. The expressions for the SOC (Eq. (9) and (19)) suggest that the magnitude of the spin-orbit coupling interaction can be traced to the magnitude of spin-orbit coupling integrals in the molecular orbital basis. These integrals (or their atomic orbital counterparts) are undoubtedly dependent upon the local nature of the spin-orbit coupling operator that has a built in r^{-3} dependence. Therefore, it can be seen that one-centre

integrals are the major contributors to the interaction. Thus, the SOC integrals in the MO basis are expected to be in general larger for bra and ket MOs localised on the same atom. This leads to a suggestion of using localised orbitals for the approximations of neglecting multi-centre integrals.

Secondly, it can be expected that for atoms the magnitude of SOC coupling is expected to be larger in general than for molecules. Interestingly, some molecules are known to exibit a SOC interaction virtually identical to that of a single atom[20]. Still, as the atomic weight increases, the inner shell core orbitals become less and less changed by chemical bonding, hence it is the core orbitals on these heavy elements that provide the major contribution to the SOC regardless of chemically active valence orbitals. It is expected that molecular complexes involving the interaction of atoms in the middle of the periodic table with light element molecules retain to a large extent their atomic spin-orbit coupling interactions. The magnitude of these spin-orbit couplings is expected to be larger than those in molecules where the middle-sized atoms form bonds and lose their atomic character.

Certainly, symmetry plays an important role in determining the magnitude of SOC because large contributions can occur with opposite phases and the value of SOC is then determined by smaller contributions. The effect of orbital shape upon the magnitude of SOC has also been studied[31].

7. Discussion and Summary

It is found that the two-electron contribution to the spin-orbit coupling grows roughly as a linear function of the nuclear charge. The one-electron part exhibits a more complicated dependence upon the nuclear charge in the range between linear and square. As expected, the partial two-electron method systematically underestimates the two-electron matrix elements,

with the relative error systematically decreasing down the Periodic Table. It can be seen that already for the second period the error introduced by the partial two-electron method becomes negligible or at least comparable to other approximations (non-relativistic unperturbed wavefunction, first order perturbative treatment, etc). With a set of reoptimised empirical parameters, a semi-empirical partial two-electron method may toffer much better performance (for heavier elements) than the one-electron semi-empirical method, for the first row of the periodic table. For the second row, the ab initio partial two-electron method is expected to deliver sufficient accuracy. There does not seem to be any real necessity to include two-electron terms for the last row.

Various aspects of the dependence of spin-orbit coupling upon various factors are discussed in the above subsections where the appropriate numerical examples are studied.

Acknowledgements

Many helpful discussions with Thomas Furlani, Shiro Koseki and comments made by Michael Schmidt are gratefully acknowledged. This work was supported by the Ames Laboratory via the Department of Energy Basic Energy Sciences Office.

References

[1] M. W. Schmidt, K. K. Baldridge, J. A. Boatz, S. T. Elbert, M. S. Gordon, J. H. Jensen, S. Koseki, N. Matsunaga, K. A. Nguyen, S. J. Su, T. L. Windus, M. Dupuis and J. A. Montgomery, J. Comput. Chem. **14**, 1347-1363 (1993).

[2] S. Koseki, M. W. Schmidt and M. S. Gordon, J. Phys. Chem. **96**, 10768 (1992),

[3] S. Koseki, M. S. Gordon, M. W. Schmidt and N. Matsunaga, J. Phys. Chem. **99**, 12764 (1995).

[4] L. Veseth, J. Phys. B **14**, 795 (1981)

[5] R. B. Ross, W. C. Ermler and P. A. Christiansen, J. Chem. Phys. **84**, 3297 (1985)

[6] S. Yabushita, THEOCHEM. **461-462**, 523-532 (1999).

[7] T. R. Furlani and H. F. King, J. Chem. Phys. **82**, 5577 (1985).

[8] R. J. Harrison, Int. J. Quantum Chem. **40**, 847 (1991).

[9] M. Snir, S. Otto, S. Huss-Lederman, D. Walker and J. Dongarra, The complete MPI reference (The MIT Press, Cambridge, 1998).

[10] H. A. Bethe, E. E. Salpeter, Quantum Mechanics of the one and two electron atoms (Plenum, New York, 1977).

[11] H. F. King, R. E. Stanton, H. Kim, R. E. Wyatt and R. G. Parr, J. Chem. Phys. **47**, 1936 (1967).

[12] B. H. Lengsfield, III, J. A. Jafri and D. H. Phillips, J. Chem. Phys. **74**, 6849 (1981).

[13] D. M. Brink and G. R. Satchler, Angular Momentum (Charedon Press, Oxford, 1968).

[14] D. G. Fedorov, M. S. Gordon, to be submitted to Theor. Chem. Acta

[15] T. Furlani, PhD Thesis, (SUNY at Buffalo, 1984).

[16] L. F. Pacios and P. A. Christiansen, J. Chem. Phys. **82**, 2664 (1985).

[17] Y. Sakai, E. Miyoshi, M. Klobukowski and S. Huzinaga, J. Chem. Phys. **106**, 8084 (1997)

[18] C. M. Marian and U. Wahlgren, Chem. Phys. Lett, **251**, 357 (1996).

[19] T. E. H. Walker and W. G. Richards, J. Chem. Phys. **52**, 1311 (1970).

J.S. Cohen, W. R. Wadt and P.J. Hay, J. Chem. Phys. **71**, 2955 (1971).

P. J. Hay, W. R. Wadt, L. R. Kahn, R. C. Raffineti and D. H. Phillips, J. Chem. Phys. **71**, 1767 (1979)

W. R. Wadt, Chem. Phys. Lett. **89**, 245 (1982)

S. R. Langhoff, J. Chem. Phys. **73**, 2379 (1980).

[20] B. A. Heß, C. M. Marian, U. Wahlgren, O. Gropen, Chem. Phys. Lett. **251**, 365 (1996).

C. M. Marian and U. Wahlgren, Chem. Phys. Lett. **251**, 357 (1996).

[21] N. Matsunaga, S. Koseki and M. S. Gordon, J. Phys. Chem. **104**, 7988 (1996).

[22] S.Huzinaga, J.Andzelm, M.Klobukowski, E.Radzio-Andzelm, Y.Sakai and H.Tatewaki, Gaussian Basis Sets for Molecular Calculations (Elsevier, Amsterdam, 1984).

[23] S. Huzinaga and B. Miguel, Chem. Phys. Lett. **175**, 289 (1990).

S. Huzinaga and M. Klobukowski, Chem. Phys. Lett. **212**, 260 (1993).

Basis sets were obtained from the Extensible Computational Chemistry Environment Basis Set Database, Version 1.0, as developed and distributed by the Molecular Science Computing Facility, Environmental and Molecular Sciences Laboratory which is part of the Pacific Northwest Laboratory, P.O. Box 999, Richland, Washington 99352, USA, and funded by the U.S. Department of Energy. The Pacific Northwest Laboratory is a multi-program laboratory operated by Battelle Memorial Institue for the U.S. Department of Energy under contract DE-AC06-76RLO 1830. Contact David Feller or Karen Schuchardt for further information.

[24] K. Dyall, J. Chem. Phys. 96, 1210 (1992)

[25] J. S. Binkley, J. A. Pople and W. J. Hehre, J. Am. Chem. Soc. **102**, 939 (1980).

M. S. Gordon, J. S. Binkley, J. A. Pople, W. J. Pietro and W. J. Hehre J. Am. Chem. Soc. **104**, 2797 (1982).

K. D. Dobbs and W. J. Hehre, J. Comput. Chem. **7**, 359 (1986)

[26] D. G. Fedorov, M. Evans, Y. Song, M. S. Gordon and C. Y. Ng, submitted to J. Chem. Phys.

[27] M. S. Gordon, V.-A. Glezakou and D. R. Yarkony, J. Chem. Phys. **108**, 5657 (1998)

[28] G. Chaban, Chem. Phys. Lett. **278**, 195 (1997)

[29] T.H. Dunning, Jr. J. Chem. Phys. **90**, 1007 (1989).

R.A. Kendall, T.H. Dunning, Jr. and R.J. Harrison, J. Chem. Phys. **96**, 6769 (1992).

[30] D.E. Woon and T.H. Dunning, Jr., J. Chem. Phys. **98**, 1358 (1993).

R.A. Kendall, T.H. Dunning, Jr., and R.J. Harrison, J. Chem. Phys. **96**, 6796 (1992).

[31] J. Michl, J. Am. Chem. Soc. **118**, 3568 (1996)

CHAPTER III. SPEEDING UP SPIN-ORBIT COUPLING CALCULATIONS

A paper to be submitted to *Theor. Chem. Acc.*

Dmitri G. Fedorov, Mark S. Gordon

Abstract

A thorough review of the symmetry properties of the spin-orbit coupling operator and its matrix elements is presented. Various consequences of symmetry upon the practical calculations of spin-orbit coupling matrix elements at both point and double group level are illuminated. A parallelisation scheme and various steps unrelated to symmetry toward making the calculations more efficient are discussed. Tests of scalability of the code are presented.

1. Introduction

Recent progress in studying molecular dynamics involving states of different multiplicities, such as conical intersection studies[1,2], relies to a large degree on the ability to calculate spin-orbit coupling matrix elements. Non-relativistic (NR) calculations involving average-sized elements, such as those in the 4th or 5th row of the Periodic Table, can be greatly improved in terms of energy level splittings by using perturbative treatments involving spin-orbit (SO) coupling. There are many different techniques available to obtain numerical results[3,4,5] for a given system.

An efficient spin-orbit coupling calculation will take advantage of symmetry and various computational techniques to improve the efficiency. This paper begins with a consideration of the applicable symmetry rules. This will be followed by a discussion of the computational aspects of the spin-orbit coupling matrix elements.

The number of non-zero elements that must be calculated can be greatly reduced by predicting ahead of time which matrix elements are zero due to symmetry. The general SO matrix element can be written as:

$$<\alpha\Gamma i S M_s \mid \hat{H}_{so} \mid \alpha'\Gamma' i' S' M_s' > \qquad (1)$$

where the Pauli-Breit Hamiltonian[6] $\hat{H}_{so}$ contains both one and two electron operators. The state $|\alpha\Gamma i S M_s>$ contains the symmetry labels of the wavefunction obtained from a NR calculation: Γ denotes the irreducible representation (irrep) of the point group G of the molecule, i distinguishes degenerate components of Γ, α distinguishes equivalent irreps, S(S+1) and M_s are the eigenvalues of the spin operators $\hat{S}^2$ and $\hat{S}_z$, respectively.

The matrix element in (1) represents the first-order perturbation theory correction to the NR wavefunction. Since the non-relativistic Hamiltonian commutes with $\hat{S}^2$ and $\hat{S}_z$, one significant use of symmetry is to apply the Wigner-Eckart theorem[7]. Secondly, $\hat{H}_{so}$ commutes with a set of rotation and reflection operators, applied to both orbital and spin variables, forming the double group $\overline{G}$, just as the non-relativistic (NR) Hamiltonian commutes with a set of space rotations and reflections forming group G. The eigenvectors of the matrix representation of $\hat{H}_{so}$ in the basis $|\alpha\Gamma i S M_s>$ can therefore be classified according to the irreps of the double group. Linear combinations of the original states $|\alpha\Gamma i S M_s>$ with eigenvectors of the H_{so} matrix as expansion coefficients form states with a distinct double group symmetry in which $\hat{H}_{so}$ is diagonal. Selection rules for groups with infinite-fold axes are generally not useful in chemistry because polyatomic molecules usually possess lower symmetry. *The following discussion is intended mainly for the finite*

groups. The exact type of nonrelativistic wavefunction is irrelevant as long as it can be described by the labels specified above. A notable exception is the unrestricted Hartree-Fock (UHF) wavefunction, where the rules involving spin angular momentum symmetry are not applicable because the wavefunction is not an eigenfunction of $\hat{S}^2$.

It should be noted that most of the symmetry rules presented here have been known but not gathered together prior to this work (see, for example, Ref. 2,8,9,[10]). Rules that have not been discussed previously are presented in more detail in the text and in the Appendices. In addition to consideration of symmetry, methods for improving the efficiency of spin-orbit coupling calculations, including the use of parallelisation, are presented.

2. The Wigner-Eckart theorem

The theorem states that:

$$\left\langle \alpha jm \left| \hat{T}_q^k \right| \alpha' j' m' \right\rangle = (j', k, m', q \mid j, m) \frac{\left\langle \alpha j \left| \hat{T}^k \right| \alpha' j' \right\rangle}{\sqrt{2j'+1}} \tag{2}$$

where $\hat{T}_q^k$ is an irreducible spherical tensor operator of rank k, $\hat{T}^k$ is the so called reduced tensor operator, (j',k,m',q|j,m) are Clebsch-Gordan coefficients (assumed below to be real), |αjm> are eigenvectors of angular momentum operators $\hat{J}^2$ and $\hat{J}_z$ and α is used to denote any other labels. Now, $\hat{H}_{so}$ transforms as $\sum_i \left(\hat{l}_i \cdot \hat{s}_i\right)$ or $(\hat{L}\cdot\hat{S}) = \hat{L}_0\hat{S}_0 - (\hat{L}_+\hat{S}_- + \hat{L}_-\hat{S}_+)/2$ and $\hat{J}_\pm = \mp\left(\hat{J}_x \pm i\hat{J}_y\right)$. Taking $\hat{T}_q^k$ to be $\hat{S}_+, \hat{S}_0, \hat{S}_-$ where k=1 and q=1,0,-1, it is therefore possible to rewrite the matrix element (1) as:

$$\left\langle \alpha\Gamma i S M_s \left| \hat{H}_{so} \right| \alpha'\Gamma' i' S' M_s' \right\rangle = \sum_{q=-1}^{1} (S', 1, M_s', q \mid S, M_s) \left\langle \alpha\Gamma i S \left| \hat{L}_{-q}\hat{S} \right| \alpha'\Gamma' i' S' \right\rangle (-1)^q \tag{3}$$

where the numerical constants are included in $\hat{L}_q$ for simplicity and the vector operator $\hat{\vec{S}}$ has been reduced to the scalar operator $\hat{S}$. For S=0 and S'=0 the coefficient (S',1,0,0|S,0)= 0,

so it follows that:

(a) A matrix element between two singlets is zero.

Secondly, using the property of the Clebsch-Gordan coefficients $(S,1,M_s,q|S',M_s')= 0$ if $|S-S'|>1$ or $M_s+q\ M_s'$, one obtains:

(b) The SO matrix elements are zero unless $|S-S'|\leq 1$

Furthermore,

(c) <u>at most three elements</u> need to be explicitly calculated, <u>given S and S'</u>.

$$\langle\alpha\Gamma iSM_s' -1|\ \hat{H}_{so}|\ \alpha'\Gamma'i'S'M_s'\rangle = (S',1,M_s',-1|S,M_s'-1)\langle\alpha\Gamma iS|\ \hat{L}_+\hat{S}|\ \alpha'\Gamma'i'S'\rangle(-1) \quad (4)$$

$$\langle\alpha\Gamma iSM_s'|\hat{H}_{so}|\ \alpha'\Gamma'i'S'M_s'\rangle\ = (S',1,M_s',0|SM_s')\langle\alpha\Gamma iS\ |\ \hat{L}_0\hat{S}|\ \alpha'\Gamma'i'S'\rangle \quad (5)$$

$$\langle\alpha\Gamma iSM_s'+1|\ \hat{H}_{so}|\ \alpha'\Gamma'i'S'M_s'\rangle = (S',1,M_s',+1|S,M_s'+1)\langle\alpha\Gamma iS|\ \hat{L}_-\hat{S}|\ \alpha'\Gamma'i'S'\rangle(-1) \quad (6)$$

The remaining elements are:

1) zero if $|M_s-M_s'|>1$ *The H_{so} matrix is tridiagonal (diagonal being defined as $M_s=M_s'$).*

2) calculated for an arbitrary M_s by using one of the basic three expressions in (c) e.g.:

$$\langle\alpha\Gamma iS\ M_s -1|\ \hat{H}_{so}|\ \alpha'\Gamma'i'S'\ M_s\rangle =$$

$$(S',1,\ M_s -1|S,M_s -1)\langle\alpha\Gamma iS|\ \hat{L}_+\hat{S}|\ \alpha'\Gamma'i'S'\rangle/(S',1,M_s',-1|S,M_s'-1)(-1) \quad (7)$$

where the reduced matrix element is calculated from the above defining relation (for M_s').

It should be noted that some Clebsch-Gordan coefficients are equal to zero, for example, (1,1,0,0|1,0) and (2,2,0,0|1,0). It is important to keep this in mind when actually implementing the Wigner-Eckart usage of the reduced matrix elements. It is not possible to use $M_s=M_s'=0$ to get the reduced matrix element in these cases as it would lead to division by zero. Using the largest possible M_s such as $M_s=S$, $M_s'=S'$, however, always leads to non-zero Clebsch-Gordan coefficients.

3. Hermiticity and time reversal, real valued NR states

If one uses real valued NR states, it is possible to **reduce** the number of matrix elements one must explicitly calculate from **three** to **two**. Note that this corresponds to calculating matrix elements of the three operators represented schematically by $\hat{L}_x\hat{S}, \hat{L}_y\hat{S}, \hat{L}_z\hat{S}$.

Elements along subdiagonals are bound by a simple relation. To see this, consider states of different multiplicity,

$$\langle \alpha\Gamma iSM_s|\hat{H}_{so}|\alpha'\Gamma'i'S+1,M_s+1\rangle = (S+1,1,M_s+1,-1|S,M_s)\langle \alpha\Gamma iS|\hat{L}_+\hat{S}|\alpha'\Gamma'i'S+1\rangle(-1) \tag{8}$$
$$= (S+1,1,M_s+1,-1|S,M_s)(-1)\left[-i\langle \alpha\Gamma iS|\left[\hat{\vec{r}}\times\hat{\vec{p}}\right]_x\hat{S}|\alpha'\Gamma'i'S+1\rangle + (-i)i\langle \alpha\Gamma iS|\left[\hat{\vec{r}}\times\hat{\vec{p}}\right]_y\hat{S}|\alpha'\Gamma'i'S+1\rangle\right](-1)$$

$$\langle \alpha\Gamma iS,-M_s|\hat{H}_{so}|\alpha'\Gamma'i'S+1,-M_s-1\rangle = (S+1,1,-M_s-1,1|S,-M_s)\langle \alpha\Gamma iS|\hat{L}_-\hat{S}|\alpha'\Gamma'i'S+1\rangle(-1)$$
$$= (S+1,1,-M_s-1,1|S,-M_s)\left[-i\langle \alpha\Gamma iS|\left[\hat{\vec{r}}\times\hat{\vec{p}}\right]_x\hat{S}|\alpha'\Gamma'i'S+1\rangle - i(-i)\langle \alpha\Gamma iS|\left[\hat{\vec{r}}\times\hat{\vec{p}}\right]_y\hat{S}|\alpha'\Gamma'i'S+1\rangle\right](-1) \tag{9}$$

It can be proven generally that $(S+1,1,M_s+1,-1|SM_s) = (S+1,1,-M_s-1,1|S,-M_s)$ (Appendix III), so that by comparing the right-hand sides of equations (8) and (9) it can be seen that their left-hand sides are bound by the relation:

$$\langle \alpha\Gamma iS\, M_s|\hat{H}_{so}|\alpha'\Gamma'i'S+1, M_s+1\rangle = \langle \alpha\Gamma iS, -M_s|\hat{H}_{so}|\alpha'\Gamma'i'S+1, -M_s-1\rangle^* \tag{10}$$

Similarly, for states of the same multiplicity:

$$\langle \alpha\Gamma iSM_s-1|\hat{H}_{so}|\alpha'\Gamma'i'SM_s\rangle = (S,1,M_s,-1|S,M_s-1)\langle \alpha\Gamma iS|\hat{L}_+\hat{S}|\alpha'\Gamma'i'S\rangle(-1)$$
$$= (S,1,M_s,-1|S,M_s-1)(-1)\left[-i\langle \alpha\Gamma iS|\left[\hat{\vec{r}}\times\hat{\vec{p}}\right]_x\hat{S}|\alpha'\Gamma'i'S\rangle + i(-i)\langle \alpha\Gamma iS|\left[\hat{\vec{r}}\times\hat{\vec{p}}\right]_y\hat{S}|\alpha'\Gamma'i'S\rangle\right](-1) \tag{11}$$

$$\langle \alpha\Gamma iSM_s|\hat{H}_{so}|\alpha'\Gamma'i'SM_s-1\rangle = (S,1,M_s-1,1|S,M_s)\langle \alpha\Gamma iS|L_-S|\alpha'\Gamma'i'S\rangle(-1)$$
$$= (S,1,M_s-1,1|S,M_s)\left[-i\langle \alpha\Gamma iS|\left[\hat{\vec{r}}\times\hat{\vec{p}}\right]_x\hat{S}|\alpha'\Gamma'i'S\rangle - i(-i)\langle \alpha\Gamma iS|\left[\hat{\vec{r}}\times\hat{\vec{p}}\right]_y\hat{S}|\alpha'\Gamma'i'S\rangle\right](-1) \tag{12}$$

However, $(S,1,M_s,-1|S,M_s-1)=(-1)\,(S,1,M_s-1,1|S,M_s)$ (Appendix III), so by comparing the

equations (11) and (12) it is seen that:

$$<\alpha\Gamma i S\, M_s\text{ -1}|\ \hat{H}_{so}|\ \alpha'\Gamma' i' S\, M_s> = <\alpha\Gamma i S\, M_s\ |\ \hat{H}_{so}|\ \alpha'\Gamma' i' S\, M_s\text{ -1}>^{*}(-1) \qquad (13)$$

For real NR states only the diagonal and one subdiagonal need to be explicitly calculated. The other subdiagonal is readily calculated as the complex conjugate (different multiplicities) or negative complex conjugate(same multiplicities) of the first subdiagonal.

Hermitian character of $\hat{H}_{so}$.

Consider $<\alpha\Gamma i S M_s|\ \hat{H}_{so}|\ \alpha\Gamma i S M_s> \propto <\alpha\Gamma i S M_s|\ \hat{L}_o\hat{S}|\ \alpha\Gamma i S M_s>$

The matrix element must be real since the operator is Hermitian, but the angular momentum operator is proportional to i, imaginary unity. So, provided that **real basis functions** are used, this matrix element is purely complex. This implies that:

$$<\alpha\Gamma i S M_s|\ \hat{H}_{so}|\alpha\Gamma i S M_s> = 0 \qquad (14)$$

Using the previously obtained relation (9) for $\alpha=\alpha', \Gamma=\Gamma', i=i'$

$$<\alpha\Gamma i S M_s\text{-1}|\ \hat{H}_{so}|\ \alpha\Gamma i S M_s> = <\alpha\Gamma i S M_s|\ \hat{H}_{so}|\alpha\Gamma i S M_s\text{-1}>^{*}(-1)$$

Since $\hat{H}_{so}$ is Hermitian,

$$<\alpha\Gamma i S M_s\text{-1}|\ \hat{H}_{so}|\alpha\Gamma i S M_s> = <\alpha\Gamma i S M_s|\ \hat{H}_{so}|\alpha\Gamma i S M_s\text{-1}>^{*}$$

This implies that $<\alpha\Gamma i S M_s\text{-1}|\ \hat{H}_{so}|\alpha\Gamma i S M_s> = <\alpha\Gamma i S M_s|\ \hat{H}_{so}|\alpha\Gamma i S M_s\text{-1}> = 0 \qquad (15)$

From (14),(15) and (7) one concludes that:

Matrix elements between the same state are zero provided that the states are real-valued.

Time-reversal symmetry.

It can be proven generally[7] that the matrix elements of operators invariant under time reversal (such as $\hat{H}_{so}$) in **the time-reversal invariant basis set** are real. This could be useful if a different basis set (i.e., not simply NR wavefunctions, but certain linear

combinations of them) were employed. Such a basis can be constructed from linear combinations of $|\alpha\Gamma iSM\rangle \pm |\alpha\Gamma iS,-M\rangle$ for integer S.

4. Double group symmetry

As is well known, in order for a matrix element to be non-zero, the direct product of irreps to which bra, ket and the operator belong must contain the totally symmetric irrep. This is a consequence of the requirement that the matrix element taken as an integral over space variables and as a scalar product for the spin coordinates be independent of an arbitrary rotation of the entire system, that is,

$$\left\langle \Psi^{\Gamma_1} \left| A^{\Gamma_A} \right| \Psi^{\Gamma_2} \right\rangle = 0, \text{ unless } \Gamma_1 \otimes \Gamma_A \otimes \Gamma_2 \text{ contains the totally symmetric irrep.} \qquad (16)$$

Since $\hat{H}_{so}$ transforms as a scalar product of two pseudovectors **L** and **S**, it transforms as a scalar, or in other words it belongs to the totally symmetric irreducible representation. Thus the requirement for the matrix element to be non-zero is:

$$\sum_{g \in G} \chi^{\Gamma_1 *}(g)\chi^{\Gamma_2}(g) = \delta_{\Gamma_1,\Gamma_2} \quad \Leftrightarrow \quad \Gamma_1 = \Gamma_2, \quad \text{where } \chi \text{ are the characters.}$$

The NR wavefunctions will mix in general into several irreps of the double group, thus *the matrix element (16) is zero unless there is an irrep of the double group to which both bra and ket belong.*

The procedure for determining the double group irreps to which the nonrelativistic wavefunctions belong will be outlined below. This procedure can also be reversed to find bases of the irreducible representations of the double groups as well. Since the number of NR states included in the SO calculation is usually small, and in order to take advantage of conventional algorithms for the matrix element calculation, the NR states are used as a

basis. Consequently, the H_{so} matrix in this basis is diagonalised (as opposed to using the symmetry adapted states as the basis in which $\hat{H}_{so}$ is diagonal).

In the discussion below, bars above symbols (eg $\overline{G}$) denote double group entities. The following projection operators extract the functions belonging to the irrep of the double group:

$$P_k^{\overline{\Gamma}} = \frac{n_{\overline{\Gamma}}}{n_{\overline{g}}} \sum_{\overline{g} \in \overline{G}} D_{kk}^{\overline{\Gamma}^*}(\overline{g}) T_{\overline{g}} \tag{17}$$

where $T_{\overline{g}}$ is the rotation operator representation of the double group elements, $D_{kk}^{\overline{\Gamma}}(\overline{g})$ are the diagonal elements of the matrices of the irreps of $\overline{G}$, $n_{\overline{\Gamma}}$ is the order(degeneracy) of $\overline{\Gamma}$, $n_{\overline{g}}$ is the order(size) of $\overline{G}$. The condition for a state $|\alpha\Gamma iSM_s>$ to mix into row k of an irrep $\overline{\Gamma}$ is

$$P_k^{\overline{\Gamma}} \mid \alpha\Gamma i S M_s > \neq 0 \tag{18}$$

Before explicit formulae are obtained, it should be noted that generally for non-Abelian groups when doing quantum-mechanical calculations, one does not obtain states with a pretabulated irreducible representation row-symmetry. Unless special measures are taken, row symmetry specific components of degenerate irreps mix with each other. Thus, instead of having a distinct row label "i", a more general case will be considered, namely with label j which simply numbers degenerate components and does not correspond to row symmetry in the sense of transformation properties with pretabulated matrices. The case with the row symmetry present will be derived as a special case at the end.

A state with mixed row symmetry (i) can be written as

$$|\alpha\Gamma j S M_s\rangle = \sum_{i=1}^{n_\Gamma} a_{ij} |\alpha\Gamma i S M_s\rangle \tag{19}$$

Next, consider the relation $P_k^{\overline{\Gamma}} \mid \alpha\Gamma j S M_s > = 0$ (20)

$$T_{\bar{g}} \mid \alpha\Gamma jSM_s > = \sum_{i=1}^{n_\Gamma} a_{ij} T_{\bar{g}} \left| \alpha\Gamma iSM_s \right\rangle = \sum_{i=1}^{n_\Gamma} a_{ij} \sum_{i'}^{n_\Gamma} D^{\Gamma}_{i'i}(g) \sum_{M_s'=-S}^{S} D^{S}_{M_s' M_s}(\bar{g}) \left| \alpha\Gamma i'SM_s' \right\rangle = 0 \qquad (21)$$

where D^Γ and D^S are the matrices of the irreducible representations of groups G and Special Orthonormal group SO(3) (also known as R_3 and K_h), respectively, and a_{ij} are the coefficients. It should be noted that $D^\Gamma(g)$ does not depend on the colour (colour can be defined as the phase in the Euler angle representation: e.g., white colour set to $\delta=0$ and black to $\delta=2\pi$ as added to Euler angle α, spin-wavefunction changes sign when rotated by 2π) of $\bar{g}$ as the states $\mid \alpha\Gamma jSM_s >$ are classified in the group G (or in other words, as single-valued representations of the double group). The a_{ij} are unknown and treated as linearly independent quantities. Thus the relation (20) becomes:

$$P_k^{\bar{\Gamma}} \mid \alpha\Gamma jSM_s > = \frac{n_{\bar{\Gamma}}}{n_{\bar{g}}} \sum_{\bar{g}\in\bar{G}} D^{\bar{\Gamma}^*}_{kk}(\bar{g}) \sum_{i=1}^{n_\Gamma} a_{ij} \sum_{i'}^{n_\Gamma} D^{\Gamma}_{i'i}(g) \sum_{M_s'=-S}^{S} D^{S}_{M_s' M_s}(\bar{g}) \left| \alpha\Gamma i'SM_s' \right\rangle = 0 \qquad (22)$$

Using the linear independence of $\left| \alpha\Gamma i'SM_s' \right\rangle$, the individual coefficients are zero for all i' and M_s'.

$$\forall i', M_s' : \sum_{i=1}^{n_\Gamma} a_{ij} \sum_{\bar{g}\in\bar{G}} D^{\bar{\Gamma}^*}_{kk}(\bar{g}) D^{\Gamma}_{i'i}(g) D^{S}_{M_s' M_s}(\bar{g}) = 0 \qquad (23)$$

Finally, using the linear independence of a_{ij},the individual coefficients for all i, i' and M_s' are zero:

$$\forall i, i', M_s' : \sum_{\bar{g}\in\bar{G}} D^{\bar{\Gamma}^*}_{kk}(\bar{g}) D^{\Gamma}_{i'i}(g) D^{S}_{M_s' M_s}(\bar{g}) = 0 \qquad (24)$$

Therefore,

$$\sum_{\bar{g}\in\bar{G}} D^{\bar{\Gamma}^*}_{kk}(\bar{g}) D^{\Gamma}(g) \times D^{S}(\bar{g}) = 0 \qquad (25)$$

in terms of the tensor product for all M_S, and one can replace the D^S matrix by the M_S - column of D^S for a specific M_S. This is easily identifiable as the relation stating that the product of two irreducible representations Γ and S does not contain $\bar{\Gamma}$.

The final result given in equation (25) is easy to apply. It can be readily deduced that the states of odd 2S mix into double-valued irreps $\bar{\Gamma}$ only, and correspondingly even 2S states mix into single-valued irreps only. This follows from $D^{\bar{\Gamma}}_{kk}(\bar{g}) = \pm D^{\bar{\Gamma}}_{kk}(g)$ where the plus/minus refer to single/double valued irreps respectively; and from $D^S(\bar{g}) = \pm D^S(g)$ where the plus/minus refer to even/odd values of 2S, respectively. Note that $\bar{g}$ and g differ by a rotation of 2π about the z-axis (in the Euler angle representation).

Thus states of integer and half-integer S do not mix with each other.

The formula (25) can finally be simplified to:

$$\sum_{g\in G} D^{\bar{\Gamma}}_{kk}{}^{*}(g) D^{\Gamma}(g) \times D^{S}(g) = 0 \tag{26}$$

Note that the sum runs over the white elements of $\bar{G}$ (i.e. over a subgroup of $\bar{G}$ isomorphic to G). In the case of distinct row symmetry i, the direct product $D^{\Gamma} \times D^{S}$ is replaced by $D^{\Gamma}_i \times D^S$, where D^{Γ}_i stands for i-th column of D^{Γ}.

Matrices $D^S(g)$, also known as Wigner functions, are straightforward to calculate. Parametrisation of g by the three Euler angles is convenient (see Appendix I).

To summarise briefly, the double group selection rule is:

$\langle \alpha \Gamma i S M_s | \hat{H}_{so} | \alpha' \Gamma' i' S' M_s' \rangle$ *is zero if there are no* $\bar{\Gamma}$ *and k such that*

$$\sum_{g\in G} D^{\bar{\Gamma}*}_{kk}(g) D^{\Gamma}(g) \times D^{S}_{M_s}(g) \neq 0 \text{ and } \sum_{g\in G} D^{\bar{\Gamma}*}_{kk}(g) D^{\Gamma'}(g) \times D^{S'}_{M_s'}(g) \neq 0 \tag{27}$$

where $D^S_{M_s}$ *is the* M_s *column of* D^S. *In addition: S and S' should be both integer or both half-integer and* $\bar{\Gamma}$ *single or double valued respectively;* D^{Γ}_i *is to be used in place of* D^{Γ} *if row symmetry is present.*

As was pointed out earlier, only half-integer spins mix into double-valued irreps of $\overline{G}$, thus double group symmetry per se is used only for half-integer spins.

5. Point group symmetry

A somewhat different kind of selection rule can be derived from a combination of the Wigner-Eckart theorem and point group symmetry. After application of the Wigner-Eckart theorem one is left with matrix elements of the type: $<\alpha\Gamma i S M_s' -q| \hat{H}_{so} | \alpha'\Gamma' i' S' M_s'> \propto <\alpha\Gamma i S M_s' -q| \hat{L}_q \hat{S}| \alpha'\Gamma' i' S' M_s'>$

This matrix element is equal to zero unless $\Gamma \times \Gamma^{(q)} \times \Gamma'$ *contains the totally symmetric representation of G.* $\hat{L}_q$ itself transforms as linear combinations of the pseudovector components $\hat{L}_x, \hat{L}_y, \hat{L}_z$ (which transform as x,y,z except that they are even under inversion). Depending on implementation of actual calculations, it may be beneficial to explicitly rewrite the matrix elements in terms of $\hat{L}_x, \hat{L}_y, \hat{L}_z$, because for the more common groups it is $\hat{L}_x$ and $\hat{L}_y$ that have unique irrep labels rather than $\hat{L}_+$ and $\hat{L}_-$.

6. Comparison of the point and double group rules

Even though the point group rules may seem less powerful due to the absence of spin dependence, they are in fact more restrictive and useful than the double group rules. There are two reasons for this: the spin dependence is actually not neglected, but taken full advantage of by means of the Wigner-Eckart theorem, and secondly the basis set in terms of which the rules are formulated (NR wavefunction) is naturally suited for point group rules. The bases of the irreps of the double groups are often built from several NR functions,

so the latter functions themselves are unwieldy and a poor choice for the rules in the double group.

A pictorial example of this is a matrix element between two states having the same point group symmetry and spin (both S and M_s) (equivalent terms), e.g., $<1\text{-}^3A_1(M_s=0)|\ \hat{H}_{so}\ |2\text{-}^3A_1(M_s'=0)>$. Such a matrix element is always non-zero in the double group, as the radial and the spin symmetries are identical, however in the point group the symmetry rule reduces to the symmetry of the component of L_z. This makes the element equal to zero in those point groups in which L_z belongs to an irrep other than the totally symmetric one.

7. Computational speed-up

The symmetry selection rules can be used in several different ways. First, let us consider techniques to accelerate scalar (single CPU) code. As the size of the active space and the level of electron correlation increases, the number of either determinants or configuration state functions (CSFs) increases dramatically. The main computational difficulty in a SOC calculation usually is confined to having to deal with a large CI expansion. Although working in the determinant basis set has its own benefits, such as its relative simplicity and efficiency at the same time, the smaller expansion in the CSF basis can prove to be a significant advantage. Most techniques described below are applicable to both types of wavefunction expansion, the main difference being that CSFs are eigenfunctions of $\hat{S}^2$ and $\hat{S}_z$, whereas determinants are eigenfunctions of $\hat{S}_z$ only.

The approaches presented below are incorporated into the GAMESS package[11] as modifications of the original SOC code written by Koseki[4].

For a CSF-driven algorithm, a SOC code contains a loop over pairs of CSFs. The following criteria can be used to avoid calculating the matrix element between two CSFs.

a) Overall number of open shells:

GUGA provides the number of unpaired electrons for each CSF. These numbers for the two CSFs cannot differ by more than 1 (one-electron $\hat{H}_{so}$) or 2 (full Pauli-Breit Hamiltonian).

b) Orbital occupancies:

Each CSF has a unique orbital occupancy, consisting of determinants that differ only by spin occupations. The maximum allowed number of orbital discoincidences n is determined by the structure of the operator: n=1 if only one-electron terms are included and n=2 for the full Pauli-Breit Hamiltonian. To make this heavily used part of the code more efficient, the orbital occupancies (which can be 0, 1 or 2 for each orbital) are packed into integer arrays, 2 bits per orbital. To determine the number of occupancies exclusive or (XOR) is performed. The resultant array is split into 2-byte integer numbers. Each of these numbers is taken as an argument to a pretabulated function giving the number of discoincidences. The total number of discoincidences is then obtained as a sum of the values of the precalculated array over all 2-byte numbers. This reduces the linear dependency on the number of orbitals to a logarithmic dependency .

c) If the absolute value of the product of the two CI expansion coefficients is smaller than some threshold value (given by the user), there is no need to proceed further.

d) Symmetry selection rules. By using the selection rules discussed above, the calculation of matrix elements that are zero by symmetry can be avoided.

The parallelisation of this scheme can be achieved quite easily by dividing the loop over CSFs into all computer nodes available for the parallel run. Each node will then calculate its share of the CSF pairs, and the resultant matrix elements are then summed over

all nodes. A few timings obtained with the parallel version of GAMESS will be presented below.

As a test case a calculation of ArO[12] has been chosen. All calculations have been run on the Scalable Computing Laboratory 64 node Pentium cluster (ALICE[13]). Each node is a 200 MHz Pentium Pro with a 2GB hard disk and 256MB RAM. All timings are wall-clock and are given in seconds.

The basis set used is Ar=(11s,7p,1d)/[4s,3p,1d], O=(9s,5p,1d)/[3s,2p,1d], and the wavefunction is a 14 electrons in 8 orbitals complete active space self consistent field (CASSCF) plus single (FOCI) and single and double (SOCI) excitations into the virtual space. The following states were included in the spin-orbit coupling study: $1\text{-}^1\Sigma^+$, $^1\Pi$, $^1\Delta$, $2\text{-}^1\Sigma^+$, $^3\Pi$, $^3\Sigma^-$. There are 145776 singlet and 232848 triplet CSFs. CSFs were generated in C_1 symmetry to obtain all states at once, and SOC and ordinary integrals were calculated in C_{2v} symmetry. The energy levels including the spin-orbit coupling are given in Table 1.

The difference between 1e FOCI and SOCI levels is mostly due to the change of the adiabatic levels. The matrix elements themselves change less:

FOCI: $\langle 1\text{-}^1\Sigma^+|\hat{H}_{so}|^3\Pi\rangle = -8.7416i$ $\quad\quad$ $\langle ^3\Pi|\hat{H}_{so}|^3\Pi\rangle = -46.9683i$

SOCI: $\langle 1\text{-}^1\Sigma^+|\hat{H}_{so}|^3\Pi\rangle = -12.2431i$ $\quad\quad$ $\langle ^3\Pi|\hat{H}_{so}|^3\Pi\rangle = -45.1645i$

The differences between 1e and 2e SOC at the SOCI level are also fairly small, ≤ 35 cm^{-1}.

The scalability of SOC is given in Figure 1. Two-electron SO integrals in the AO basis as well as transformations into the MO basis are performed on each node independently to reduce the amount of communication traffic. As seen from the figure the scalability of the full Pauli-Breit Hamiltonian is the best. The overall scalability is dragged down by the CI code.

Table 1. ArO energy levels(in cm^{-1}) including spin-orbit coupling

Term	FOCI with 1e H_{so}	SOCI with 1e H_{so}	SOCI with 2e H_{so}
$^3\Pi_2$	-7764.1	-7727.7	-7692.8
$^3\Pi_1$	-7682.2	-7648.3	-7647.8
$1-^3\Pi_0$	-7600.2	-7569.1	-7602.6
$2-^3\Pi_0$	-7599.2	-7567.7	-7602.4
$1-^1\Sigma_0^+$	.3	.5	.0
$^3\Sigma_0^-$	4585.4	3685.2	3685.3
$^3\Sigma_1^-$	4585.5	3685.2	3685.4
$^1\Pi_1$	8172.7	7872.7	7871.9
$^1\Delta_1$	22017.7	20367.2	20367.0
$2-^1\Sigma_0^+$	36125.8	32307.5	32306.6

Adiabatic $1-^1\Sigma_0^+$ was chosen as the zero energy.

8. Summary and conclusions

General group-theoretical methods have been used to derive important selection rules for spin-orbit coupling matrix elements. Whereas some of the results have been known prior to this publication, some useful new procedures have been introduced, and as complete a symmetry analysis as possible has been presented. Selection rules for the spin-orbit coupling matrix elements have been given in terms of both double and point groups. The computational procedure for an efficient spin-orbit coupling code has been described and the results of parallel tests have been presented.

A typical spin-orbit coupling matrix is given in Appendix IV.

Acknowledgements

The authors wish to express their gratitude to Professors Michael Schmidt, Satoshi Yabushita, David Yarkony and Pekka Pyykkö for their helpful comments. The parallel calculations were performed on the Alice cluster, obtained via funds from the Ames Laboratory-USDOE and Iowa State University. This work was supported by the Ames Laboratory via the Department of Energy Basic Energy Sciences Office. Development of scalable codes was supported by a DoD software grant administered by the Air Force Office of Scientific Research.

Appendix I. Wigner functions

Wigner functions in the Euler angle representation can be calculated as follows[14]:

$$D^{j}_{mm'}(\alpha,\beta,\gamma) = \exp(-im\alpha - im'\gamma)d^{j}_{mm'}(\beta)$$

$$d^{j}_{mm'}(\beta) = (-1)^{j-m'}\sqrt{(j+m)!(j-m)!(j+m')!(j-m')!}\times \sum_{k=\min(j-m,j-m')}^{\max(-m-m',0)} (-1)^{k}\frac{\cos^{m+m'+2k}(\beta/2)\sin^{2j-m-m'-2k}(\beta/2)}{k!(j-m-k)!(j-m'-k)!(m+m'+k)!} \quad (28)$$

Appendix II. Arbitrary CI wavefunction symmetry labelling

While this labelling is a technical issue, it appears sufficiently important to be briefly outlined. The necessity for this lies in the fact that especially for non-Abelian point groups, existing CI implementations are not always able to assign symmetry labels to the states

obtained in a determinant-based calculation, such as CASSCF or MRCI. In particular, the non-Abelian GUGA approach does not appear to be widely used. Consider a wavefunction

$$\Psi = \sum_I C_I D_I \tag{29}$$

where D_I are the determinants and C_I the expansion coefficients. It is assumed that molecular spin-orbitals $\psi=\varphi\sigma$ in the determinants are already symmetry labelled. For simplicity the spin part σ is omitted in the equations below, except where relevant. The statement that Ψ does not belong to row a of irrep Γ is equivalent to:

$$P^{\Gamma a}\Psi = 0 \qquad \text{where P is a projection operator.} \tag{30}$$

$$P^{\Gamma a}\Psi = \frac{n^\Gamma}{n_g}\sum_g D^{\Gamma\,*}_{aa}(g) T_g \sum_I C_I \det\{\varphi_1 ... \varphi_N\}_I = \frac{n^\Gamma}{n_g}\sum_g D^{\Gamma\,*}_{aa}(g) \sum_I C_I \det\{T_g\varphi_1 ... T_g\varphi_N\}_I \tag{31}$$

Unless special measures are taken, φ will usually be labelled without a distinct row symmetry. This corresponds to mixing degenerate components, such as p_x and p_y for atoms. In order to find their transformation law, they can be decomposed into linear combinations of row-adapted functions. In the following, k_μ below simply numbers degenerate components, eg. one can assign k=1 for an orbital $\varphi = p_x+p_y$ and k=2 for p_x-p_y so k=1 does not imply pure p_x or p_y.

$$\varphi_\mu \equiv \varphi_\mu^{\Gamma_\mu k_\mu} = \sum_{\alpha=1}^{n^\Gamma} a^{\Gamma_\mu}_{\alpha k_\mu} \phi_\mu^{\Gamma_\mu \alpha} \quad and \quad \phi_\mu^{\Gamma_\mu \alpha} = \sum_{k_\mu=1}^{n^\Gamma} (a^{-1})^{\Gamma_\mu}_{k_\mu \alpha} \varphi_\mu^{\Gamma_\mu k_\mu}$$

$$T_g \phi_\mu^{\Gamma_\mu \alpha} = \sum_{\alpha'=1}^{n^\Gamma} D^{\Gamma_\mu}_{\alpha'\alpha}(g) \phi_\mu^{\Gamma_\mu \alpha'} = \sum_{\alpha'=1}^{n^\Gamma} D^{\Gamma_\mu}_{\alpha'\alpha}(g) \sum_{k_\mu=1}^{n^\Gamma} (a^{-1})^{\Gamma_\mu}_{k_\mu \alpha'} \varphi_\mu^{\Gamma_\mu k_\mu}$$

$$T_g \varphi_\mu^{\Gamma_\mu k_\mu} = \sum_{\alpha=1}^{n^\Gamma} a^{\Gamma_\mu}_{\alpha k_\mu} \sum_{\alpha'=1}^{n^\Gamma} D^{\Gamma_\mu}_{\alpha'\alpha}(g) \sum_{k_\mu=1}^{n^\Gamma} (a^{-1})^{\Gamma_\mu}_{k_\mu \alpha'} \varphi_\mu^{\Gamma_\mu k_\mu}$$

$$D'^{\Gamma_\mu}(g) = a^{-1} D^{\Gamma_\mu}(g) a \tag{32}$$

where ϕ transform according to row α of the irreducible representation $\Gamma$and the coefficients "a" will be found later. D' gives the transformation law in the new basis.

$$P^{\Gamma\alpha}\Psi = \frac{n^{\Gamma}}{n_g}\sum_g D^{\Gamma^*}_{aa}(g)\sum_I C_I \det\{T_g\varphi_1^{\Gamma_1 k_1}...T_g\varphi_N^{\Gamma_N k_N}\}_I$$

$$= \frac{n^{\Gamma}}{n_g}\sum_g D^{\Gamma^*}_{aa}(g)\sum_I C_I \sum_{k_1'} D'^{\Gamma_1}_{k_1' k_1}(g)...\sum_{k_N'} D'^{\Gamma_N}_{k_N' k_N}(g)\det\{\varphi_1^{\Gamma_1 k_1'}...\varphi_N^{\Gamma_N k_N'}\}_I \qquad (33)$$

Some of the determinants $\det\{\varphi_1^{\Gamma_1 k_1'}...T_g\varphi_N^{\Gamma_N k_N'}\}_I$ are linearly dependent. These are only the determinants which include degenerate MO's belonging to the same Γ_μ and only for certain combinations of spin functions, e.g., for doubly degenerate MOs

$\det\{...\varphi_1\alpha\varphi_2\alpha...\}$ *and* $\det\{...\varphi_2\alpha\varphi_1\alpha...\}$ arise from $T_g\det\{...\varphi_1\alpha\varphi_2\alpha...\}$

These linearly independent cases are small in number and are readily accounted for.

The weight of the irreducible representation Γ row α in the wavefunction Ψ is:

$$W^{\Gamma\alpha}[\Psi] = \sum_I \left| \frac{n^{\Gamma}}{n_g}\sum_J C_J[-1]^{I,J}\sum_g D^{\Gamma^*}_{aa}(g)D'^{\Gamma_1}_{k_1' k_1}(g)...D'^{\Gamma_N}_{k_N' k_N}(g)\right|^2 \qquad (34)$$

The sum over I runs over all determinants in Ψ and the sum over J runs over determinants generating linearly dependent determinants in D_I upon application of T_g. Unprimed indices correspond to orbitals found in D_I and primed indices are from D_J. $[-1]^{I,J}$ arises after an even (1) or odd (-1) permutation producing I from J.

Determinants to be included in the J sum are easy to identify, because they have the same orbital **and** spin occupancies except for one possible degree of freedom: MOs belonging to a degenerate Γ_μ can replace one another. So a determinant containing p_x, det $\{...p_x...\}$, can be reproduced upon rotation from a determinant with p_y in place of p_x, det $\{...p_y...\}$, and identical in other orbitals. It should be noted that Γ_μ is understood to include a label distinguishing equivalent irreps, such as 2 in $2p_x$, so that $2p_x$ does not interact with $3p_y$ in the above sense. For determinants containing a degenerate irrep, for MOs multiplied by the same spin function it is necessary to add determinants to J obtained from those in I by a permutation. This can be seen to correspond to restricting J to only determinants found in I

and replacing the product of D' matrix elements with det D'^{T}. Since the choice of J for a given I is crucial, the following examples should clarify the choice of J.

Consider a wavefunction consisting of only three determinants in C_{3v} (case A).

D_1=det{ $1a_1 1e_1 2\ a_1$ }

D_2=det{ $1\ a_1 1e_2 2\ a_1$ }

D_3=det{ $1\ a_1 1e_2 3\ a_1$ }

(for any spin occupancies)

The phases and determinants to be included into the J sum are given in Table 2.; I, J and $[-1]^{I,J}$ are defined as in the Eq. 34.

Table 2. Determinants and phase factors for Non-Abelian groups, case A.

I	J	$[-1]^{I,J}$
1	1	1
	2	1
2	1	1
	2	1
3	3	1

Another example involving negative phase might be (case B):

D_1=det{ $1\ a_1\alpha 1e_1\beta 1e_2\beta$ }

D_2=det{ $1\ a_1\alpha 1e_2\beta 2\ a_1\beta$ }

D_3=det{ $1\ a_1\beta 1e_2\beta 2\ a_1\alpha$ }

(1'≡ det{ $1\ a_1\alpha 1e_2\beta 1e_1\beta$ })

The phases and determinants are given in Table 3.

Table 3. Determinants and phase factors for Non-Abelian groups, case B.

I	J	$[-1]^{IJ}$
1	1	1
	1'	-1
2	2	1
3	3	1

Finally to find the necessary coefficients a, the following procedure can be used. Application of $P^{\Gamma\alpha}$ on the set $\varphi^{\Gamma k}$ produces either zero if $\varphi^{\Gamma k}$ has no projection in the space of Γ,α or $\varphi^{\Gamma\alpha}$ otherwise and $\varphi^{\Gamma\alpha}$ can be normalised for convenience. Functions $\varphi^{\Gamma\alpha}$ can be explicitly written in terms of atomic orbitals.

$$\varphi^{\Gamma k}(r) = \sum_{pst} c_{pst}^{\Gamma k} \chi_{ps}(r - R_t)$$
$$\phi^{\Gamma\alpha}(r) = \sum_{pst} C_{pst}^{\Gamma\alpha} \chi_{ps}(r - R_t) \qquad (35)$$

The index p corresponds to l (angular momentum quantum number) in case spherical harmonics are used or to the rank of the Cartesian direct product tensor (i.e., 1 for x, 2 for xy,z^2 etc) for real Cartesian basis sets, s being correspondingly m or denoting a component of the tensor of rank p. R_t stands for Cartesian corrdinates of atom t.

$$\phi^{\Gamma\alpha}(r) = \sum_{pst} C_{pst}^{\Gamma\alpha} \chi_{ps}(r - R_t) = P^{\Gamma\alpha}\varphi^{\Gamma k}(r) = \frac{n^{\Gamma}}{n_g} \sum_{pst} c_{pst}^{\Gamma k} \sum_{g} D_{aa}^{\Gamma\,*}(g) T_g \chi_{ps}(r - R_t) =$$
$$= \frac{n^{\Gamma}}{n_g} \sum_{pst} c_{pst}^{\Gamma k} \sum_{g} D_{aa}^{\Gamma\,*}(g) \sum_{s'} F_{s's}^{p}(g) \chi_{ps'}(r - gR_t) \qquad (36)$$

Matrices F(g) give the transformation law for χ. They are the Wigner functions for χ having angular dependence of spherical harmonics. For Cartesian angular dependence they can be explicitly written down with some algebra as linear combinations of Wigner functions.

$$C_{ps}^{\Gamma\alpha} = \frac{n^{\Gamma}}{n_g}\sum_{g} D_{aa}^{\Gamma\,*}(g)\sum_{s'} F_{ss'}^{p}(g)c_{ps',g^{-1}t}^{\Gamma k} \tag{37}$$

where $_{g^{-1}t}$ is understood to mean atom t' such that $R_{t'}=g^{-1}R_t$.

Using the orthonormality of $\langle\varphi^{\Gamma\alpha}|\varphi^{\Gamma\alpha'}\rangle = \delta_{\alpha\alpha'}$

$$\varphi^{\Gamma k} = \sum_{\alpha=1}^{n^{\Gamma}} a_{\alpha k}^{\Gamma}\phi^{\Gamma\alpha}$$
$$a_{\alpha k}^{\Gamma} = \langle\phi^{\Gamma\alpha}|\varphi^{\Gamma k}\rangle \tag{38}$$

Appendix III. Clebsch-Gordan coefficient relations

The following relations used above can be readily proved by using the properties of 3j Wigner symbols[7].

$$(S,1,M_s-1,1|S,M_s) = (-1)^{S-1+M_s}\sqrt{2S+1}\begin{pmatrix} S & 1 & S \\ M_s-1 & 1 & -M_s \end{pmatrix}$$

$$(S,1,M_s,-1|S,M_s-1) = (-1)^{S-1+M_s-1}\sqrt{2S+1}\begin{pmatrix} S & 1 & S \\ M_s & -1 & -(M_s-1) \end{pmatrix}$$

$$= (-1)^{S-1+M_s-1}\sqrt{2S+1}(-1)^{2S+1}\begin{pmatrix} S & 1 & S \\ -M_s & 1 & M_s-1 \end{pmatrix}$$

$$= (-1)^{S-1+M_s-1}\sqrt{2S+1}(-1)^{2S+1}(-1)^{2S+1}\begin{pmatrix} S & 1 & S \\ M_s-1 & 1 & -M_s \end{pmatrix}$$

$$= -(-1)^{S-1+M_s}\sqrt{2S+1}\begin{pmatrix} S & 1 & S \\ M_s-1 & 1 & -M_s \end{pmatrix} = -(S,1,M_s-1,1|S,M_s)$$

And similarly,

$$(S+1,1,M_s+1,-1|S,M_s) = (-1)^{S+1-1+M_s}\sqrt{2S+1}\begin{pmatrix} S+1 & 1 & S \\ M_s+1 & -1 & -M_s \end{pmatrix}$$

$$(S+1,1,-M_s-1,1|S,-M_s) = (-1)^{S+1-1-M_s}\sqrt{2S+1}\begin{pmatrix} S+1 & 1 & S \\ -M_s-1 & 1 & M_s \end{pmatrix}$$

$$= (-1)^{S+1-1-M_s}\sqrt{2S+1}(-1)^{S+1+1+S}\begin{pmatrix} S+1 & 1 & S \\ M_s+1 & -1 & -M_s \end{pmatrix}$$

$$= (-1)^{M_s - M_s} (-1)^{S+1-1-M_s} \sqrt{2S+1} (-1)^{S+1+1+S} \begin{pmatrix} S+1 & 1 & S \\ M_s+1 & -1 & -M_s \end{pmatrix}$$

$$= (-1)^{S+1+1+S-2M_s} (-1)^{S+1-1+M_s} \sqrt{2S+1} \begin{pmatrix} S+1 & 1 & S \\ M_s+1 & -1 & -M_s \end{pmatrix}$$

$$= (-1)^{S+1-1+M_s} \sqrt{2S+1} \begin{pmatrix} S+1 & 1 & S \\ M_s+1 & -1 & -M_s \end{pmatrix} = \left(S+1,1,M_s+1,-1 \middle| S,M_s\right)$$

where $S+1+1+S-2M_s$ is always an even number as S and M_s are both integers or half-integers.

Appendix IV. Detailed structure of the H_{so} matrix

As pointed out above, the matrix is tridiagonal and only two matrix elements need to be calculated explicitly. The detailed structure is provided below, the cases of equal and different multiplicities are given separately in Table 4 and Table 5. The orbital part is assumed to be different for the two states. The only two matrix elements which are explicitly calculated are A and B, the rest are obtained from these two.

Table 4. H_{so} matrix for equal multiplicities.

	S	S-1	S-2	...	← M_s'
S	A	-B*	0	0	0
S-1	B	aA	-bB*	0	0
S-2	0	bB*	...	...	0
...	0	0	...	...	...
M_s ↑	0	0	0	...	...

A,B – calculated matrix elements, while a and b are Clebsch-Gordan coefficients:

$a \equiv (S,1,S-1,0|S,S-1)/(S,1,S,0|S,S)$ and $b \equiv (S,1,S-1,-1|S,S-2)/(S,1,S,-1|S,S-1)$

"... " denote further propagation of A and B by means of equation (7).

Table 5. H_{so} matrix for different multiplicities.

	S+1	S	S-1	...	$\leftarrow M_s' \rightarrow$	-S	-S-1
S	B	A	bB*	0	0	0	0
S-1	0	aB	cA	...	0	0	0
S-2	0	0	...	...	...	0	0
$M_s \uparrow$	0	0	0	...	...	...	0
-S	0	0	0	0	...	...	B*

A,B – calculated matrix elements and a,b,c are Clebsch-Gordon coefficients:

$a \equiv (S+1,1,S,-1|S,S-1)/(S+1,1,S+1,-1|S,S)$, $b \equiv (S+1,1,S-1,1|S,S)/(S+1,1,-S-1,1|S,-S)$

$c \equiv (S+1,1,S-1,0|S,S-1)/(S+1,1,S,0|S,S)$

References

[1] Yarkony DR, J Phys Chem A (1997) 101:4263

[2] Yarkony DR, Int Rev in Phys Chem (1992) Vol II No 2, 195-242

[3] Yarkony DR, J Chem Phys (1986) 84: 2075

[4] Koseki S, Gordon MS, Schmidt MW, Matsunaga N (1995) J Phys Chem 99:12764

[5] Furlani TR (1984) PhD Thesis, SUNY

[6] Bethe HA, Salpeter EE (1977), Quantum Mechanics of the one and two electron atoms. New York, Plenum

[7] Brink DM, Satchler GR (1968), Angular Momentum. Charedon Press, Oxford

[8] Yarkony DR (1995), Modern Electronic Structure Theory. World Scientific, 174ff

[9] many symmetry related references can be found in:

Pyykkö P (1986), Relativistic Theory of Atoms and Molecules, A bibliography 1916-1985. Springer Verlag. (1993) *idem*, 1986-1992.

[10] Balasubramanian K (1997), Relativistic Effects In Chemistry. John Wiley, New York.

[11] Schmidt MW, Baldridge KK, Boatz JA, Elbert ST, Gordon MS, Jensen JH, Koseki S, Matsunaga N, Nguyen KA, Su SJ, Windus TL, Dupuis M, Montgomery JA (1993), J Comput Chem 14:1347

[12] Dunning TH, Hay PJ (1977), J Chem Phys 66:3767

Cohen JS, Wadt WR, Hay PJ (1979) J Chem Phys 71:2955

[13] http://www.scl.ameslab.gov

[14] Warshalovich DA, Moskalev LN, Kersunski VK (1975), Quantum theory of angular momentum. Nauka, Moscow

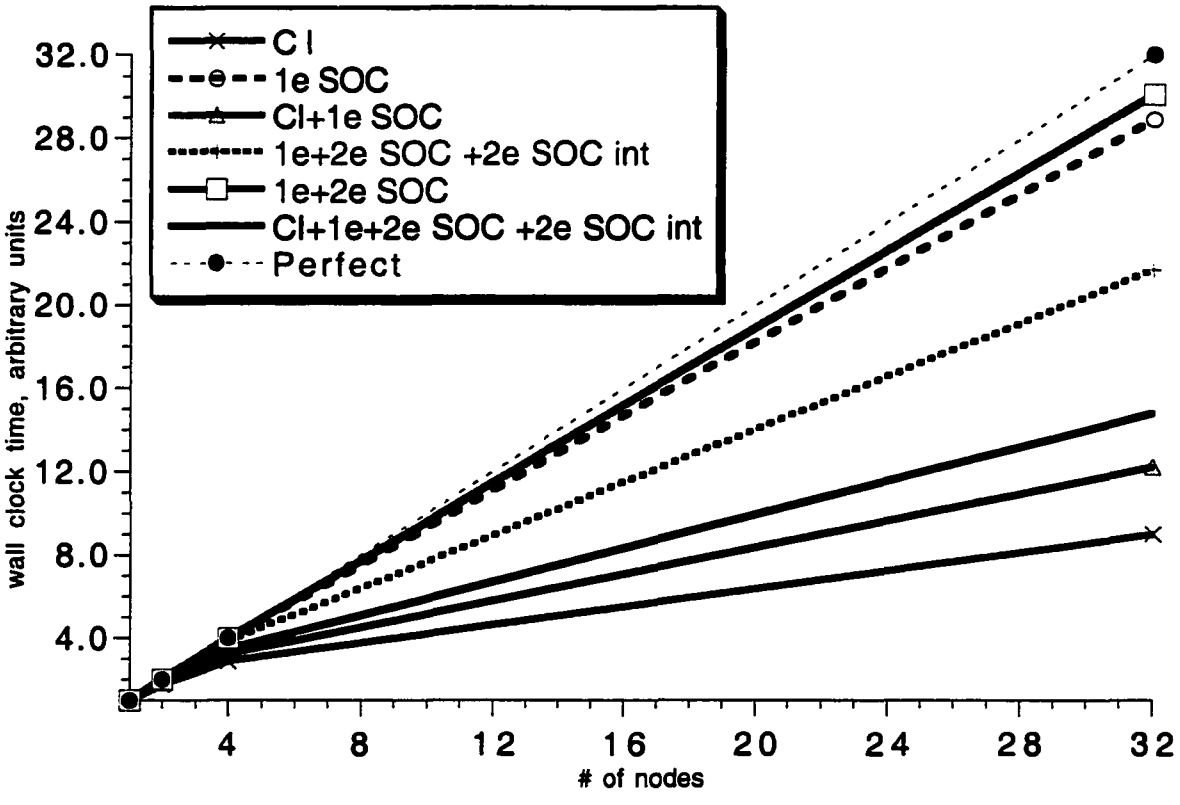

Figure 1. Scalability of SOC code

CHAPTER IV. STUDY OF THE VIBRATIONAL STRUCTURE

1. Introduction

It is possible to measure vibrational and rotational structure very accurately[1],[2]. In ab initio studies several approximations are made as the exact solution is in general not possible. The basic approximation inherent to many theoretical studies is the already mentioned adiabatic approximation, where the independence of electronic and nuclear movement is enforced. An independence of rotational, vibrational and electronic structure is often enforced as well, and rotations and vibrations are frequently treated with the rigid rotor-harmonic oscillator approximations. These approximations provide a backbone for the further refinement of the methods via the reintroduction of the neglected interactions, as simplified models allow for a general and analytical solution to be found. The nuclear wavefunction obtained as a result of these approximations is used to obtain the vibrational structure of the molecules so that a comparison of theoretical predictions and experimental measurements can be made.

2. Vibrational wavefunction

In the adiabatic approximation, the total wavefunction is separated into a product of electronic and nuclear parts:

$$\Psi_{tot}(r_e, R_N) = \Psi_N(R_N)\Psi_e(r_e, R_N)$$

The conventional quantum-chemical application codes focus on accurate calculation of the electronic wavefunction $\Psi_e(r_e, R_N)$. Exact analytical calculation of the vibrational

wavefunction $\Psi_N(R_N)$ does not appear to be possible in general, so approximations need to be made.

The relative magnitude of rotational (small) and vibrational (large) interaction allows one to take the total wavefunction as a product of the rotational and vibrational parts. The rotational part is usually treated in the rigid rotor approximation and in this Chapter the rotational wavefunction is taken to be unchanged, i.e., the rotational motion is neglected.

For the vibrational wavefunction, several approaches can be taken. For diatomic molecules there is only one vibrational degree of freedom, and several analytical models can be solved exactly, most notably, the harmonic oscillator model and the Morse potential model (an anharmonic oscillator). For a molecule with more than two atoms one can conceivably take a model of non-interacting harmonic or anharmonic oscillators with further addition of coupling terms. Such a treatment provides immense benefits of analytical solutions, while an alternative approach of numerical solution for vibrational eigenfunctions of a potential energy surface calculated numerically on a grid leaves the sensation of physical interpretation vanishing into "thin air".

Yet alternatively to these ab initio approaches one can retreat to the misleading safety of a semiempirical approach, where for each vibrational level one extracts the geometry R_N from the experiment by means of $\langle R_N \rangle = \frac{\hbar}{\sqrt{2\mu B}}$. This approach, however, can work only if the true vibrational wavefunction resembles the Dirac delta function with a peak at $R=R_N$. This is usually true only for the first few vibrational quantum numbers, in which case all analytical methods as well as this semi-empirical one converge to the vicinity of the same answer (provided that the $\Psi_e(r_e, R_N)$ is obtained at the same level of theory) as seen in the numerical examples below.

The harmonic oscillator model works well only near the equilibrium and in the dissociation limit it behaves incorrectly. Since the Morse potential model is not much more complicated and it does describe the potential energy up to the dissociation limit properly, only this model is studied further. A comparison of Morse and harmonic potentials is given in Table 1.

Table 1. Morse Potential vs Harmonic Potential[3].

	Harmonic	Morse
Potential	$U(r) = k\frac{(r-R_e)^2}{2}$	$U(r) = D_e\left(1-e^{-a(r-R_e)}\right)^2$
Energy	$E_\upsilon = \hbar\omega_e\left(\upsilon+\frac{1}{2}\right)$	$E_\upsilon = \hbar\omega_e\left(\upsilon+\frac{1}{2}\right) - \hbar\omega_e x_e\left(\upsilon+\frac{1}{2}\right)^2$
Eigen-function	$\Psi_{\upsilon lm}(r,\vartheta,\phi) = e^{-\alpha z^2/2}H_\upsilon(\sqrt{\alpha}z)Y_{lm}(\vartheta,\phi)$ $\alpha = \frac{\omega_e\mu}{\hbar}$ $z = r - R_e$	$\Psi_{\upsilon lm}(r,\vartheta,\phi) = e^{-z/2}z^{b_\upsilon/2}L_\upsilon^{b_\upsilon}(z)Y_{lm}(\vartheta,\phi)$ $b_\upsilon = \sqrt{\frac{2\mu(D_e-E_\upsilon)}{a}}$ $z = 2\sqrt{\frac{2\mu D_e}{a}}e^{-a(r-R_e)}$
Polynomials	Hermite	Associated Laguerre
Constants	$\omega_e = \sqrt{\frac{k}{\mu}}$	$\omega_e = 2a\hbar\sqrt{\frac{D_e}{2\mu}}$ $\quad$ $\omega_e x_e = \frac{a^2\hbar^2}{2\mu}$
Applicable	near the equilibrium	except r→0 (not infinite)

Thus two methods are studied and compared, a semiempirical method in which the vibrational wavefunction is sharply peaked at the empirically determined geometry (single point method) and an ab initio method, in which the vibrational wavefunction is taken to be an eigenfunction of the Morse potential (Morse potential method). The latter case is used

only for diatomic molecules and in order to accurately obtain the wavefunction, a series of single point energy calculations at a set of internuclear distances is performed with high accuracy. For the numerical examples below, this means a sufficiently good basis set and either SOCI or multi-reference CI (MRSD) electronic wavefunction (SOCI plus single and double excitations from the core into the virtual space), both based on all-valence CAS. The obtained energy values are then least square fit to a Morse potential. From the fit one can calculate $\Psi_N^v(R)$ and then proceed to calculate the properties of interest.

This does not exceed all possibilities. The RKR method[4] can be used to estimate the turning points from the empirical data, thus reconstructing the energy curve. Both this empirical curve and the ab initio curve can be used to obtain numerical solutions (eigenvectors) of the vibrational Schrödinger equation. An improvement for the single point method would be to depart from the rigid rotor approximation for the relation between the rotational constant and the averaged internuclear distance. It is known that for some molecules the Morse potential does not work very well[5] and other functional forms can be tried. The problem with other forms is that the wavefunctions may not be found analytically. Since the Morse potential works well for the molecules considered, no other form has been studied here.

The empirical Morse curve can be used to obtain the empirical vibrational wavefunction integrated with the ab initio spin-orbit splitting A(R) this would yield yet another semi-empirical approach. It is thought however that the main reason for the discrepancy between the experimental and ab initio levels are the first-order perturbative treatment, the absence of spin-spin interaction and the deficiencies in the electron correlation.

3. Properties as a function of the vibrational number

With either a semi-emprical or ab initio vibrational wavefunction and ab initio electronic wavefunction the properties are straightforward to obtain for an operator $\hat{A}$:

$$\Psi^{\upsilon}_{total}(r,R) = \Psi^{\upsilon}_{N}(R)\Psi_{e}(r,R)$$

$$A_{\upsilon} = \iint \left[\Psi^{\upsilon}_{N}(R)\Psi_{e}(r,R)\right]^{+} \hat{A}(r)\Psi^{\upsilon}_{N}(R)\Psi_{e}(r,R)drdR =$$

$$\int \Psi^{\upsilon +}_{N}(R)\left[\int \Psi^{+}_{e}(r,R)\hat{A}(r)\Psi_{e}(r,R)dr\right]\Psi^{\upsilon}_{N}(R)dR =$$

$$\int \Psi^{\upsilon +}_{N}(R)A(R)\Psi^{\upsilon}_{N}(R)dR$$

In the case of spin-orbit coupling, one is often interested in splitting, i.e. difference between two spin-orbit coupled diabatic levels (eigenvectors of $\hat{A} = \hat{H}_{so}$). In this case in order for A(R) to be the splitting, two eigenvectors $\Psi'_{e}(r,R)$ and $\Psi''_{e}(r,R)$ of the H_{so} matrix corresponding to the two levels are introduced.

$$A(R) \equiv \int \Psi'^{+}_{e}(r,R)\hat{A}(r)\Psi'_{e}(r,R)dr - \int \Psi''^{+}_{e}(r,R)\hat{A}(r)\Psi''_{e}(r,R)dr$$

The quantity denoted by A(R) is calculated by the developed spin-orbit coupling code with the electronic wavefunction and for a few representative values of R. Thus the A(R) is obtained for a few single points on a grid. In order to integrate A(R) with $\Psi^{\upsilon}_{N}(R)$ it is convenient to interpolate (least square fit) these values of A(R) with an analytical function. The form of this analytical function is individually tailored for each molecule as there appears to be no exact analytical functional dependence of A upon R in general. Certainly, in the limit of $R \rightarrow \infty$, one should expect to arrive at the SOC values for two separate atoms, however even in that case there appears to be no closed form analytical solution for A(R) in the case of CI electronic wavefunctions.

Once the functional form of A(R) is determined, a number of numerical intergrations for the desired values of υ are performed. Depending on the form of A(R), an analytical

integration may also be possible, although the associated Laguerre polynomials appearing in the vibrational wavefunction present some difficulty in taking analytical integrals. The resultant values of A_v can be directly compared with the experiment. The Morse potential parameters such as dissociation energy and equilibrium internuclear distance are also compared with the experimental values.

4. Vibronic coupling model

While analysing the experimental data, one is sometimes able to observe small jumps in spin-orbit coupling as a function of the vibrational number. These jumps are attributed to the coupling between different electronic states because at the averaged geometries corresponding to these vibrational states, the two (or more) potential energy surfaces of these states come close (or intersect) interacting by means of diabatic coupling potentials, such as spin-orbit coupling (and others). Again, two approaches can be tried.

The first approach is the single point approach, where the electronic states thought to couple are calculated at the same geometry. The problems associated with this approach are two-fold. The first is the inherent anharmonicity of the potential energy surface, and the second is the problem of having to accurately calculate several electronic states at once. While there are general difficulties in treating excited states, another impedence is that they need to be obtained in one calculation, which is frequently done with CAS state-averaged orbitals and further large CI expansion.

A simple modification of the Morse approach allows for immediate calculation of the vibronic coupling as follows. The electronic H_{so} matrix as a function of the internuclear distance is precalculated in the basis of the electronic states of interest. This matrix generalises the previously introduced single constant A(R). Then a vibronic matrix is

constructed in the basis of the $\Psi^{\upsilon}_{total}(r,R) = \Psi^{\upsilon}_{N}(R)\Psi_{e}(r,R)$, as before except that now several of these are included for each electronic state with a desired vibrational number and $\Psi_{e}(r,R)$ is now the adiabatic wavefunctions.

$$A^{vibso}_{e\upsilon,e'\upsilon'} = \iint\left[\Psi^{\upsilon}_{N}(R)\Psi_{e}(r,R)\right]^{+}\hat{H}_{so}(r)\Psi^{\upsilon'}_{N}(R)\Psi_{e'}(r,R)drdR =$$

$$\int\Psi^{\upsilon+}_{N}(R)\left[\int\Psi^{+}_{e}(r,R)\hat{H}_{so}\Psi_{e'}(r,R)dr\right]\Psi^{\upsilon'}_{N}(R)dR = \int\Psi^{\upsilon+}_{N}(R)A_{ee'}(R)\Psi^{\upsilon'}_{N}(R)dR$$

where the label e denotes an electronic state.

The resultant (complex-valued) matrix $A^{vibso}_{e\upsilon,e'\upsilon'}$ is then diagonalised and the eigenvectors of this matrix give vibronically coupled states. It is thought that usually only a few vibrational numbers (of the order of two) need to be coupled, thus this matrix is very small-dimensional. Note the subtle point: the vibrational wavefunction is optimised solely for the term of interest (via the Morse potential parameters) whereas $A_{ee'}(R)$ is necessarily calculated from a multi-state calculation where some accuracy is sacrificed due to having to treat several states simultaneously.

The splitting between the eigenvalues of the $A^{vibso}_{e\upsilon,e'\upsilon'}$ matrix gives then an estimate of the vibronically coupled spin-orbit splitting with the Morse potential approach.

5. Results and discussion

Two molecules CO^{+} and O_2^{+} are studied both experimentally and theoretically as described in Chapter VI, where all computational details are given. In Figure 1 and 2 the experimental energy levels for CO^{+} are given. In Figure 3 similar data are given for the averaged levels of O_2^{+}. The experimental date fit the Morse potential levels perfectly.

Figure 4 and Figure 5 show the reconstructed experimental Morse curve (i.e., the curve is plotted with least square fir Morse potential parameters) and the theoretical predicted

single geometry energies and the fitted Morse potential curve. Again the Morse potential fits the theoretical data nicely. Since the CO^+ results were obtained with a less correlated wavefunction one can see that the data deviate from the curve near the dissociation limit. This does not occur with O_2^+. The spin-orbit coupling splitting A(R) displayed in Figure 6 and Figure 7 appears to have a different shape for the two molecules studied. Two different functional forms were used to obtain an analytic for A(R). The jump near 1.484Å on the CO^+ curve is due to potential curve crossing between $^2\Pi$ and $^2\Sigma^+$ terms and the value of A(R) is overestimated due to optimisation of the orbitals for $^2\Pi$ term only. The values of A(R) at small values of R (<1 Å) are difficult to obtain due to strong repulsion of the nuclei. It is seen from the pictures that the values of A(R) for CO^+ significantly deviate from the analytic function at small internuclear distances. However the vibrational wavefunction has small weight in that area so this deviation does not cause significant error in the numerical integration afterwards.

References

[1] D. G. Fedorov, M. Evans, Y. Song, M. S. Gordon, and C. Y. Ng, submitted to J. Chem.Phys.

[2] A. J. Orr-Ewing, W. R. Simpson, T. P. Rakitzis, S. A. Kandel and R. N. Zare, J. Chem. Phys. **106**, 5961 (1997).

[3] C. S. Johnson, Jr. and L. G. Pederson, Problems and solutions in Quantum Chemistry and Physics (Dover, New York, 1986).

[4] J. I. Steinfeld, Molecules and Radiation (Harper&Row,New York,1974).

[5] D. Steele, E. R. Lippincott and J. T. Vanderslice, Rev. Mod. Phys **34**, 239 (1962).

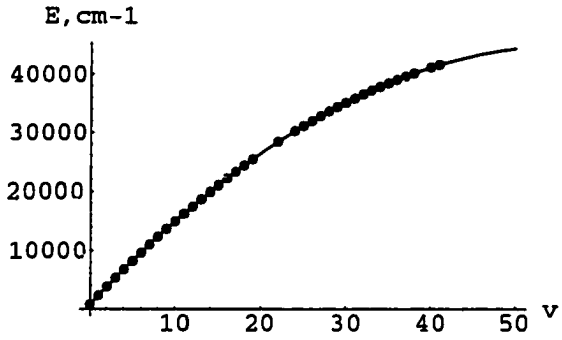

Figure 1. Experimental Energy levels CO^+, $A^2\Pi_{1/2}$

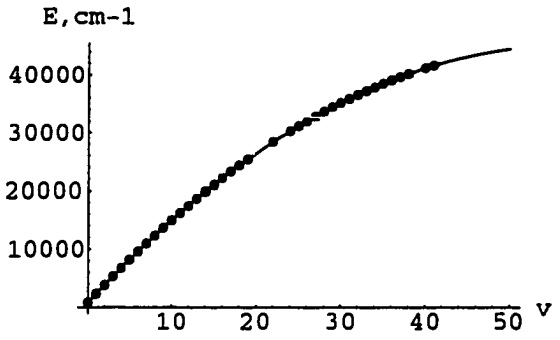

Figure 2. Experimental Energy levels CO^+, $A^2\Pi_{3/2}$

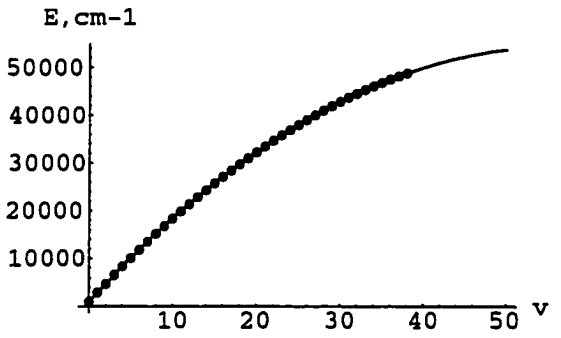

Figure 3. Experimental Energy levels O_2^+, $X^2\Pi_g$

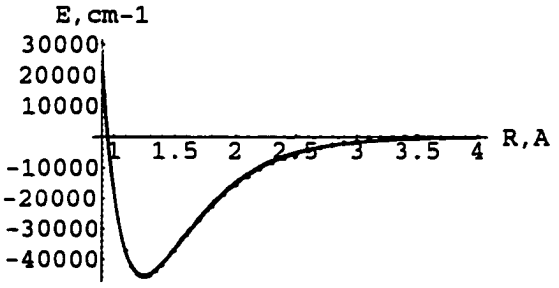

Figure 4. Experimental (no dots) and theoretical (filled dots) curves for CO^+

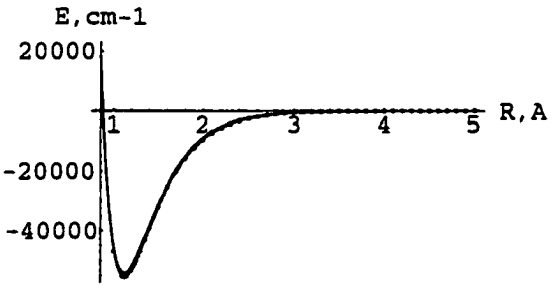

Figure 5. Experimental (no dots) and theoretical (filled dots) curves for O_2^+

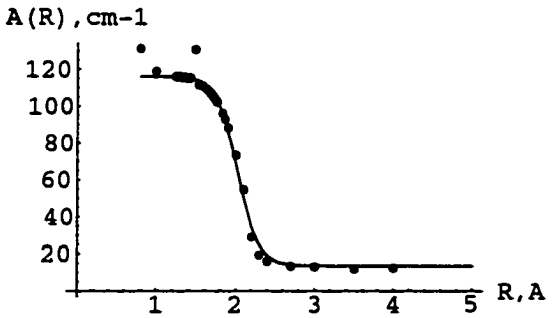

Figure 6. Ab initio splitting for CO^+

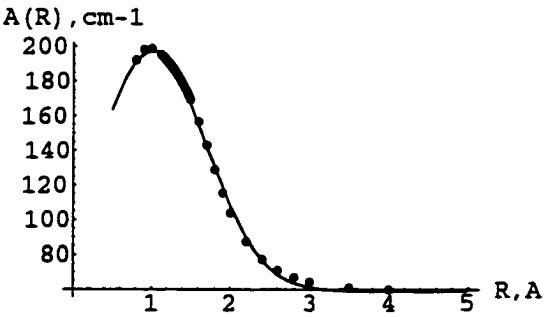

Figure 7. Ab initio splitting for O_2^+

CHAPTER V. DIABATIC PROPERTIES

1. Introduction

In this chapter, the derivation and description of quantities of chemical interest computed from or along with spin-orbit coupling are given. The approach to SOC taken in this work can best be described as quasi-degenerate perturbation theory, because a few quasi-degenerate CI roots are segregated from the rest, and the degenerate perturbative formalism is used to obtain the perturbed eigenvalues and eigenvectors of the H_{so} matrix in this set of CI roots. The usual perturbative approach would in fact produce no correction to the eigenvalues, as the matrix element between the same state is zero by Hermiticity (provided that the states are real-valued!) However, the first order perturbed eigenfunction could be calculated, provided that one knows all states of the system; their number is equal to the number of CSFs for each multiplicity. This is a resource-consuming task. It should be noted that the orbitals are optimised for a specific CI root, so these excited state eigenvalues may not be sensible. This problem has been recognised[1], and one solution is to include SOC into the zeroth-order Hamiltonian; i.e., forsake the perturbative treatment in favour of what is known as spin-orbit CI[2]. This has additional benefits: one can include other non-adiabatic operators, and since the perturbation treatment breaks down for a large perturbation (heavy elements) the non-perturbative treatment is the preferred approach.

In the quasi-adiabatic approach discussed below the expense of the non-perturbative approach is avoided. The eigenvectors of the H_{so} matrix couple adiabatic states, and thus they represent diabatic states. The eigenectors thus obtained can be used to obtain diabatic properties, given a quantity of interest with corresponding operator $\hat{A}$.

Two quantities are considered below: dipole moments and the z-axis component of the total angular momentum.

2. One-electron spin-independent operator (e.g. dipole moment)

A diabatic matrix element of a one-electron spin-independent operator may be expressed as:

$$\begin{aligned}\left\langle \Psi_I \middle| \hat{A} \middle| \Psi_J \right\rangle &= \sum_{n\Gamma\alpha S M_s} \sum_{n'\Gamma'\alpha'S'M_s'} \left(a^I_{n\Gamma\alpha S M_s}\right)^* a^J_{n'\Gamma'\alpha'S'M_s'} \left\langle n\Gamma\alpha S M_s \middle| \hat{A} \middle| n'\Gamma'\alpha'S'M_s' \right\rangle \\ &= \sum_{n\Gamma\alpha S M_s} \sum_{n'\Gamma'\alpha'} \left(a^I_{n\Gamma\alpha S M_s}\right)^* a^J_{n'\Gamma'\alpha' S M_s} \left\langle n\Gamma\alpha S \middle| \hat{A} \middle| n'\Gamma'\alpha'S \right\rangle\end{aligned} \tag{1}$$

where Ψ_I denotes a diabatic state and $a^I_{n\Gamma\alpha S M_s}$ denote complex-valued H_{so} eigenvector expansion coefficients in terms of adiabatic states. Since the operator $\hat{A}$ is spin-free, the spin part can be summed over by using the orthonormality of the states. The point group selection rules can be applied to reduce the number of calculated matrix elements $\left\langle n\Gamma\alpha S \middle| \hat{A} \middle| n'\Gamma'\alpha'S \right\rangle$.

The original dipole moment code was written for GAMESS by Koseki. No additional dipole moment calculations have been performed in this work.

3. Spin-dependent J_z operator

The following quantity is useful for labelling the diabatic states for linear molecules and atoms.

$$\begin{aligned}\left\langle \Psi_I \middle| \hat{A} \middle| \Psi_J \right\rangle &= \sum_{n\Gamma\alpha S M_s} \sum_{n'\Gamma'\alpha'S'M_s'} \left(a^I_{n\Gamma\alpha S M_s}\right)^* a^J_{n'\Gamma'\alpha'S'M_s'} \left\langle n\Gamma\alpha S M_s \middle| \hat{L}_z + \hat{S}_z \middle| n'\Gamma'\alpha'S'M_s' \right\rangle \\ &= \sum_{n\Gamma\alpha S M_s} \sum_{n'\Gamma'\alpha'} \left(a^I_{n\Gamma\alpha S M_s}\right)^* a^J_{n'\Gamma'\alpha' S M_s} \left\langle n\Gamma\alpha S \middle| \hat{L}_z \middle| n'\Gamma'\alpha'S \right\rangle + \sum_{n\Gamma\alpha S M_s} \left(a^I_{n\Gamma\alpha S M_s}\right)^* a^J_{n\Gamma\alpha S M_s} M_s\end{aligned} \tag{2}$$

In the SOC calculations of linear molecules the eigenvalue of the $\hat{J}_z$ operator, M_J is a good quantum number. The absolute value of this number (the states are doubly degenerate except for M_J=0) is put into the subscript of the diabatic Russell-Sanders terms, ${}^{2S+1}\Gamma \rightarrow {}^{2S+1}\Gamma_{M_J}$, where Γ is the irreducible representation label, such as Σ, Δ etc.

4. Transitions between adiabatic levels

In the limit of linear diabatic terms, constant diabatic coupling, etc, in the semi-classical Landau-Zener model[3] of two-state nonadiabatic transitions, the probability of transition between two adiabatic levels i and j is given by:

$$P(i,j) = 1 - e^{-2\delta} \qquad \delta = \pi \frac{|V_{ij}|^2}{\hbar v |g_i - g_j|} \tag{3}$$

where g is the adiabatic energy gradient, v is the velocity and V_{ij} is a matrix element of a diabatic operator coupling two adiabatic state i and j.

The matrix element V_{ij} in the case of spin-orbit coupling is better denoted by multiplicity labels, thus the notation is changed to P(S,S') and the matrix element to H_{so}(S,S'). Since the levels are degenerate, it is necessary to sum over the spin-degenerate adiabatic levels and the sum needs to be normalised by the number of spin-degenerate levels. Since these expressions have not been published previously, their derivations are presented here.

First, the derivation of the quantity given above in Eq. (II.2) is given separately for equal and different multiplicities. As already pointed out, due to symmetry the constant $C_{S,S'}$ is equal to zero unless $|S-S'| \leq 1$. Secondly, $C_{S,S'}=C_{S',S}$, thus there are two distinct cases, S'=S and S'=S+1 considered next.

During the derivations the properties of Clebsch-Gordan coefficients are used[4].

(i) S=S'

$$C_{S,S} \equiv \sum_{M_s=-S}^{S}\sum_{M_s'=-S}^{S}\left|\left\langle SM_s\left|\hat{H}_{so}\right|SM_s'\right\rangle\right|^2 = \sum_{M_s=-S}^{S}\left|\left\langle SM_s\left|\hat{H}_{so}\right|SM_s\right\rangle\right|^2 + 2\sum_{M_s=-S}^{S-1}\left|\left\langle SM_s\left|\hat{H}_{so}\right|SM_s+1\right\rangle\right|^2 \quad (4)$$

by using tridiagonal structure of H_{so} matrix and the subdiagonal symmetry.

$$C_{S,S} = \sum_{M_s=-S}^{S}\left|\left(S,M_s,1,0|S,M_s\right)\left\langle S\left|\hat{\mathcal{L}}_z\right|S\right\rangle\right|^2 + \sum_{M_s=-S}^{S-1}\left(S,M_s+1,1,-1|SM_s\right)^2\left\{\left|\left\langle S\left|\hat{\mathcal{L}}_x\right|S\right\rangle\right|^2 + \left|\left\langle S\left|\hat{\mathcal{L}}_y\right|S\right\rangle\right|^2\right\} \quad (5)$$

These Clebsch-Gordan coefficients are simplified to:

$$\begin{gathered}\left(S,M_s,1,0|S,M_s\right) = (-1)^{S-1+M_s}\sqrt{2S+1}\begin{pmatrix} S & 1 & S \\ M_s & 0 & -M_s\end{pmatrix} = (-1)^{S-1+M_s}\sqrt{2S+1}\begin{pmatrix} S & S & 1 \\ -M_s & M_s & 0\end{pmatrix} = \\ (-1)^{S-1+M_s}\sqrt{2S+1}(-1)^{S+M_s}\frac{(-M_s)}{\sqrt{S(S+1)(2S+1)}} = \frac{M_s}{\sqrt{S(S+1)}}\end{gathered} \quad (6)$$

and

$$\begin{gathered}\left(S,M_s+1,1,-1|S,M_s\right) = (-1)^{S-1+M_s}\sqrt{2S+1}\begin{pmatrix} S & 1 & S \\ M_s+1 & -1 & -M_s\end{pmatrix} = \\ (-1)^{S-1+M_s}\sqrt{2S+1}(-1)^{2S+1}\begin{pmatrix} S & 1 & 1 \\ -M_s-1 & 1 & M_s\end{pmatrix} = \\ (-1)^{S+M_s}\sqrt{2S+1}(-1)^{2S}(-1)^{S-M_s}\sqrt{\frac{(S-M_s)(S+M_s+1)}{2S(S+1)(2S+1)}} = \sqrt{\frac{(S-M_s)(S+M_s+1)}{2S(S+1)}}\end{gathered} \quad (7)$$

Since the L matrix elements do not depend upon M_s the sum of Clebsch-Gordan coefficients yields:

$$\begin{gathered}\sum_{M_s=-S}^{S}\left|\left(S,M_s,1,0|S,M_s\right)\right|^2 = \frac{1}{S(S+1)}\sum_{M_s=-S}^{S}M_s^2 = \frac{1}{S(S+1)}2\sum_{M_s=1}^{S}M_s^2 = \\ \frac{1}{S(S+1)}2\frac{S(S+1)(2S+1)}{6} = \frac{2S+1}{3}\end{gathered} \quad (8)$$

and

$$\begin{gathered}\sum_{M_s=-S}^{S-1}\left(S,M_s+1,1,-1|SM_s\right)^2 = \sum_{M_s=-S}^{S-1}\frac{(S-M_s)(S+M_s+1)}{2S(S+1)} = \\ \frac{1}{2S(S+1)}\sum_{M_s=-S}^{S}(S-M_s)(S+M_s+1) - \frac{1}{2S(S+1)}(S-M_s)(S+M_s+1)\Big|_{M_s=S} = \\ \frac{1}{2S(S+1)}\sum_{M_s=-S}^{S}(S-M_s)(S+M_s+1) = \frac{1}{2S(S+1)}\sum_{M_s=-S}^{S}\left(S^2+S\right) - M_s^2 - M_s =\end{gathered}$$

$$\frac{1}{2S(S+1)}\left\{(S^2+S)(2S+1)-2\frac{S(S+1)(2S+1)}{6}\right\}=\frac{2S+1}{3} \tag{9}$$

Thus, by combining equations (5), (8) and (8) one gets:

$$C_{S,S}=\frac{2S+1}{3}\left|\left\langle S\left|\hat{\mathcal{L}}_z\right|S\right\rangle\right|^2+\frac{2S+1}{3}\left\{\left|\left\langle S\left|\hat{\mathcal{L}}_x\right|S\right\rangle\right|^2+\left|\left\langle S\left|\hat{\mathcal{L}}_y\right|S\right\rangle\right|^2\right\}=$$
$$\frac{2S+1}{3}\left\{\left|\left\langle S\left|\hat{\mathcal{L}}_x\right|S\right\rangle\right|^2+\left|\left\langle S\left|\hat{\mathcal{L}}_y\right|S\right\rangle\right|^2+\left|\left\langle S\left|\hat{\mathcal{L}}_z\right|S\right\rangle\right|^2\right\}\equiv\frac{2S+1}{3}\left|\left\langle S\left|\hat{\mathcal{L}}\right|S\right\rangle\right|^2 \tag{10}$$

(ii) S'=S+1

$$C_{S,S+1}\equiv\sum_{M_s=-S}^{S}\sum_{M_s'=-S-1}^{S+1}\left|\left\langle SM_s\left|\hat{H}_{so}\right|S+1M_s'\right\rangle\right|^2=\sum_{M_s=-S}^{S}\left|\left\langle SM_s\left|\hat{H}_{so}\right|S+1M_s\right\rangle\right|^2+2\sum_{M_s=-S}^{S}\left|\left\langle SM_s\left|\hat{H}_{so}\right|S+1M_s+1\right\rangle\right|^2 \tag{11}$$

Again, the tridiagonal structure and subdiagonal symmetry are used.

$$C_{S,S+1}=\sum_{M_s=-S}^{S}\left|\left(S+1,M_s,1,0\middle|SM_s\right)\left\langle S\left|\hat{\mathcal{L}}_z\right|S+1\right\rangle\right|^2+$$
$$\sum_{M_s=-S}^{S}\left(S+1,M_s+1,1,-1\middle|SM_s\right)^2\left\{\left|\left\langle S\left|\hat{\mathcal{L}}_x\right|S+1\right\rangle\right|^2+\left|\left\langle S\left|\hat{\mathcal{L}}_y\right|S+1\right\rangle\right|^2\right\} \tag{12}$$

By using the properties of Clebsch-Gordan coefficients:

$$\left(S+1,M_s,1,0\middle|SM_s\right)=(-1)^{S+1-1+M_s}\sqrt{2S+1}\begin{pmatrix}S+1 & 1 & S\\ M_s & 0 & -M_s\end{pmatrix}=(-1)^{S+M_s}\sqrt{2S+1}\begin{pmatrix}S & S+1 & 1\\ -M_s & M_s & 0\end{pmatrix}=$$
$$(-1)^{S+M_s}\sqrt{2S+1}(-1)^{S+M_s-1}\sqrt{\frac{(S+M_s+1)(S-M_s+1)}{(S+1)(2S+1)(2S+3)}}=-\sqrt{\frac{(S+M_s+1)(S-M_s+1)}{(S+1)(2S+3)}} \tag{13}$$

and

$$\left(S+1,M_s+1,1,-1\middle|SM_s\right)=(-1)^{S+1-1+M_s}\sqrt{2S+1}\begin{pmatrix}S+1 & 1 & S\\ M_s+1 & -1 & -M_s\end{pmatrix}=$$
$$(-1)^{S+M_s}\sqrt{2S+1}(-1)^{2S+2}\begin{pmatrix}S+1 & 1 & S\\ -M_s-1 & 1 & M_s\end{pmatrix}=(-1)^{S+M_s}\sqrt{2S+1}(-1)^{2S}\begin{pmatrix}S & S+1 & 1\\ M_s & -M_s-1 & 1\end{pmatrix}=$$
$$(-1)^{S+M_s}\sqrt{2S+1}(-1)^{2S}(-1)^{S-M_s}\sqrt{\frac{(S+M_s+1)(S+M_s+2)}{(2S+1)(2S+2)(2S+3)}}=\sqrt{\frac{(S+M_s+1)(S+M_s+2)}{(2S+2)(2S+3)}} \tag{14}$$

Summing the Clebsch-Gordan coefficients one obtains:

$$\sum_{M_s=-S}^{S}\left(S+1,M_s,1,0\middle|SM_s\right)^2=\sum_{M_s=-S}^{S}\frac{(S+M_s+1)(S+1-M_s)}{(S+1)(2S+3)}=\frac{1}{(S+1)(2S+3)}\sum_{M_s=-S}^{S}(S+1)^2-M_s^2=$$
$$\frac{1}{(2S+2)(2S+3)}\left[(S+1)^2(2S+1)-2\frac{S(S+1)(2S+1)}{6}\right]=\frac{S(2S+1)(S+1)(2S+3)}{3(S+1)(2S+3)}=\frac{2S+1}{3} \tag{15}$$

and

$$\sum_{M_s=-S}^{S}\left(S+1,M_s+1,1,-1|SM_s\right)^2=\sum_{M_s=-S}^{S}\frac{(S+M_s+1)(S+M_s+2)}{(2S+2)(2S+3)}=$$
$$\frac{1}{(2S+2)(2S+3)}\sum_{M_s=-S}^{S}\left(S^2+3S+2+M_s^2\right)=$$
$$\frac{1}{(2S+2)(2S+3)}\left[(S^2+3S+2)(2S+1)+2\frac{S(S+1)(2S+1)}{6}\right]= \tag{16}$$
$$\frac{1}{(2S+2)(2S+3)}(S+1)(2S+1)\left[S+2+\frac{S}{3}\right]=\frac{(S+1)(2S+1)(4S+6)}{(2S+2)(2S+3)3}=\frac{2S+1}{3}$$

combining Equations (11), (15) and (16) one gets:

$$C_{S,S+1}=\frac{2S+1}{3}\left|\left\langle S\left|\hat{\mathcal{L}}_z\right|S+1\right\rangle\right|^2+\frac{2S+1}{3}\left\{\left|\left\langle S\left|\hat{\mathcal{L}}_x\right|S+1\right\rangle\right|^2+\left|\left\langle S\left|\hat{\mathcal{L}}_y\right|S+1\right\rangle\right|^2\right\}=$$
$$\frac{2S+1}{3}\left\{\left|\left\langle S\left|\hat{\mathcal{L}}_x\right|S+1\right\rangle\right|^2+\left|\left\langle S\left|\hat{\mathcal{L}}_y\right|S+1\right\rangle\right|^2+\left|\left\langle S\left|\hat{\mathcal{L}}_z\right|S+1\right\rangle\right|^2\right\}\equiv\frac{2S+1}{3}\left|\left\langle S\left|\hat{\mathcal{L}}\right|S+1\right\rangle\right|^2 \tag{17}$$

So in general the spin-orbit coupling constant is $\frac{2S+1}{3}$ times the square of the matrix element of L. The degeneracy of the diabatic states is (2S+1) thus the normalised constant is what should be used for the Landau-Zener probability:

$$H_{so}(S,S')=\frac{C_{S,S'}}{2\min(S,S')+1}=\frac{\left|\left\langle S\left|\hat{\mathcal{L}}\right|S'\right\rangle\right|^2}{3} \tag{18}$$

This is the averaged matrix element that can be used to get the probability of crossing or other dynamics simulations.

References

[1] D. Yarkony, Int. Rev in Phys. Chem. **11**, 195 (1992).

[2] S. Yabushita, THEOCHEM, **461-462**, 523-532 (1999).

[3] H.Nakamura, J. Chem. Phys. **87**, 4031(1987).

[4] D.M.Brink and G.R.Satchler Angular Momentum (Charedon Press,Oxford,1968).

CHAPTER VI. AN EXPERIMENTAL AND THEORETICAL STUDY OF THE SPIN-ORBIT INTERACTION FOR $CO^+(A^2\Pi_{3/2,1/2}, V^+=0\text{-}41)$ AND O_2^+ $(X^2\Pi_{3/2,1/2G}, V^+=0\text{-}38)$

A paper accepted to *J. Chem. Phys.*

D. G. Fedorov, M. Evans, Y. Song, M. S. Gordon, and C. Y. Ng

Abstract

Accurate spin-orbit splitting constants (A_{v+}) for the vibrational levels $v^+=0\text{-}41$ of $CO^+(A^2\Pi_{3/2,1/2})$ have been determined in a rotationally resolved pulsed field ionization photoelectron study. A change in slope is observed in the v^+ dependence for A_{v+} at $v^+\approx19\text{-}20$. This observation is attributed to perturbation of the $CO^+(A^2\Pi)$ potential by the $CO^+(B^2\Sigma^+)$ state. Theoretical A_{v+} values for $CO^+(A^2\Pi_{3/2,1/2}, v^+=0\text{-}41)$ have also been obtained using a newly developed *ab initio* computational routine for spin-orbit coupling calculations. The theoretical A_{v+} predictions computed using this routine are found to be in agreement with the experimental A_{v+} values $CO^+(A^2\Pi_{3/2,1/2}, v^+=0\text{-}41)$. Similar A_{v+} calculations obtained for $O_2^+(X^2\Pi_{3/2,1/2g}, v^+=0\text{-}38)$ are also in accord with the recent experimental A_{v+} values reported by Song et al. (*J. Chem. Phys.*, in press). The theoretical predictions are generally lower than the experimental results for both the $CO^+(A^2\Pi_{3/2,1/2})$ and $O_2^+(X^2\Pi_{3/2,1/2g})$ systems.

1. Introduction

The spin-orbit constants (A_{v+}) for the v^+=0 and 2 vibrational levels of $CO^+(A^2\Pi_{3/2,1/2})$ have been determined to be 122.03 and 121.87 cm^{-1}, respectively,[1,2] which are higher than the value of 117.5 cm^{-1} cited in Huber and Herzberg[3] based on earlier measurements. To our knowledge, the A_{v+} values for the high v^+-levels of $CO^+(A^2\Pi_{3/2,1/2}, v^+)$ have not been measured.

The most general experimental method for the determination of A_{v+} values of cations for a wide range of v^+ levels is the photoelectron spectroscopic technique. Due to autoionization mechanisms, photoelectron spectroscopic measurements often allow the observation of highly vibrationally excited states for the cation.[4,5] This is especially the case for threshold photoelectron or pulsed field ionization photoelectron (PFI-PE) measurements using a tunable ionization source,[5] where highly vibrationally excited ionic states can be observed due to finite couplings to nearby resonance Rydberg states and/or repulsive states. In photoionization studies using a fixed energy light source, such as HeI, highly vibrationally excited ionic states with negligible Franck-Condon factors can also be observed.[4] When the HeI photon energy coincides with the excitation energy of a Rydberg level, the Rydberg level initially formed can decay to a lower vibronic state of the cation, concomitant with the ejection of an energetic electron. This two-step mechanism can thus give rise to a long progression of vibrational bands for the cation, which would not be observed via direct ionization. The HeI spectrum for CO obtained by Wannberg et al.[4] indeed reveals high vibrational bands up to v^+=18 for $CO^+(A^2\Pi)$. However, the two spin-orbit states cannot be resolved in the latter experiment due to the relatively small spin-orbit splitting constant (A_{v+}) for $CO^+(A^2\Pi_{3/2,1/2})$. Kong *et al.*[6] have recently performed a high-resolution vacuum ultraviolet (VUV) laser PFI-PE study of $CO^+(A^2\Pi_{3/2,1/2}, v^+=0$ and 1). The observed rotationally resolved PFI-PE spectra for these vibrational bands are found to be

consistent with A_{v+} =120 cm^{-1} for v^+=0 and 1, which is close to the value of 122 cm^{-1} determined previously.[1,2]

Taking advantage of the high-resolution vacuum ultraviolet (VUV) facility of the Chemical Dynamics Beamline established at the Advanced Light Source (ALS),[7,8] we have recently developed a novel synchrotron based PFI-PE detection scheme,[9,10] achieving PFI-PE resolutions similar to that observed in VUV laser PFI-PE studies.[10-12] The ease of tunability over a wide energy range (6-30 eV) has made this synchrotron based PFI-PE method highly productive, particularly in measuring photoelectron bands of a long vibrational progression. In recent studies, we have reported rotationally resolved PFI-PE bands for long progressions of $O_2^+(X^2\Pi_{3/2,1/2g}, v^+=0\text{-}38)$,[13] $NO^+(X^1\Sigma^+, v^+=0\text{-}32)$[14], and $CO^+(X^2\Sigma^+, v^+=0\text{-}42)$.[15] Using the same experimental method, we have obtained rotationally resolved PFI-PE spectra for $CO^+(A^2\Pi_{3/2,1/2}, v^+=0\text{-}41)$. The intensities of PFI-PE bands for higher v^+ (>10) levels of $CO^+(A^2\Pi_{3/2,1/2})$ are more than 100 fold lower than those observed for the v^+=0-2 bands. Despite the low intensities for the high v^+ bands, we have successfully recorded most of the PFI-PE bands for $CO^+(A^2\Pi_{3/2,1/2}, v^+=0\text{-}41)$ at the rotationally resolved level with good signal-to-noise ratios. Here, we present accurate A_{v+} values for $CO^+(A^2\Pi_{3/2,1/2}, v^+=0\text{-}41)$ derived from the analysis of the rotationally-resolved PFI-PE spectrum of CO.

In the theoretical front, reliable calculations on spin-orbit interactions have not been readily accessible due to the requirement of accurate electronic and vibrational wavefunctions. Many theoretical calculations[16-19] have been made on the potential energy surfaces of CO^+. The recent multi-configuration self-consistent field configuration interaction (MCSCF-CI) calculations of Lavendy and Robbe[16] and Okada and Iwata[17] have obtained reliable predictions for the vibrational and rotational constants of $CO+(A^2\Pi_{3/2,1/2})$.

However, the A_{v+} value of 92 cm^{-1} for $CO+(A^2\Pi_{3/2,1/2})$ calculated by Lavendy and Robbe[16] is significantly smaller than the experimental measurements[1,2] of 122 cm^{-1}.

In view of the lack of computational routines available for reliable calculations of spin-orbit coupling constants, we have recently developed a new *ab initio* computational code for this purpose. This code, to be included into the production version of the publicly available quantum chemistry package GAMESS,[20] has the capability of performing efficient spin-orbit coupling calculations for arbitrary spin multiplicities with any CI wavefunction types supported by GAMESS, for both one and two electron spin-orbit coupling operators. As a test of this computational code, we have calculated the A_{v+} values for $CO+(A^2\Pi_{3/2,1/2}, v^+=0\text{-}41)$ for comparison with the experimental measurements.

Highly accurate spin-orbit coupling constants for $O_2^+(X^2\Pi_{1/2,3/2g}, v^+\leq 11)$ have been determined previously[21] in a comprehensive analysis of the $O_2^+(A^2\Pi_u) \rightarrow O_2^+(X^2\Pi_g)$ emission system. The VUV laser PFI-PE study of Kong and Hepburn has extended the measurement to $O_2^+(X^2\Pi_{1/2,3/2g}, v^+ =24)$.[22] By employing the synchrotron based PFI-PE detection method, Song *et al.*. have made a comprehensive spectroscopic study on $O_2^+(X^2\Pi_{1/2,3/2g}, v^+ =\text{-}0\text{-}38)$,[13] which provides reliable A_{v+} values for these states. Thus, the experimental A_{v+} values for $O_2^+(X^2\Pi_{1/2,3/2g})$ can be considered well established. For this reason, we have also obtained theoretical A_{v+} values for this system. The comparison of the theoretical values with experimental A_{v+} data for the $O_2^+(X^2\Pi_{1/2,3/2g})$ system serves as a second test case for the new computational code.

2. Experimental and theoretical methods

a) High-resolution PFI-PE measurements

The design and performance of the Chemical Dynamics Beamline at the ALS has been described previously.[7-11] Briefly, the major components for the high-resolution VUV photoionization facility at this beamline include a 10 cm period undulator (U10), a gas harmonic filter,[23] a 6.65-m off-plane Eagle mounted monochromator,[8] and a photoelectron-photoion apparatus.[9-11]

In the present experiment, helium was used in the gas harmonic filter, where higher undulator harmonics with photon energies greater than 24.59 eV were suppressed. The fundamental light from the undulator was then directed into the 6.65-m monochromator and dispersed by a 4800 l/mm grating (dispersion = 0.32 Å/mm) before entering the experimental apparatus. The ALS storage ring is capable of filling 328 electron buckets in a period of 656 ns. Each electron bucket emits a light pulse of 50 ps with a time separation of 2 ns between successive bunches. In each storage ring period, a dark gap (80 ns) consisting of 40 consecutive unfilled buckets exists for the ejection of cations from the orbit. Thus, the present experiment was performed in the multibunch mode with 288 bunches in the synchrotron orbit, corresponding to a repetition rate of 439 MHz.

The multi-purpose photoelectron-photoion apparatus associated with the Chemical Dynamics Beamline was used for the present study.[9-11] A continuous effusive CO beam was produced by a metal orifice (diameter = 0.5 mm) at 298 K and a distance of 0.5 cm from the photoionization/photoexcitation (PI/PEX) region. Thus, the rotational temperature of the CO sample is expected to be ≈298 K. We estimate that the CO density at the PI/PEX region is $\approx 10^{-3}$ Torr. The photoionization chamber and photoelectron chamber were evacuated by

turbomolecular pumps with pumping speeds of 1200 L/s and 3400 L/s, respectively. The respective pressures maintained in the photoionization chamber and the photoelectron chamber were $\approx 1 \times 10^{-5}$ and $\approx 1 \times 10^{-7}$ Torr during the experiment.

The PFI-PE detection scheme using the high-resolution monochromatized undulator synchrotron radiation facility at the ALS has been described previously.[9-11] Briefly, a pulsed electric field (height = 1.1 V/cm, width = 40 ns, delayed by 20 ns with respect to the beginning of the 80 ns synchrotron dark gap) was applied to the repeller at the PI/PEX region. This pulsed electric field was used to field ionize high-*n* Rydberg species and extract photoelectrons toward the detector and was applied every synchrotron ring period (0.656 μs). An electron spectrometer, which consists of a steradiancy analyzer and a hemispherical energy analyzer arranged in tandem, was used to filter prompt electrons. We have previously shown that PFI-PEs can be detected with little background from prompt electrons after only an 8 ns delay with respect to the beginning of the dark gap.

The achievable PFI-PE resolution depends on the resolution of the excitation VUV light source and the magnitude of the applied pulsed electric field.[10] The PFI-PE spectra for CO presented in this experiment were measured using monochromator slits ranging from 30-200 μm. The PFI-PE resolution achieved was 4-7 cm^{-1} (FWHM). The photon energy step size and counting time used at each photon energy varied between 0.1-0.3 meV and 3-30 sec, respectively.

The PFI-PE spectra for CO were calibrated using the PFI-PE spectra of the $Ar^+(^2P_{3/2})$ and $Ne^+(^2P_{3/2})$ bands obtained at the same experimental conditions. This calibration scheme assumes that the Stark shifts for the IEs of CO and the rare gases are identical. The calibration for the CO PFI-PE spectrum was made before and after the experiment. Our previous experience with energy calibrations of the PFI-PE spectra of other molecular systems indicates that the accuracy of the present energy calibration is within ±0.5 meV.[24]

Since the spin-orbit PFI-PE components for individual v^+-levels were recorded in a single scan, the error due to energy calibration does not apply to the uncertainties assigned for the A_{v+} values. Most of the A_{v+} values reported here are based on rotationally resolved data and have uncertainties well within ± 2 cm^{-1}.

b) Spin-orbit coupling calculations

Ab initio spin-orbit coupling calculations have been made possible by generalization of the existing spin-orbit coupling code built into the quantum chemistry package GAMESS.[20] In order to accurately reproduce experimental results, a large basis set (AVTZ, built into MOLPRO)[25-29] and an extensive CI wavefunction have been used. The orbitals are optimized with the complete active space self-consistent field (CASSCF) method, the active space including 12 electrons in 8 orbitals (2s and 2p on C and O).[Ref. 30] Energy values are further refined with single and double excitations from the CASSCF active space into the virtual space using MOLPRO. We have examined the effect of adding single and double excitations from the core 1s orbitals into the virtual space: the CO^+ results do not include such excitations and the O_2^+ results do. Spin-orbit coupling calculations are performed with the CASSCF wavefunction and Pauli-Breit Hamiltonian,[31] including rigorous one and two-electron terms and using the modified version of GAMESS soon to be released for distribution. The effect of including neighboring states into spin-prbit coupling diagonalization has been studied. CO^+ calculations include the 6 lowest CI roots and O_2^+ calculations include two roots (i.e., only the $^2\Pi_u$ state).

The potential energy of $CO^+(A^2\Pi)$ has been calculated for a series of internuclear C-O distances (R) of interest and a geometry optimization has been performed (at the CASSCF

level) to locate the potential minimum. Experimentally, the splitting between the $CO^+(A^2\Pi_{3/2})$ and $CO^+(A^2\Pi_{1/2})$ spin-orbit states is found as a function of vibrational quantum number up to v^+=41. The rotational constants (B_v^+) for $CO^+(A^2\Pi_{3/2,1/2}, v^+=0\text{-}41)$ have also been determined. In the first approach, the corresponding average R value $\langle r_{v+} \rangle$ for individual v^+-levels of $CO^+(A^2\Pi)$ is estimated using the harmonic oscillator approximation,

$$\langle r_{v+} \rangle = \frac{\hbar}{\sqrt{2\mu B_{v+}}}, \tag{1}$$

where B_v is the rotational constant given by the experiment and μ is the reduced mass of CO^+. At each $\langle r_{v+} \rangle$ value, the spin-orbit coupling constant is computed (the single-point approach). As shown in the discussion below, the A_{v+} constants for $CO^+(^2\Pi_{3/2})$ and $CO^+(^2\Pi_{1/2})$ calculated at these $\langle r_{v+} \rangle$ distances deviate significantly from the experimental values, especially for high v^+ levels.

A more sophisticated approach involves the least square fit of the calculated *ab initio* potenital energies at a series of R values to a Morse potential,

$$U(R) = D_e\{1 - \exp[-a(R - R_e)]\}^2, \tag{2}$$

where D_e is the well-depth and R_e is the internuclear distance at the potential minimum. The best fitted parameters D_e and a obtained for the Morse potential are listed in Table I. The corresponding vibrational frequency (ω_e) and anharmonicity constant ($\omega_e\chi_e$) for the Morse potential, together with the *ab initio* R_e value for $CO^+(A^2\Pi_{3/2,1/2}, v^+=0)$, are also included in Table I. We note that for a Morse potential only two out of the four parameters (D_e, a, ω_e,

$\omega_e\chi_e$) are independent. Since accurate vibrational energies for the $CO^+(A^2\Pi_{3/2,1/2}, v^+=0\text{-}41)$ states have also been determined based on the simulation of their PFI-PE bands, we have also constructed a Morse potential to provide the best fit for the experiment vibrational energies of $CO^+(A^2\Pi_{3/2,1/2})$. The best fitted parameters for the experimental $CO^+(A^2\Pi_{3/2})$ and $CO^+(A^2\Pi_{1/2})$ Morse potentials are also given in Table I. We find that these Morse potentials obtained based on the experimental vibrational energies for $CO^+(A^2\Pi_{3/2,1/2})$ are in reasonable agreement with the $CO^+(A^2\Pi)$ Morse potential based on the *ab initio* calculation. We note that the R_e value and the width of the theoretical $CO^+(A^2\Pi)$ Morse potential are greater than the experimental $CO^+(A^2\Pi_{3/2,1/2})$ Morse potentials. As a result, the outer turning point of the theoretical Morse potential is greater than that of the experimental Morse potential at the same energy. We also list the Morse potential parameters for $CO^+(A^2\Pi)$ constructed based on the vibrational constants cited in Huber and Herzberg.[3] These parameters are in accord with those deduced from the present experiment.

The vibronic wavefunction used is,

$$\Psi^v(r,R) = \Psi_N^v(R)\Psi_e(r,R), \tag{3}$$

where $\Psi_N^v(R)$ is an eigenfunction of the theoretical Morse potential, $\Psi_e(r,R)$ is the electronic wavefunction. R and r are the nuclear and electron coordinates, respectively. The theoretical A_{v+} value is calculated as,

$$A_v = \frac{\iint\left[\Psi_N^v(R)\right]^+\left[\Psi_e(r,R)^+\hat{H}_{PB}\Psi_e(r,R) - \Psi_e'(r,R)^+\hat{H}_{PB}\Psi_e'(r,R)\right]\Psi_N^v(R)drdR}{\int\left[\Psi_N^v(R)\right]^+A(R)\Psi_N^v(R)dR}, \tag{4}$$

where $\hat{H}_{PB}$ is the Pauli-Breit Hamiltonian.[31] $\Psi_e(r,R)$ and $\Psi'_e(r,R)$ are the eigenvectors of the H_{PB} matrix in the basis of CASSCF states. The unprimed and primed states correspond to the two levels between which the splitting is calculated (i.e., between J=1/2 and J=3/2 levels). A*b initio* splitting constants as a function of R, A(R), are first calculated at discrete R values and then fitted to an appropriate analytical form for the convenience of performing numerical integration. For the $CO^+(A^2\Pi_{3/2,1/2})$ system, the A(R) function is found to have the form $A(R) = h(1 - \tanh[(R - R_o)s]) + A_0$ with the following least square fit parameters: h = 51.25, A_0 = 13.5, R_o = 2.02, s = 3.75. Here, R and A(R) are in Å and cm^{-1}, respectively.

The average vibrational energies for the $O_2^+(X^2\Pi_{3/2,1/2g})$ spin-orbit states have been determined recently in a similar PFI-PE experiment by Song *et al.*[13] The Morse potentials based on fitting to these experimental vibrational energies are given in Table I for comparison with the best fitted *ab initio* Morse potential for $O_2^+(X^2\Pi)$. As a reference, we also include in Table I the Morse potential for $O_2^+(X^2\Pi)$ based on the vibrational constants cited in Huber and Herzberg.[3] Similar to the observation for the $CO^+(A^2\Pi)$ system, the theoretical R_e value is larger than that determined in the experiment. As a result, the outer wall of the theoretical Morse potential for $O_2^+(X^2\Pi)$ is wider than that for the experimental Morse potential.

The A(R) function associated with Eq. (4) of the $O_2^+(X^2\Pi)$ system has the functional form: $A(R) = h \exp[-s(R - R_o)^2] + A_0$. The least square fit parameters are, h = 138.219, A_0 = 1.06641, R_o = 1.0115, and s = 58.9876.

3. Results and discussion

a) $CO^+(A^2\Pi_{3/2,1/2}, v^+=0\text{-}41)$

We have obtained rotationally resolved PFI-PE bands for $CO^+(A^2\Pi_{3/2,1/2}, v^+=0\text{-}41)$. The bulk of these data and their analysis, including important issues on spectroscopy and photoionization dynamics, will be presented in a future publication.[32] Here, we have selected to show in Figs. 1(a), 1(b), and 2(b) the respective experimental PFI-PE bands (solid circles) for $CO^+(A^2\Pi_{3/2,1/2}, v^+=2, 15, 38)$ to illustrate of the assignment for the spin-orbit components and the typical quality of the simulation. As with the rotational and vibrational constants, the A_{v+} values for $CO^+(A^2\Pi_{3/2,1/2}, v^+=0\text{-}41)$ are derived from the spectral simulation. The intensities shown for the spectra of Figs. 1(a), 1(b), and 2 reflect the actual relative intensities. As shown in these figures, the intensities for the $CO^+(A^2\Pi_{3/2,1/2}, v^+=15$ and 38) bands are more than two orders of magnitude lower that for the $CO^+(A^2\Pi_{3/2,1/2}, v^+=2)$ band. We note that the PFI-PE band for $CO^+(A^2\Pi_{3/2,1/2}, v^+=38)$ has partial overlap with the $CO^+(X^2\Sigma^+, v^+=37)$. Thus, Fig. 2 is a composite figure with panel (a) showing the comparison of the experimental (solid circles) and simulated (solid line) spectra for $CO^+(X^2\Sigma^+, v^+=37)$. The analysis and simulation of the PFI-PE bands for $CO^+(X^2\Sigma^+, v^+=0\text{-}42)$ has been reported previously and thus will not be substantiated here.[13]

The relative intensities for rotational structures resolved in a vibrational band were simulated using the Buckingham-Orr-Sichel (BOS) model,[33] which is described by the formula,

$$\sigma(J^+\leftarrow N'') \propto \Sigma_\lambda\ Q(\lambda;J^+,N'')C_\lambda, \qquad (5)$$

This model was derived to predict rotational line strengths observed in the single-photon ionization of diatomic molecules. Since the BOS model does not take into account channel interactions, which are certain to occur in the PFI-PE spectra, we may consider the BOS simulation used here as semi-empirical in nature. As in previous studies, the BOS simulation is valid in determining spectroscopic constants from the experimental PFI-PE spectra. The factor C_λ is associated with the electronic transition moments, which is the linear combination of electron transition amplitudes for the possible angular momenta ℓ of the ejected electron. The other factor Q is determined by the angular momentum coupling scheme. The parameter λ can be interpreted as the partial wave of the electron in the ground state of the neutral molecule. The more general interpretation of λ is that of the angular momentum transfer in the photoionization process. The angular momentum coupling factor Q for the photoionization of the present CO system can be described by a Hund's case (b) to (a) transition. The Q factor is thus expressed as,

$$Q(\lambda; J^+, N'') = \frac{2J^+ + 1}{2S^+ + 1} \sum_{\chi=|\lambda-1/2|}^{\chi=\lambda+1/2} (2\chi+1) \begin{pmatrix} \lambda & S^+ & \chi \\ \Delta\Lambda & \Sigma^+ & \Lambda''-\Omega^+ \end{pmatrix}^2 \begin{pmatrix} J^+ & \chi & N'' \\ -\Omega^+ & \Omega^+ - \Lambda'' & \Lambda'' \end{pmatrix}^2, \qquad (6)$$

where $\Delta\Lambda = \Lambda^+ - \Lambda'$ and $\Omega^+ = |\Lambda \pm \Sigma|$. Here, Λ^+ and Σ^+ are the projection of the electron orbital angular momentum and electron spin angular momentum on the axis of CO^+, respectively, and Λ'' is the projection of the electron orbital angular momentum on the axis of CO. Given that $\Delta\Lambda = 1$ for the transition $CO^+(A^2\Pi_\Omega, v^+) \leftarrow CO(X^1\Sigma^+, v'' = 0)$, the first 3-j symbol of Eq. (6) requires that $\lambda \geq 1$. The contribution by each C_λ was determined from the fit to the experimental data. Each spin-orbit state was simulated using a unique set of C_λ's.

The rotational structure observed in the experiment was accounted for using the BOS coefficients (C_1, C_2, C_3, and C_4). Thus, the possible angular momentum states for the ejected photoelectron were l = 0, 1, 2, 3, 4, and 5. The possible change in total angular momentum for a Hund's case (b) to (a) ionization transition is given by[12]

$$\Delta J = J^+ - J'' = l + 3/2, l + 1/2, \ldots, -l - 3/2. \quad (7)$$

Rotational transitions ($\Delta N = N^+ - N''$) of -4, -3, -2, -1, 0, 1, 2, 3, and 4 (designated as M, N, O, P, Q, R, S, T, and U branches, respectively) are clearly observed in the spectra, although transitions up to $\Delta N = \pm 6$ are possible according to Eq. (7).

We assume that the rotational population for CO was characterized by a Boltzmann distribution with a rotational temperature of 298 K. The simulation uses known spectroscopic constants for the molecular ground state $CO(X^1\Sigma^+, v^+)$: $\omega_e'' = 2169.81358\ cm^{-1}$, $\omega_e\chi_e'' = 13.28831 cm^{-1}$, $B_e'' = 1.93128\ cm^{-1}$, and $\alpha_e'' = 0.017504\ cm^{-1}$.[3] The spin-rotational splitting present in the ionic state has been ignored since it is much smaller than the experimental PFI-PE resolution.

In addition to the BOS C_λ coefficients, the rotational constant B_v^+ and the spin-orbit coupling constant A_{v+} were varied during the simulation of each vibration level. The simulated spectra (solid line, lower spectra) shown in Figs. 1(a), 1(b), and 2(b) were obtained using a Gaussian profile with a linewidth of 4, 4, and 7 cm^{-1} (FWHM), respectively. The positions of the rotational transitions $CO^+(A^2\Pi_{3/2}, v^+, N^+) \leftarrow CO(X^1\Sigma^+, v''=0, N'')$ and $CO^+(A^2\Pi_{1/2}, v^+, N^+) \leftarrow CO(X^1\Sigma^+, v'' = 0, N'')$ are shown by respectively downward pointing and upward pointing stick marks in Figs. 1(a), 1(b), and 2(b). As shown in Figs. 1(a) and 1(b), the agreement between the BOS simulated spectra and the experiment PFI-PE spectra

are excellent, yielding values of 120.2±2.0 cm^{-1} for $A_{v+}(v^+=2)$, and 117±2.0 cm^{-1} for $A_{v+}(v^+=15)$. The $A_{v+}(v^+=2)$ value is in excellent accord with the literature value of 121.87 cm^{-1}.[2] The comparison of the BOS simulated (solid line) and experimental (solid circles) PFI-PE band for $CO^+(A^2\Pi_{1/2}, v^+=38)$ is shown in Fig. 2(b). The sum of the simulated spectra for $CO^+(X^2\Sigma^+, v^+=37)$ shown in Fig. 2(a) and $CO^+(A^2\Pi_{1/2}, v^+=38)$ gives the overall simulated spectrum (solid line) in Fig. 2(c), which is again in excellent accord with the experimental PFI-PE spectrum (solid circles). The A_{v+} value for $CO^+(A^2\Pi_{3/2,1/2}, v^+=38)$ is determined to be 66.1±3.0 cm^{-1}.

The A_{v+} values for $CO^+(A^2\Pi_{1/2}, v^+=0\text{-}41)$ obtained in the BOS simulation are listed in Table II. The plot of the experimental A_{v+} value versus v^+ is shown in Fig. 3. It is interesting to note that the A_{v+} value seems to remain nearly constant until $v^+\approx19$, which has an IE value of 19.6 eV. Then it decreases nearly linearly toward higher v^+. Although the A_{v+} values for $CO^+(A^2\Pi_{3/2,1/2}, v^+=20$, 21, and 23) were not determined in the present experiment due to serious overlap with the $CO^+(A^2\Pi-X^2\Sigma^+)$ bands, the plot of Fig. 3 seems to reveal a break or a change in slope at $v^+\approx19\text{-}20$. This may be indicative of perturbation by other states.

Figure 4 depicts the PFI-PE spectrum for CO in the region of 18.5-20.7 eV. The positions of v^+ levels for $CO^+(X^2\Sigma^+, A^2\Pi_{3/2,1/2}, B^2\Sigma^+)$ are marked in the figure. We note the overlap of the weak $CO^+(A^2\Pi_{3/2,1/2}, v^+=19$ and 20) PFI-PE bands with the overwhelmingly strong vibrational band for $CO^+(B^2\Sigma^+, v^+=0)$ at 19.80 eV. This observation suggests that the break observed for the v^+ dependence of A_{v+} may arise from high order interactions between the $CO^+(A^2\Pi, v^+=19$ and 20) and $CO^+(B^2\Sigma^+, v^+=0)$ states. By symmetry, the $CO^+(A^2\Pi)$ and $CO^+(B^2\Sigma^+)$ can mix by spin-orbit interaction.

Included in Table II are the theoretical A_{v+} values obtained based on the theoretical Morse potential and the single-point approach. We have also plotted in Fig. 4 these theoretical A_{v+} values. As shown in Fig. 4, for $v^+ \leq 19$ the single-point theoretical predictions and the experimental results are in slightly better accord than those obtained based on the theoretical Morse potential. However, the predictions for $v^+ > 19$ obtained by the single-point approach deviate significantly lower from the experimental values. This discrepancy observed at high v^+ is expected and can be attributed to the increasing anharmonicity of the $CO^+(A^2\Pi)$ potential at high v^+. That is, the $\langle r_e \rangle$ values calculated using the approximation of Eq. (1) are not valid at high v^+ levels, yielding significantly smaller values than the actual equilibrium bond distances for high v^+ levels. The theoretical predictions obtained using the theoretical Morse potential show the correct overall v^+ dependence for A_{v+}. The theoretical A_{v+} value varies smoothly over the whole v^+ range. Contrary to the experimental observation, the v^+ dependence for the theoretical A_{v+} values shows no break at $v^+ \approx 19$-20.

We find that all theoretical A_{v+} values obtained based on the theoretical Morse potential are slightly lower than the corresponding experimental values. Upon comparing the theoretical and experimental Morse potentials, we find that the *ab initio* R_e value is larger than the experiment R_e value. Furthermore, the outer wall of the *ab initio* Morse potential is softer than that of the experimental Morse potential. That is, at the same energy, the outer turning point for the *ab initio* Morse potential lies at a larger R than that for the experimental Morse potential. As a result, the theoretical Morse potential predicts a larger value for the average equilibrium distance for a given v^+ than that of the experimental Morse potential. This analysis indicates that the lower theoretical predictions compared to the experimental results can be partly ascribed to finite inaccuracy of the *ab initio* Morse potential.

b) $O_2^+(X^2\Pi_{3/2,1/2g}, v^+=0\text{-}38)$

The theoretical A_{v+} predictions obtained here based on the single-point approach and the *ab initio* Morse potential arc listed in Table I for comparison with the experimental A_{v+} values for $O_2^+(X^2\Pi_{3/2,1/2g}, v^+=0\text{-}38)$. The latter values have been reported recently by Song *et al.*[13] Similar to the comparison of the $CO^+(A^2\Pi)$ system, the single-point predictions are slightly closer to the experimental results at low v^+ (<19). However, contrary to the experimental observation, the slope for the single-point A_{v+} prediction versus v+ plot remains nearly constant over the entire range of v^+=0-38. That is, the single-point predictions are significantly higher than the corresponding experimental values at higher v^+ (>21) levels. This observation can also be attributed to the inaccuracy of using Eq. (1) for the prediction of $\langle r_e \rangle$ values at high v^+-levels.

The trend of the v^+ dependence for the theoretical A_{v+} value obtained using the *ab initio* Morse potential is consistent with the experimental data. Although the theoretical predictions based on the *ab initio* Morse potential and experimental A_{v+} values are in general agreement, all theoretical predictions are slightly lower than the corresponding experimental results. The comparison of the *ab initio* and experimental Morse potentials are similar to the situation of the $CO^+(A^2\Pi)$ system. That is, the outer wall of the theoretical Morse potential is shifted to the longer range compared to that of the experimental Morse potential. Thus, this partly contributes to the lower calculated A_{v+} values.

The A_{v+} values for $O_2^+(X^2\Pi_{3/2,1/2g}, v^+=20)$ determined in both the synchrotron based PFI-PE[13] and VUV laser[22] PFI-PE studies are higher than the A_{v+} values for the adjacent v^+=19 and 20 states. Thus, the variation of A_{v+} versus v^+ is most likely not a smooth function. We note this kink observed at $O_2^+(X^2\Pi_{3/2,1/2g}, v^+=20)$ with an IE ≈15.96 eV is also

close to the beginning of the vibrational progression of the $O_2^+(a^4\Pi_u)$ state beginning at ≈16.10 eV. The latter PFI-PE band is nearly in total overlap with the $O_2^+(X^2\Pi_{3/2,1/2g}, v^+=21)$ state. The A_{v+} values for $O_2^+(X^2\Pi_{3/2,1/2g}, v^+=37$ and 38), which have the IEs ≈17.9-18.0 eV, also seem to deviate from the general trend of the A_{v+} versus v^+ curve. This observation may be correlated to the appearance of the vibrational progression for the $O_2^+(b^4\Sigma_g^-)$ state at 18.1 eV. On the basis of this observation, we tentatively attribute this kink at $O_2^+(X^2\Pi_{3/2,1/2g}$, $v^+=20)$ and $O_2^+(X^2\Pi_{3/2,1/2g}, v^+=37$-38) as due to perturbation by the $O_2^+(a^4\Pi_u)$ and $O_2^+(b^4\Sigma_g^-)$ states, respectively. This speculation requires theoretical confirmations in the future.

The effect of core excitations is noticeable mostly at large distances near the dissociation limit where the core excitations become essential to obtain a good energy curve. The Morse potential parameters are noticeably better for O_2^+ where the excitations have been included. The inclusion of other low lying states (CO^+) , most noticeably, $X^2\Sigma^+$, gives an opportunity to theoretically verify the experimentally observed features in spin-orbit splitting. Since the Morse potential approach is based upon the single state results, it displays a smooth dependence without any jumps. The single point approach, on the other hand, allows one to study the effect of other states. The calculated jump in spin-orbit splitting at $v^+=24$ is due to interaction with the $X^2\Sigma^+$ state. To be consistent with the rest of calculations we choose to optimze orbitals only for the $A^2\Pi$ state and use these orbitals to obtain the wavefunction for the other state. This causes a somewhat overestimated jump in the splitting.

4. Conclusions

We have obtained accurate A_{v+} constants for $CO^+(A^2\Pi_{3/2,1/2}, v^+=0$-41) in a rotationally resolved PFI-PE experiment. A break at $CO^+(A^2\Pi_{3/2,1/2}, v^+\approx19$-20) was observed in the plot of

A_{v+} versus v^+. Such a feature is tentatively interpreted as due to perturbation of the $CO^+(B^2\Sigma^+)$ state. We have also identified similar features in the v^+ dependence of A_{v+} values for $O_2^+(X^2\Pi_{3/2,1/2g}, v^+=0\text{-}38)$, suggesting perturbation from the $O_2^+(A^2\Pi_u)$ and $O_2^+(b^4\Sigma^-_g)$ states.

We have also developed a new *ab initio* computational code for reliable spin-orbit coupling calculations. The A_{v+} predictions for $CO^+(A^2\Pi_{3/2,1/2}, v^+=0\text{-}41)$ and $O_2^+(X^2\Pi_{3/2,1/2g}, v^+=0\text{-}38)$ obtained using this computation routine are found to be in agreement with experimental meausrments.[13]

The systematic underestimation of the theoretical values for the splitting relative to the experimental values is attributed to two factors of the same order of importance: the first order perturbative treatment of spin-orbit coupling and the complete omission of the spin-spin coupling. To assessthe effect of a larger CI expansion upon the spin-orbit coupling we have performed spin-orbit coupling calculations with single excitations from the CAS into the virtual space at equilibrium, near the dissociation limit and at a middle point. The splitting decreased by about $4cm^{-1}$ except for the dissociation limit where the change was $8cm^{-1}$. Single and double excitations are several million in number and are not possible computationally unless some kind of contraction scheme is employed.

Acknowledgments

This work was supported by the Director, Office of Energy Research, Office of Basic Energy Sciences, Chemical Science Division of the U. S. Department of Energy under contract No. W-7405-Eng-82 for the Ames Laboratory, and Contract No. DE-AC03-76SF00098 for the Lawrence Berkeley National Laboratory. Y.S. is the recipient of the 1999 Wall Fellowship at Iowa State University.

References

1. Katayama et al, *J. Chem. Phys.* **75**, (1981).
2. Gagmaire et al, *Can. J. Phys.* **54**, 2111 (1976).
3. K. P. Huber and G. Herzberg, "Molecular Spectra and Molecular Structure, Vol. IV, Constants of Diatomic Molecules" (Van Nostrand, New York, 1979).
4. B. Wannberg, D. Nordfors, K. L. Tan, L. Karlsson, and L. Mattsson, *J. Elec. Spec. Relat. Phenom.*, **47**, 147 (1988).
5. P.-M. Guyon and T. Baer, in *High Resolution Laser Photoionization and Photoelectron Studies*, edited by I. Powis, T. Baer, and C. Y. Ng, Wiley Series in Ion Chemistry and Physics (Wiley, Chichester, 1995), Chap. 1.
6. Kong et al, *J. Phys. Chem.* **99**, 1637 (1995).
7. C.-W. Hsu, M. Evans, P. Heimann, K. T. Lu, and C. Y. Ng, *J. Chem. Phys.* **105**, 3950 (1996).
8. P. Heimann, M. Koike, C.-W. Hsu, M. Evans, K. T. Lu, C. Y. Ng, A. Suits, and Y. T. Lee, *Rev. Sci. Instrum.* **68**, 1945 (1997).
9. C.-W. Hsu, M. Evans. P. A. Heimann, and C. Y. Ng, *Rev. Sci. Instrum.*, **68**, 1694 (1997).
10. C.-W. Hsu, M. Evans, S. Stimson, C. Y. Ng, and P. Heimann, *Chem. Phys.* **231**, 121 (1998).
11. C. Y. Ng, in "Photoionization and Photodetachment", edited by C. Y. Ng, *Adv. Ser. Phys. Chem.* (World Scientific, Singapore, 1999), Vol. 10A, in press.
12. Powis, T. Baer, and C. Y. Ng, editors, "High Resolution Laser Photoionization and Photoelectron Studies", *Wiley Series in Ion Chem. and Phys.* (Wiley, Chichester, 1995).
13. Y. Song, M. Evans, C. Y. Ng, C.-W. Hsu, and G. K. Jarvis, *J. Chem. Phys.*, accepted.
14. G. K. Jarvis, M. Evans, C. Y. Ng, and K. Mitsuke, *J. Chem. Phys.*, accepted.
15. M. Evans and C. Y. Ng, *J. Chem. Phys.*, submitted.
16. H. Lavendy and J.M. Robbe, *Chem. Phys. Lett.*, **205**, 456 (1993).
17. K. Okada and S. Iwata, to be published.
18. N. Honjou and Sasaki, *Mol. Phys.* **37**, 1593 (1978).
19. M. E. Wacks, *J. Chem. Phys.* **41**, 930 (1964).
20. M. W. Schmidt, K. K. Baldridge, J. A. Boatz, S. T. Elbert, M. S. Gordon, J. H. Jensen, S. Koseki, N. Matsunaga, K. A. Nguyen, S. J. Su, T. L. Windus, M. Dupuis, J. A. Montgomery, J Comput. Chem. **14**, 1347 (1993).
21. J. A. Coxon and M. P. Haley, *J. Mol. Spectrosc.* **108**, 119 (1984).

22. W. Kong and J. W. Hepburn, *Can. J. Phys.* **72**, 1284 (1994).
23. A. G. Suits, P. Heimann, X. Yang, M. Evans, C.-W. Hsu, D. A. Blank, K.-T. Lu, A. Kung, and Y. T. Lee, *Rev. Sci. Instrum.*, **66**, 4841 (1995).
24. S. Stimson, Y.-J. Chen, M. Evans, C.-L. Liao, C. Y. Ng, C.-W. Hsu, and P. Heimann, *Chem. Phys. Lett.*, **289**, 507 (1998).
25. MOLPRO is a package of ab initio programs written by H.-J. Werner and P. J. Knowles, with contributions from J. Almlöf, R. D. Amos, M. J. O. Deegan, S. T. Elbert, C, Hampel, W. Meyer, K. Meyer, K. Peterson, R. Pitzer, A. J. Stone, P. R. Taylor, and R. Lindh.
26. H.-J. Werner and P. J. Knowles, *J. Chem. Phys.* **82**, 5053 (1985).
27. P. J. Knowles and H.-J. Werner, *Chem. Phys. Lett.* **115**, 259 (1985).
28. H.-J. Werner and P. J. Knowles, *J. Chem. Phys.* **89**, 5803 (1988).
29. P. J. Knowles and H.-J. Werner, *Chem. Phys. Lett.* **145**, 514 (1988).
30. M.W.Schmidt and M.S.Gordon, Ann. Rev. Phys. Chem.,**49**,233 (1998)
31. H. A. Bethe and E. E, Salpeter, "Quantum Mechanics of the One and Two Electron Atoms" (Plenum, New York, 1977).
32. M. Evans and C. Y. Ng, . *Chem. Phys.*, in preparation.
33. A. D. Buckingham, B. J. Orr, J. M. Sichel, *Phil. Trans. Roy. Soc. Lond. A* **268**, 147 (1970).

Table I. Parameters[a] for the Morse potential [Eq. (2)] for $CO^+(A^2\Pi)$ and $O_2^+(X^2\Pi)$ obtained by fitting the ab initio potential energies and experimental vibrational energies for $CO^+(A^2\Pi_{3/2})$.

Morse Potential	R_e (Å)	A ($Å^{-1}$)	D_e (cm^{-1})	ω_e^+ (cm^{-1})	$\omega_e^+\chi_e^+$ (cm^{-1})
Expt. $CO^+(A^2\Pi_{3/2})^b$	1.2444	2.3531	45147	1567.5	13.61
Expt. $CO^+(A^2\Pi_{1/2})^b$	1.2444	2.3579	45006	1568.3	13.66
Expt. $CO^+(A^2\Pi)^c$	1.2436	2.345	45115	1562.1	13.52
Theo $CO(A^2\Pi)^d$	1.2510	2.2585	45542	1511.1	12.53
Expt. $O_2^+(X^2\Pi)^e$	1.1200	2.8343	54392	1919.1	16.93
Expt. $O_2^+(X^2\Pi)^c$	1.1227	2.8008	53250	1876.4	16.53
Theo $O_2^+(X^2\Pi)^d$	1.1249	2.7915	55541	1910.0	16.42

a) R_e is the equilibrium bond distance for $CO^+(A^2\Pi, v^+=0)$ and D_e = well depth, ω_e^+ = vibrational frequency, and $\omega_e^+\chi_e^+$ = anharmonicity for the Morse potential.

b) Morse potential based on experimental vibrational energies of this work.

c) Morse potential based on vibrational constants cited in Ref. 3.

d) Morse potential based on *ab initio* potential energies calculated in this work.

e) Morse potential based on experimental vibrational energies of Ref. 13.

Table II. Comparison of the experimental and theoretical spin-orbit constants [A_{v^+} (cm^{-1})] for $CO^+(A^2\Pi_{3/2,1/2}, v^+=0\text{-}41)$ and $O_2^+(X^2\Pi_{3/2,1/2g}, v^+=0\text{-}38)$.

	A_{v^+} (cm^{-1})			
V^+	Expt[$CO^+(A^2\Pi)$][a]	Theo[$CO^+(A^2\Pi)$]	Expt[$O_2^+(X^2\Pi)$][c]	Theo[$O_2^+(X^2\Pi)$][b]
0	120.2	115.7 (116.0)	200.2	195.0 (195.1)
1	121.0	115.6 (116.0)	199.5	194.4 (194.8)
2	120.2	115.5 (116.0)	199.0	193.7 (194.5)
3	120.2	115.4 (115.9)	198.5	193.0 (194.2)
4	121.0	115.3 (115.8)	197.6	192.2 (193.9)
5	122.6	115.2 (115.8)	198.0	191.4 (193.7)
6	120.2	115.1 (115.8)	196.6	190.6 193.2)
7	120.2	114.9 (115.7)	195.0	189.7 (192.8)
8	120.2	114.7 (115.7)	193.1	188.8 (192.4)
9	119.4	114.5 (115.6)	192.5	187.8 (192.0)
10	116.1	114.2 (115.6)	192.2	186.8 (191.6)
11	120.2	113.9 (115.5)	191.0	185.8 (191.4)
12	119.4	113.5 (115.5)	190.0	184.7 (190.7)
13	117.0	113.1 (115.4)	189.4	183.5 (190.3)
14	119.4	112.6 (115.4)	188.0	182.3 (189.8)
15	117.0	112.0 (115.3)	187.0	181.0 (189.3)
16	117.0	111.3 (115.3)	185.0	179.8 (188.7)
17	117.0	110.5 (115.2)	183.5	178.4 (188.2)
18	117.0	109.6 (115.2)	183.0	177.0 (187.6)
19	119.4	108.5 (115.2)	179.3	175.5 (187.0)
20	---	107.3	182.0	173.9 (186.3)
21	---	105.8	177.0	172.3 (185.3)
22	109.7	104.2 (116.5)	174.0	170.6 (185.3
23	---	102.3	173.0	168.9 (184.2)
24	103.2	100.3 (130.4)	169.0	167.0 (183.1)
25	101.6	98.0 (111.0)	168.0	165.1 (182.2)
26	99.2	95.5 (111.4)	165.0	163.1 (182.2)
27	96.0	92.8 (111.4)	163.0	161.1 (181.4)
28	94.4	90.0 (111.2)	161.0	159.0 (180.4)
29	91.1	86.9 (110.9)	159.0	156.7 (179.5)
30	88.7	83.8 (110.6)	155.0	154.4 (179.0)
31	85.5	80.6 (108.9)	155.0	152.0 177.4)
32	83.1	77.4 (108.7)	150.0	149.5 (175.6)
33	81.5	74.2 (107.6)	147.0	147.0 (174.4)
34	77.4	71.0 (106.7)	146.0	144.3 (173.0)

Table II. (continued)

35	74.2	67.9 (105.9)	144.0	141.5 (173.7)
36	70.2	64.9 (105.0)	141.0	138.6 (171.6)
37	67.8	61.9 (103.7)	142.0	135.7 (173.0)
38	66.1	59.1 (102.2)	141.0	132.6 (169.3)
39	---	56.4	---	---
40	59	53.7 (96.0)	---	---
41	57	51.2 (92.8)	---	---

a) This work. Experimental A_{v+} values for $CO^+(A^2\Pi_{3/2,1/2}, v^+=0\text{-}41)$.

b) This work. Theoretical A_{v+} values for $CO^+(A^2\Pi_{3/2,1/2}, v^+=0\text{-}41)$ or $O_2^+(X^2\Pi_{3/2,1/2g}, v^+=0\text{-}38)$. calculated using the ab initio Morse potential. Values in parentheses are obtained by the single-point approach based on the $\langle r_e \rangle$ value calculated using Eq. (1).

c) Reference 13. Experimental A_{v+} values for $O_2^+(X^2\Pi_{3/2,1/2})$.

Figure Captions

Figure 1. Comparison of the experimental (solid circles) and BOS simulated (solid line) PFI-PE spectra for (a) $CO^+(A^2\Pi_{3/2,1/2}, v^+=2)$ and (b) $CO^+(A^2\Pi_{3/2,1/2}, v^+=15)$. Positions for individual rotational are indicated using down pointing and up pointing stick marks for the $^2\Pi_{3/2}$ and $^2\Pi_{1/2}$ components, respectively. The rotational branches are labeled as M, N, O. P, Q, R, S, T, and U for ΔN = -4, -3, -2, -1, 0, 1, 2, 3, and 4, respectively. In each ΔN case shown, the position of the first and second transitions are indicated by progressively shorter lines. The PFI-PE resolution achieved = 4 cm^{-1} (FWHM).

Figure 2. Composite simulation spectra for $CO^+(X^2\Sigma^+, v^+=37)$ and $CO^+(A^2\Pi, v^+=38)$. The figure is divided into three panels. Panel (i) [(ii)] compares the experimental PFI-PE spectrum (solid circles) and the deconvoluted (solid line) PFI-PE spectrum for $CO^+(X^2\Sigma^+, v^+=37)$ [$CO^+(A^2\Pi_{3/2,1/2}, v^+=38)$]. Panel (iii) compares the experimental (solid circles) PFI-PE spectrum with the sum of the deconvoluted (solid line) spectra for $CO^+(X^2\Sigma^+, v^+=37)$ and $CO^+(A^2\Pi_{3/2,1/2}, v^+=38)$. In panel (i), positions for individual rotational transitions are indicated by down pointing stick marks. In panel (ii), positions for individual rotational transitions are indicated using down pointing and up pointing stick marks for the $^2\Pi_{3/2}$ and $^2\Pi_{1/2}$ components, respectively. The numbers in panels (i) and (ii) are N″ values. The rotational branches are labeled as M, N, O. P, Q, R, S, T, and U for ΔN = -4, -3, -2, -1, 0, 1, 2, 3, and 4, respectively. The PFI-PE resolution achieved = 4 cm^{-1} (FWHM).

Figure 3. Plot of the experimental and theoretical spin-orbit splitting constants (A_{v+}) for $CO^+(A^2\Pi_{3/2,1/2})$ versus v^+ in the range of v^+=0-41. Experimental values are in solid circles. The theoretical values obtained using the *ab initio* Morse potnetial and by the single-point approach are shown as open circles and triangles, respectively.

Figure 4. PFI-PE spectrum for CO in the energy region of 18.5-20.7 eV. The positions of v^+ levels for $CO^+(X^2\Sigma^+, A^2\Pi_{3/2,1/2}, B^2\Sigma^+)$ are marked in the figure. Note that the oberlap of the weak $CO^+(A^2\Pi_{3/2,1/2}, v^+$=19 and 20) PFI-PE bands with the overwhelmingly strong vibrational band for the $CO^+(B^2\Sigma^+)$ at 19.80 eV.

Figure 5. Plot of the experimental and theoretical spin-orbit splitting constants (A_{v+}) for $O_2^+(A^2\Pi_{3/2,1/2})$ versus v^+ in the range of v^+=0-38. Experimental values are in solid circles. The theoretical values obtained using the *ab initio* Morse potential and by the single-point approach are shown as open circles and triangles, respectively.

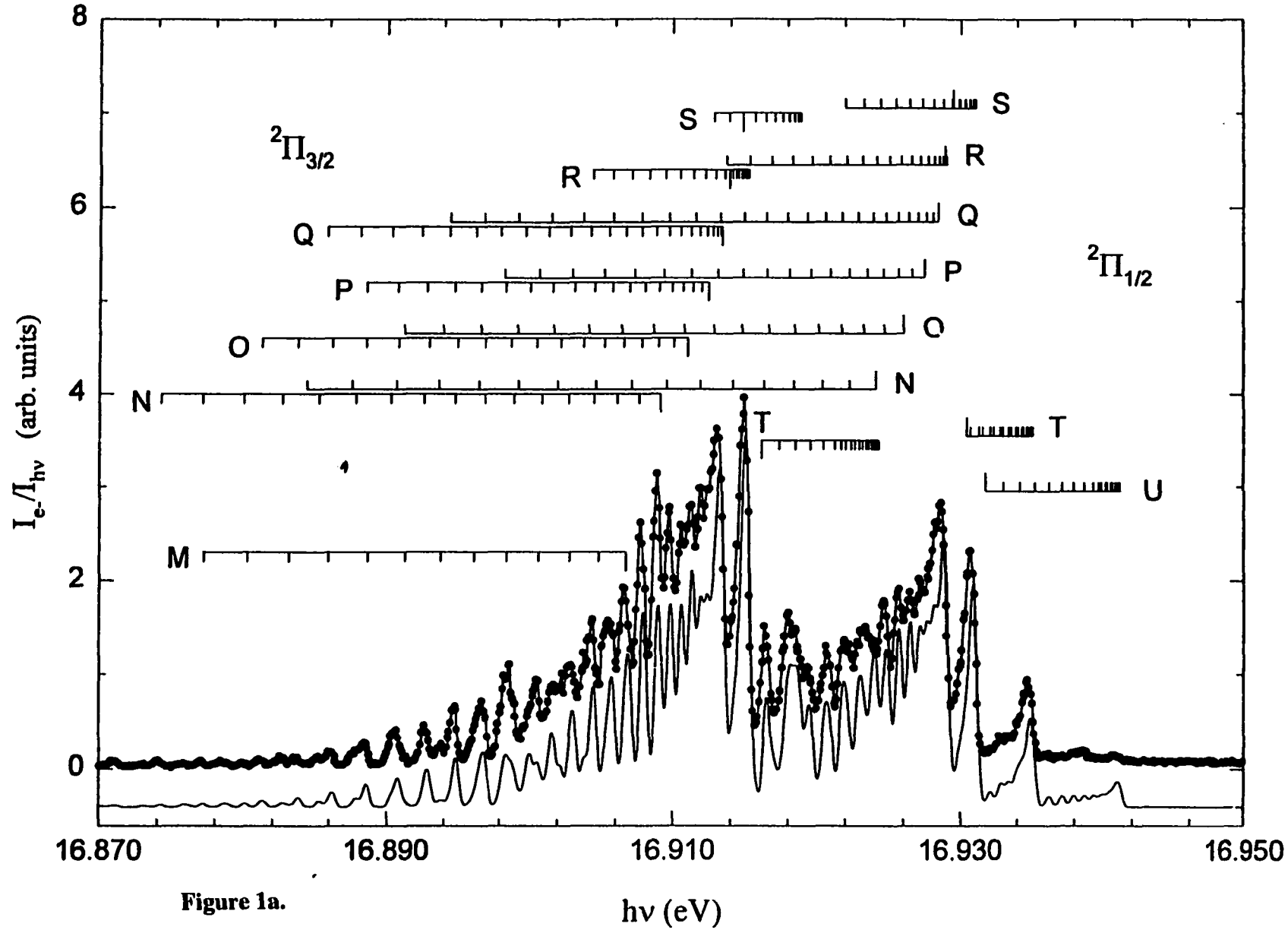
8
6
4
2
0
$I_{e^-}/I_{h\nu}$ (arb. units)
$^2\Pi_{3/2}$
$^2\Pi_{1/2}$
S
R
Q
P
O
N
T
U
M
16.870
16.890
16.910
16.930
16.950
hν (eV)

Figure 1a.

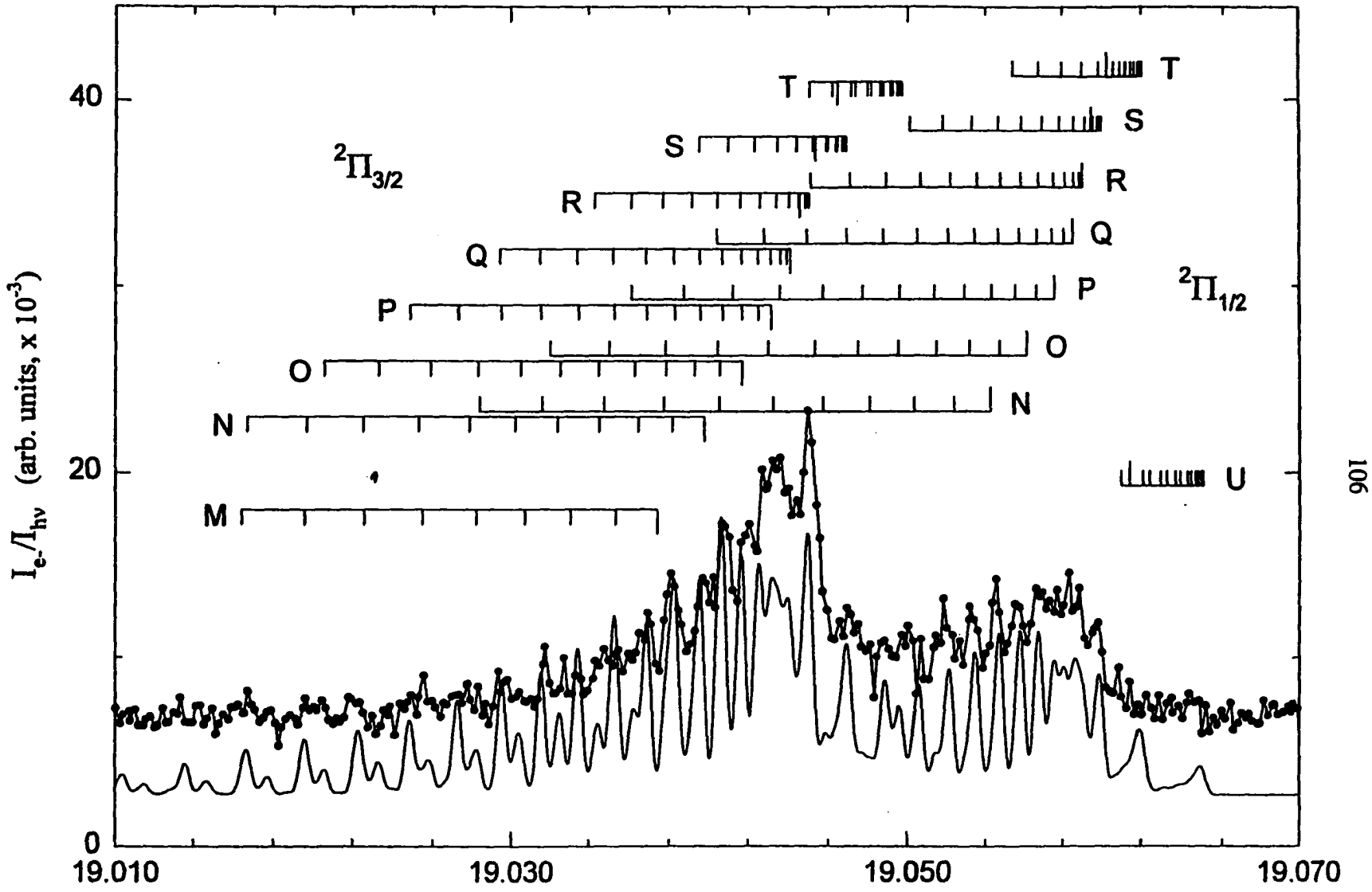
40
20
0
19.010
19.030
19.050
19.070
hν (eV)
$I_{e^-}/I_{h\nu}$ (arb. units, x 10^{-3})
$^2\Pi_{3/2}$
$^2\Pi_{1/2}$
T
S
R
Q
P
O
N
M
U

Figure 1b.

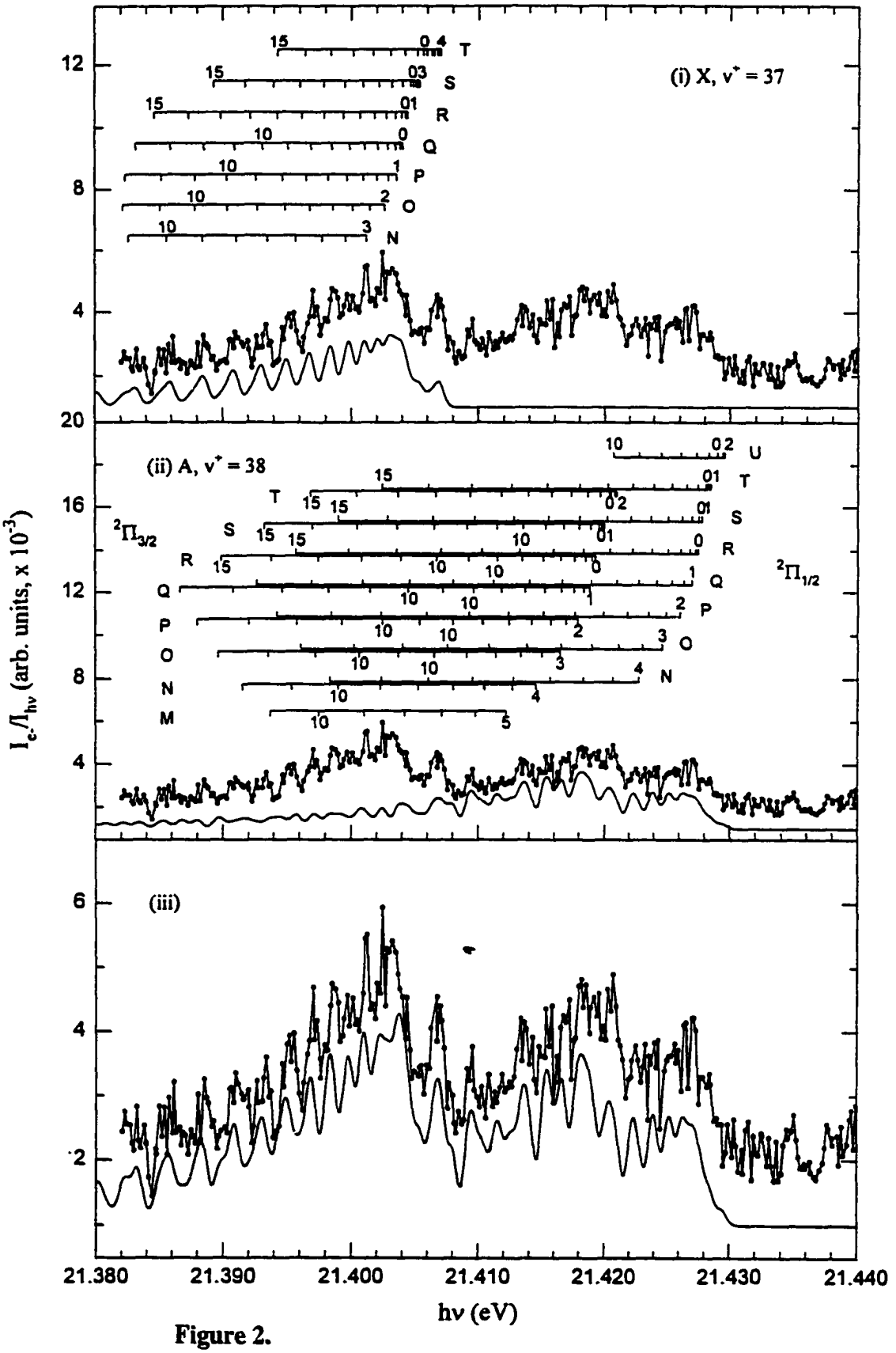
(i) X, v+ = 37
(ii) A, v+ = 38
(iii)
2Π3/2
2Π1/2
T
S
R
Q
P
O
N
M
U
Ic+/Ihν (arb. units, x 10-3)
hν (eV)
21.380
21.390
21.400
21.410
21.420
21.430
21.440

Figure 2.

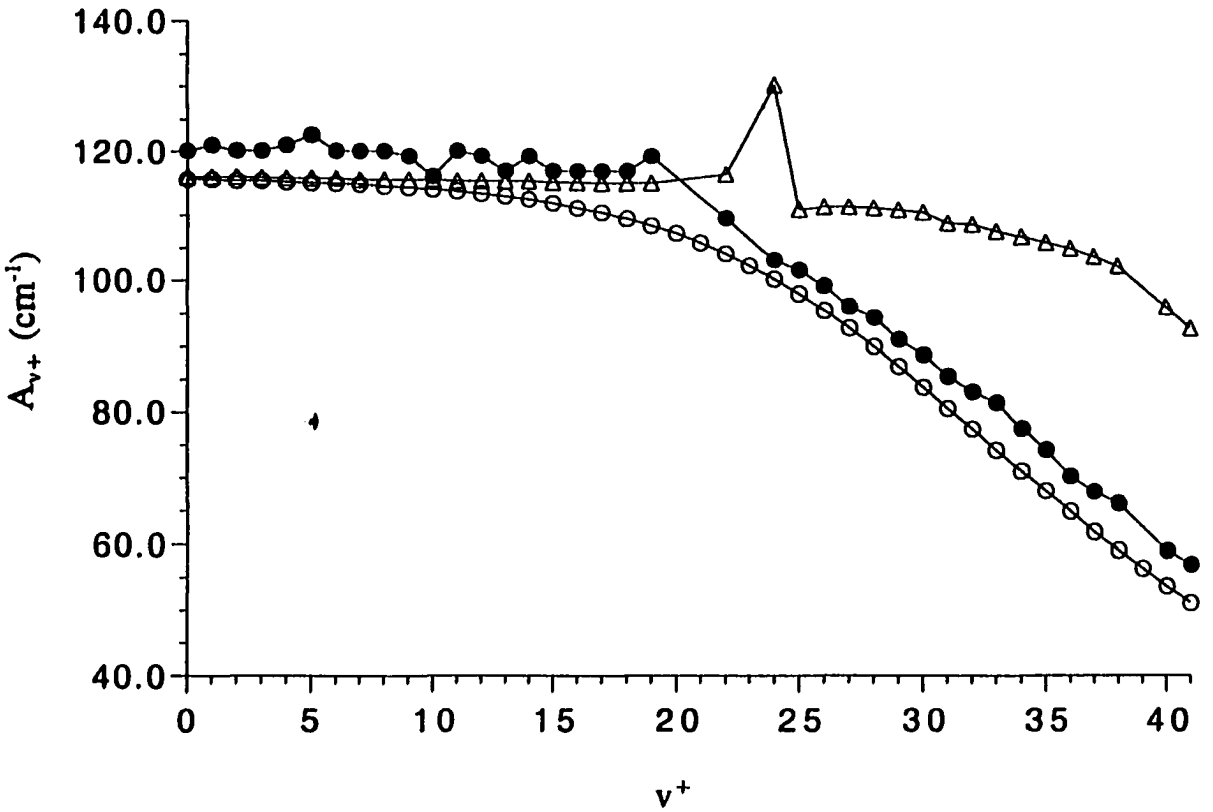

Figure 3.

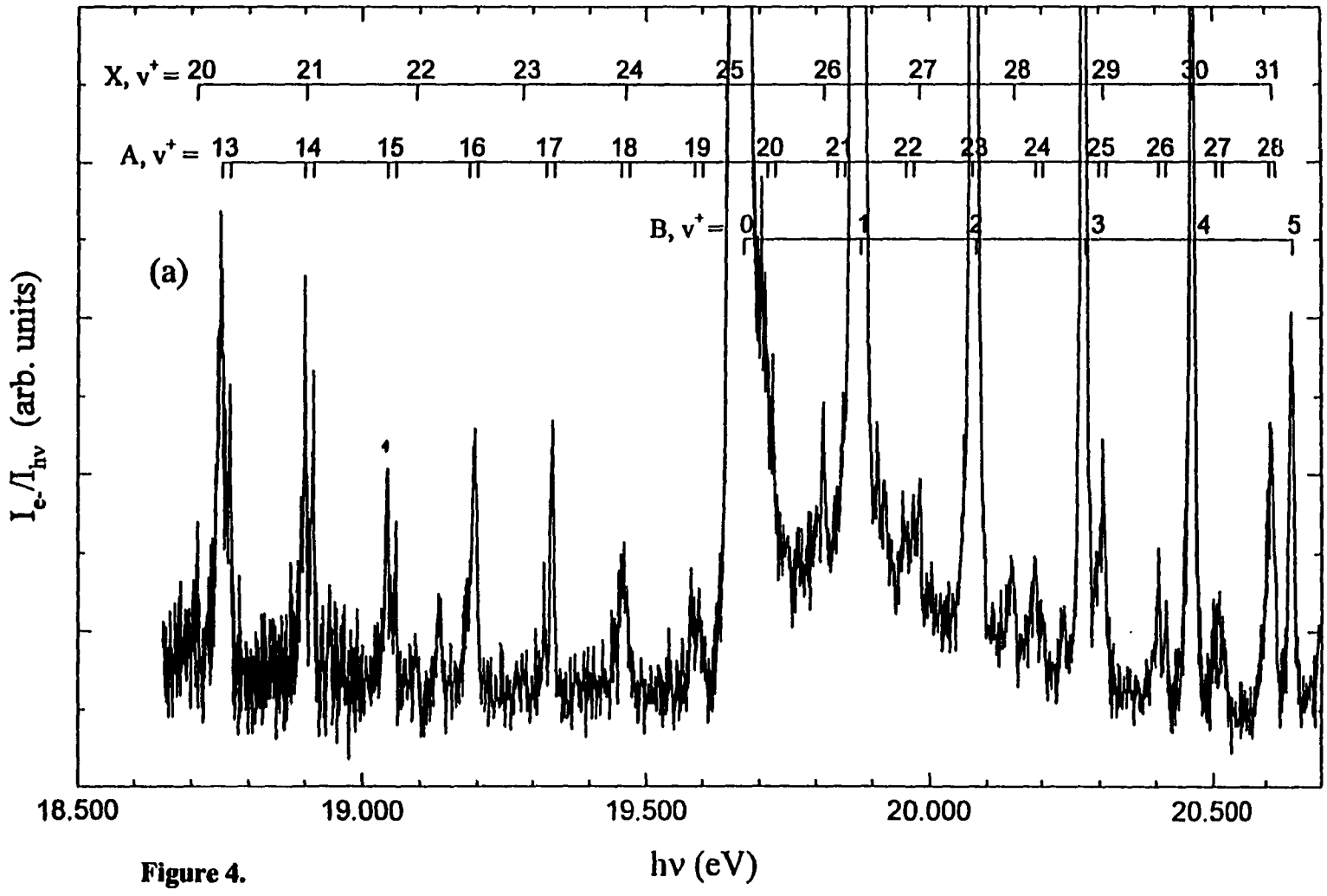
X, v+ = 20 21 22 23 24 25 26 27 28 29 30 31
A, v+ = 13 14 15 16 17 18 19 20 21 22 23 24 25 26 27 28
B, v+ = 0 1 2 3 4 5
(a)
Ie-/Ihν (arb. units)
18.500
19.000
19.500
20.000
20.500
hν (eV)

Figure 4.

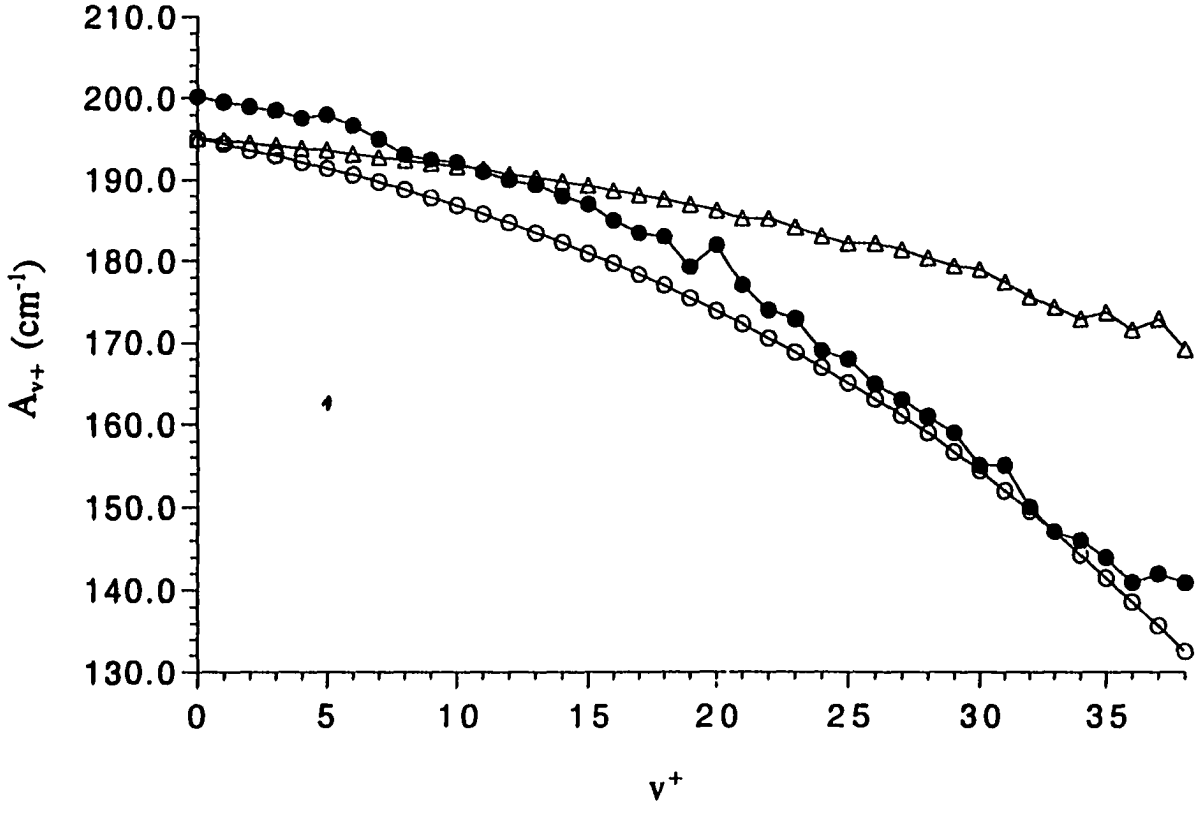
210.0
200.0
190.0
180.0
170.0
160.0
150.0
140.0
130.0
A_{v+} (cm^{-1})
0
5
10
15
20
25
30
35
v^+

Figure 5.

CHAPTER VII. A THEORETICAL STUDY OF THE REACTION OF Ti^+ WITH ETHANE

A paper to be submitted to *J. Phys. Chem.*

Jerzy Moc, Dmitri G. Fedorov and Mark S. Gordon

Abstract

Both the doublet and quartet potential energy surfaces for the $Ti^+ + C_2H_6 \rightarrow TiC_2H_4^+ + H_2$ and $Ti^+ + C_2H_6 \rightarrow TiCH_2^+ + CH_4$ reactions are studied using density functional theory (DFT) with the B3LYP functional and ab initio CCSD(T) methods with high quality basis sets. Structures have been optimized at the DFT level and the minima connected to each TS by following the intrinsic reaction coordinate (IRC). Relative energies are calculated both at the DFT and Coupled Cluster levels of theory.

I. INTRODUCTION

Experimental studies of gas-phase reactions of the first-row transition-metal cations with simple alkanes provide valuable insight into the mechanism and energetics of C-H and C-C bond activation.[1] Insertion of the metal into C-H and/or C-C bonds is common and eventually leads to the elimination of H_2 or small alkanes.[1] In particular, several studies of Ti^+ reacting with ethane in the gas phase were conducted during the last 15 years using various mass spectrometric and ion beam techniques.[2-6] In the early experiment by the Freiser group,[2] an ion cyclotron resonance (ICR) method was used. Under single-collision conditions, only the C-H insertion leading to the H_2 elimination products, $TiC_2H_4^+ + H_2$, was observed[2]. Weisshaar and co-workers[3] employed a flow tube reactor technique to study the gas phase

reaction of Ti^+ with C_2H_6. In the multiple-collision environment of the flow reactor containing He buffer gas, the primary products found by these researchers were the adduct ions $TiC_2H_6^+$ and elimination products $TiC_2H_4^+ + H_2$, with the product distribution at 300K determined to be 0.55 and 0.45, respectively.[3] Tolbert and Beauchamp,[4] who used an ion beam method observed at a relative kinetic energy of 0.5 eV (11.5 kcal/mol) both the major elimination products $TiC_2H_4^+ + H_2$ and minor double elimination products, $TiC_2H_2^+ + 2H_2$, with a product distribution of 0.96 and 0.04, respectively. Based on the Ti^+ reactions with partially deuterated ethane, CH_3CD_3, Tolbert and Beauchamp suggested a 1,2-elimination mechanism for the dehydrogenation.[4] In the experiment of Sunderlin and Armentrout,[5] a guided-ion beam tandem mass spectrometer was used to examine the $Ti^+ + C_2H_6$ reaction, with the applied kinetic energies ranging from thermal to several eV. Six products were observed by these workers, with the H_2 elimination products indicated to be dominant at low energies.[5] The most recent experimental study on the gas-phase reaction of Ti^+ with ethane at thermal energies was conducted by Castleman group[6] using the flow tube reactor technique. Consistent with the findings of Weisshaar,[3] the primary products observed by Castleman[6] under multiple-collision conditions were the adduct ions $TiC_2H_6^+$ and elimination products $TiC_2H_4^+ + H_2$, followed by the minor double elimination products $TiC_2H_2^+ + 2H_2$, with the product distribution determined as 0.30, 0.66 and 0.04, respectively.

In the present theoretical study, DFT and ab initio type calculations were carried out for the $Ti^+ + C_2H_6 \longrightarrow TiC_2H_4^+ + H_2$ and $Ti^+ + C_2H_6 \longrightarrow TiCH_2^+ + CH_4$ elimination reactions. The details of the potential energy surfaces (PES) involved were elucidated and the following particular issues were addressed:

(1) What is the actual structure of the adduct ions observed[3,6] in the flow tube experiments?

(2) Why were only the H_2 elimination products observed at low energies,[2-6] whereas the CH_4 elimination products were not?

(3) Is the H_2 elimination reaction of 1,1- or 1,2-type?

(4) How important are spin-orbit effects on the $Ti^+ + C_2H_6$ reaction?

II. COMPUTATIONAL METHODS

Structures were optimized at the density functional theory (DFT) level[7,8,22], using the hybrid B3LYP[9-11] functional of the form:

$(1-A)F_x^{Slater} + A\,F_x^{HF} + B\,F_x^{Becke} + C\,F_C^{LYP} + (1-C)F_C^{VWN}$

where F_x^{Slater} is the Slater exchange, F_x^{HF} is the Hartree-Fock exchange, F_x^{Becke} is the gradient part of the exchange functional of Becke,[9-10] F_C^{LYP} is the correlation functional of Lee, Yang and Parr,[12] F_C^{VWN} is the correlation functional of Vosko, Wilk and Nusair,[13] and A, B, C are the coefficients determined by Becke[9-10] using a fit to experimental heats of formation. The DFT force constant matrix was calculated[22] at each stationary point to confirm its character (minimum or transition state (TS)) as well as to evaluate zero-point vibrational energy (ZPVE) corrections, which were included in all the relative energies. To verify each pair of intermediates connected by a TS, the DFT intrinsic reaction coordinate (IRC)[14,15] was determined.[15]

The DFT B3LYP calculations employed the all-electron valence triple-ζ plus polarization (TZVP) basis set. For Ti, it consisted of the [10s6p] contraction of the (14s9p) primitive set developed by Wachters[16] combined with the [3d] contraction of the (6d) primitive set taken from Rappé et al.[17] Wachters' sp basis was modified by replacing the most diffuse s function with one spanning the 3s-4s region (α_s=0.209) and by adding two sets of p functions (α_p=0.156 and 0.0611).[18] For C, the TZVP basis was composed of Dunning's[19] [5s3p] contraction of Huzinaga's (10s6p) primitive set,[20] augmented by a set of d polarization functions (α_d=0.72). Similarly, for H, the [3s] basis derived[19] from the (5s) primitive set,[20] and augmented by a set of p polarization functions (α_p=1.0) was used as TZVP.

The DFT B3LYP relative energies are compared with those determined by the coupled-cluster singles and doubles method including a perturbative estimate of triples (labeled CCSD(T)).[21] The large basis set denoted 6-311+G(2d,2p) in GAUSSIAN 94[22a] was used in the CCSD(T) calculations. For Ti, this basis consists of the [9s5p3d] contraction of Wachters (14s9p5d) primitive set,[16] supplemented with one diffuse s (α_s=0.01),[23] two sets of diffuse p (α_p=0.1016 and 0.0340)[16] and one set of diffuse d functions (α_d=0.072)[24] as well as two sets of f polarization functions (α_f=1.38 and 0.345).[22a,25]

The relevant parts of the potential energy surface were studied with CASSCF wavefunctions and the final energetics were obtained at the MCQDPT2 level of theory. The active space always included all 6 valence 4s3d orbitals on Ti and the relevant C-H bonds in the pairs of bonding/antibonding orbitals.

Since the potential energy surfaces of quartet and doublet appear to cross, and this crossing can affect the kinetics dramatically, the non-adiabatic coupling potential at the crossing (spin-orbit coupling) was studied. The spin-orbit coupling was calculated with the TZV basis set augmented with one f-polarization function for Ti and full Pauli-Breit Hamiltonian[39] using GAMESS (for CASSCF wavefunctions). Non-orthogonal orbitals are used throughout; that is, the active orbitals are optimised for each multiplicity separately, but common core orbitals are used for both.

Three slightly different approaches were taken to locate the crossing of the doublet and quartet surfaces.

1) follow the doublet IRC and calculate quartet energies for the corresponding doublet geometries at the IRC points.

2) follow the quartet IRC and calculate the doublet energies at these IRC points.

3) average the internal coordinates for the doublet and quartet IRC point near the crossing. Then emulate the IRC by varying the C-H bond distance, which is broken along this path (the

imaginary mode of the complex d is mostly along the separation of the two atoms), and calculate doublet and quartet energies. This is called averaged IRC.

III. RESULTS AND DISCUSSION

A. Reactants and Products

The ground state of Ti^+ is ^4F ($4s^13d^2$) and the lowest doublet state is ^2F ($4s^13d^2$), the latter lying 13.2 kcal/mol higher in energy than the former.[27] As Table 1 shows, the ^2F-^4F splitting obtained by the MCQDPT2 method based on the multiconfigurational CASSCF (3/6) wave function (three active electrons in six active orbitals) compares most favourably with experiment. The ^2F state of Ti^+ is a three-electron doublet state and is difficult to describe with single configurational methods due to near degeneracy effects. Nevertheless, the DFT B3LYP estimate of the ^2F-^4F splitting is within 1 kcal/mol of the experimental result.[28] The CCSD(T) splitting on the other hand appeared to be unreasonably low due to an overestimation of the correlation energy for the ^2F state.

The optimized structure of the second reactant C_2H_6, as well as those corresponding to the dehydrogenation and demethanation products of C_2H_6 by Ti^+, $TiC_2H_4^+ + H_2$ and $TiCH_2^+ + CH_4$, respectively, are depicted in Fig. 1. As expected,[10b,31] DFT B3LYP reproduces the geometrical parameters of C_2H_6, CH_4 and H_2 very well. For the H_2 elimination product, $TiC_2H_4^+$, DFT predicts the quartet ($^4B_1$) to be the ground state separated from the lowest doublet state ($^2A_1$) by 1.8 kcal/mol, while the CCSD(T) order is reversed with the $^2A_1$ becoming the ground state, lying however only 0.2 kcal/mol below the $^4B_1$. Sodupe et al[32] predicted the $^2A_1$ ground state for $TiC_2H_4^+$ with the high-spin state $^4B_1$ being 5.2 kcal/mol less stable. These authors optimized their structures at the SCF level and calulated energies using the modified coupled-pair functional (MCPF) method.[32] For the the $^2A_1$ state, our DFT structure of $TiC_2H_4^+$ (Fig. 1b) is similar to that of Sodupe et al.[32] In particular, we also predict

a relatively short Ti^+-C_2H_4 distance and a significant H bend angle. For the $^4B_1$ state, a major difference between the present DFT geometry and the SCF one[32] is a much shorter Ti^+-C_2H_4 distance of 2.287 Å in the former (Fig. 1b) as compared to 2.82 Å in the latter. The DFT structure of the $^4B_1$ state of $TiC_2H_4^+$ is supported by our additional geometry optimization using the coupled-cluster doubles (CCD)[21] approach yielding, respectively, 2.347 Å and 9.9° for the Ti^+-C_2H_4 distance and H bend angle. Apparently, dynamic correlation implicit to some degree in DFT B3LYP and explicit in CCSD(T) shortens markedly the Ti^+-C_2H_4 interaction distance for the quartet state relative to the SCF finding.

The CH_4 elimination product, $TiCH_2^+$, was studied previously at both ab initio and DFT levels.[33] The most recent DFT B3LYP work by Ricca and Bauschlicher[33a] revealed that the C_{2v} structure of $TiCH_2^+$ distorts to C_s as the latter symmetry allows donation from one of the C-H bonds to the empty Ti 3d orbital. Our DFT B3LYP geometry of $TiCH_2^+$ in its lowest $^2A'$ state (Fig. 1c) agrees well with that of Ricca and Bauschlicher.[33a] The $TiCH_2^+$ lowest quartet state, $^4A''$ (Fig. 1c) (not reported in Ref. 33a) is found here to have nearly C_{2v} symmetry and lie 8.4 and 8.6 kcal/mol above $^2A'$ at the DFT B3LYP and CCSD(T) levels, respectively.

B. Initial Complexes

An electrostatically bound complex $Ti^+\cdots C_2H_6$ was proposed[3] as one candidate for the observed[3,6] $TiC_2H_6^+$ adduct ions. The computed structures for such complexes formed in the first step of the reaction between Ti^+ and C_2H_6 are denoted **a1** and **a2** in Fig. 2 and **a** in Figs. 3 (doublet) and 4 (quartet), and are shown in both doublet and quartet states. Structure **a1** corresponds to an end-on approach of Ti^+ toward C_2H_6, while **a** and **a2** correspond to a side-on approach. Only C_s structures **a** and **a1** involving η^3 coordination appeared to be minima on both surfaces, while η^2 coordinated structure **a2** of C_2 symmetry produced one imaginary

frequency with the eigenvector clearly indicating distortion to **a**.[34] As Ti^+ has a quartet ground state, so have the electrostatic complexes **a** and **a1** ($^4A''$). Complex **a** ($^4A''$) is bound by 20.1 and 15.6 kcal/mol relative to the C_2H_6 + $Ti^+(^4F)$ reactants at the DFT B3LYP and CCSD(T) levels, respectively. The corresponding binding energies obtained for the complex **a1** are 18.7 and 14.9 kcal/mol, respectively. On the the doublet surface, complexes **a** and **a1** are bound by 20.5 and 20.1 kcal/mol with respect to C_2H_6 + $Ti^+(^2F)$ at the DFT B3LYP level. As CCSD(T) breaks down for the doublet state of Ti^+, no reliable binding energies could be obtained at this level for the doublet **a** and **a1**. However, based on the results for the quartet surface, one may predict that the DFT doublet binding energies are also a few kcal/mol too large.

Starting from the $Ti^+\cdots C_2H_6$ complex, metal insertion into a C-H or C-C bond can be considered as the next reaction step. The C-H insertion described below starts from the complex **a**. Initially we also explored this important step as eventually leading to the observed H_2 elimination products beginning with both the **a** and **a1** complexes (on the doublet surface, see below). The energy of the C-H insertion TS connecting complex **a1** with the corresponding product was 0.5 kcal/mol lower than the energy of the TS connecting complex **a**, but the former TS leads to an energetically less favorable product, by *ca.* 10 kcal/mol at the DFT B3LYP level. Therefore, we did not pursue the "**a1** path" further.

The complete reaction paths for the H_2 and CH_4 eliminations will be discussed next. Figs. 3 and 4 summarize all of the calculated structures for the doublet and quartet states, respectively. The energies relevant to the H_2 and CH_4 eliminations are collected in Tables 2 and 3, and the corresponding energy profiles are depicted in Fig. 5 and Fig. 6, respectively. For each species the energy given is relative to the ground-state reactants C_2H_6 + $Ti^+(^4F)$ and includes the ZPVE correction. The structure labels in Tables 2 and 3 and Figs. 5 and 6 correspond to those used in Figs. 3 and 4.

C. H_2 elimination path

The C-H insertion step in the H_2 elimination reaction involves breaking a C-H bond in **a** and forming the insertion product **e**, $HTiC_2H_5^+$ (oxidative addition), shown in Figures 3 and 4. On the doublet surface, the B3LYP energy of **e** (C_1 symmetry) decreases by 4.8 kcal/mol relative to the complex **a.** This structure has a C-Ti distance of 2.00 Å and a nearly perpendicular C-C-Ti arrangement. The corresponding C-H insertion TS **d** is "product-like" with only slightly shorter C-Ti bond (Fig. 3). The barrier height at this (adiabatic) doublet TS is 5.2 (9.0) kcal/mol at DFT(CCSD(T)) level of theory (Table 2). The MCQDPT2 barrier is 8.0 kcal/mol. In contrast, on the quartet surface, the energy of **e** increases with respect to **a** by 37.2(37.7) kcal/mol at the DFT (CCSD(T)) level. Since the quartet C-H insertion TS **d** is obviously shifted even higher in energy, a crossing occurs between the quartet and doublet surfaces in this region (cf. Fig. 5). This implies that the reaction will subsequently proceed on the doublet surface if the surface coupling potential is sufficiently large. The crossing apparently precedes (Figures 5a and 5c) the doublet C-H insertion TS **d** which determines the actual insertion barrier. In the next step on the doublet surface, the Ti-H bond in the C-H insertion product **e** rotates via TS **f** to the rotamer **g**, the latter having a planar structure (^{2}A") with a slightly longer C-Ti bond than that in **e** (Fig. 3). All levels of theory agree that after accounting for the ZPVE correction, the rotation TS **f** becomes lower in energy than **g**, so that the rotamer may not correspond to a genuine minimum (Fig. 5), and the TS **f** may be irrelevant. Both DFT (Figure 5a) and MCQDPT2 (Figure 5c) find that **f** and **g** lie well below the C_2H_6 + Ti^+(^{4}F) reactants, whereas CCSD(T) locates the two species slightly above this asymptote. All methods predict **e** to be below the asymptote.

On the quartet surface (Fig. 5) all species between **a** and **g** lie well above the C_2H_6 + Ti^+ (^{4}F) asymptote. Unlike the doublet, the quartet Ti^+ apparently cannot form stable insertion products. For instance, after forming an H-Ti bond in the quartet structure **e**, by singlet

coupling by a pair of electrons, the missing spin contribution is "borrowed" from the neighbouring C atom to conserve the quartet character. This is confirmed by the calculated spin density distribution in the quartet **e** of *ca.* 2.2 and 0.8 on the Ti and neighbouring C atoms, respectively. The quartet structures show correspondingly much weaker C-Ti bonds with the distances longer by *ca.* 0.4 Å as compared to the doublet counterparts (cf. Figs. 3 and 4).

In the next step on the doublet surface, the $HTiC_2H_5^+$ rotamer **g** can undergo reductive elimination via the planar H_2 elimination TS **j** to form the molecular complex $TiC_2H_4^+\cdots H_2$(**k**) (Fig. 3). The latter C_s (2A") intermediate has the H_2 unit rotated in the C-C-Ti symmetry plane. Also, it exhibits asymmetrically lengthened Ti-C bonds and a shortened C-C bond relative to the $TiC_2H_4^+(^2A_1)$ product. These structural changes are indicative of the weakening of the Ti^+-C_2H_4 interaction within the molecular complex **k** in the doublet state as compared to $TiC_2H_4^+(^2A_1)$. The DFT C_{2v} $TiC_2H_4^+\cdots H_2$ structure with the H_2 unit perpendicular to the C-C-Ti plane is 1.4 kcal/mol higher in energy and has two imaginary frequencies. The corresponding normal mode eigenvectors indicate distortions leading to **k**. For the reductive elimination step DFT B3LYP predicts a barrier of 1.5 kcal/mol above the C_2H_6 + $Ti^+(^4F)$ reactants with the resulting complex **k** located 1.8 kcal/mol below this asymptote. According to CCSD(T), the reductive elimination step must conquer a higher barrier of 9.5 kcal/mol above C_2H_6 + $Ti^+(^4F)$ (comparable to the CCSD(T) C-H insertion barrier), and the complex **k** is located 6.2 kcal/mol above this asymptote (Fig. 5). The MCQDPT2 surface is more similar to the DFT result, since it predicts that all points after the insertion step **d** are below the asymptote.

On the quartet surface, the electrostatic complex $TiC_2H_4^+\cdots H_2$ **k** is a very stable structure, well below the asymptote according to both DFT and MCQDPT2. The quartet **k** has C_{2v} symmetry ($^4A_2$) with the H_2 unit perpendicular to the C-C-Ti plane (Fig. 4).[35] Since the C-Ti and C-C distances in quartet **k** and the $TiC_2H_4^+(^4B_1)$ product (Fig. 1) are nearly the

same, the weakening of the Ti^+-C_2H_4 interaction within the quartet complex **k** relative to $TiC_2H_4^+(^4B_1)$ should be smaller than that in the doublet case discussed above. Indeed, all levels of theory predict that the molecular complex **k** in the quartet state is lower in energy than the doublet counterpart. The DFT quartet **k** is 6.8 kcal/mol below $C_2H_6 + Ti^+(^4F)$, whereas the CCSD(T) energy at this point is 3.1 kcal/mol above this asymptote. As a result, another spin crossing occurs in this region and the H_2 elimination proceeds back to the original (quartet) surface (Fig. 5).

In the final step the H_2 molecule is eliminated yielding the $TiC_2H_4^+$ product. According to DFT, the latter is left in the quartet state at a net cost of 5.2 kcal/mol, and the overall H_2 elimination reaction starting with the $C_2H_6 + Ti^+(^4F)$ reactants is slightly exothermic, by 1.2 kcal/mol (Figure 5a). The CCSD(T) calculations predict that $TiC_2H_4^+$ is left in the doublet state and the overall H_2 elimination reaction is slightly endothermic, by 7.5 kcal/mol (Fig. 5b). The MCQDPT2 calculations are in qualitative agreement with CCSD(T), since this method predicts a doublet final product with a net cost of less than 8.0 kcal/mol and essentially a thermoneutral reaction.

D. CH_4 elimination path

Both H_2 and CH_4 elimination paths stem from the complex **a**. Moreover, on the doublet surface, the C-H insertion step is common for the two paths (Fig. 6). In the next step on that surface, the $HTiC_2H_5^+$ intermediate **e** can be transformed to the $Ti(CH_3)_2^+$ dimethyl cation **c** via the four-center TS **b** (Fig. 3). The latter TS leads from the C-H insertion product to the C-C insertion product and features partially broken C-C and C-H bonds. The optimal structure of $Ti(CH_3)_2^+$ **c** is bent and has C_s symmetry ($^2A'$) with the two methyls eclipsed and the two in-plane hydrogens nearer each other than the four out-of-plane hydrogens (Fig. 3). A DFT C_{2V} structure with the same orientation of the methyls was found to be 0.04 kcal/mol higher in

energy and showed a small imaginary frequency with the eigenvector indicating rotation of both methyls in the same direction. The barrier is predicted to be 16.7 (25.0) kcal/mol above the C_2H_6 + $Ti^+(^4F)$ reactants at the DFT (CCSD(T)). DFT predicts that the $^2A'$ state is the global minimum, lying 22.1 kcal/mol below C_2H_6 + $Ti^+(^4F)$ and 2 kcal/mol below quartet **a**. In comparison, the CCSD(T) $^2A'$ **c** is 11.6 kcal/mol below C_2H_6 + $Ti^+(^4F)$ and 4 kcal/mol above quartet **a** (Fig. 6). A "direct" C-C insertion TS from the complex **a** to the dimethyl species **c** was also found. However, because this DFT TS is strongly spin contaminated, this part was not pursued.

Insertion of Ti^+ in the quartet state into the C-C bond is not thermodynamically favorable as discussed earlier for the C-H insertion. The dimethyl species **c** on the quartet surface is 31 and 34 kcal/mol above complex **a** at the DFT and CCSD(T) levels, respectively. Consequently, a surface crossing occurs similar to that found for the H_2 elimination. Assuming significant spin--orbit coupling, the reaction moves to the doublet surface and remains there as the quartet surface is shifted to much higher energies (cf. Fig. 6). Despite a very careful search we failed to locate the quartet C-C insertion TS. This TS (if it exists) is assumed to lie not lower than 11.0 kcal/mol (DFT) or 18.3 kcal/mol (CCSD(T)) above C_2H_6 + $Ti^+(^4F)$.

The next step on the doublet surface is 1,3 hydrogen migration leading to the molecular complex $TiCH_2^+\cdots CH_4$(**i**) (Fig. 3). The complex **i** is found to lie 3.4 kcal/mol below and 1.9 kcalmol above C_2H_6 + $Ti^+(^4F)$ at DFT and CCSD(T), respectively. In order to reach **i**, TS **h** located respectively 8.1 and 15.1 kcal/mol above the same asymptote has to be passed. Complex **i** involves η^2 coordinated CH_4 and was obtained by following the IRC. The "asymmetrical" $TiCH_2^+$ product already formed within **i** can be easily recognized (cf. Figs. 1c and 3). The DFT C_s symmetry η^3 coordinated structure of $TiCH_2^+\cdots CH_4$ is *ca.* 3 kcal/mol less stable and has one imaginary frequency with the eigenvector showing distortion to C_1. The final step for this mechanism is a release of a CH_4 molecule at the cost of 14.4 and 15.1

kcal/mol, at the DFT and CCSD(T) levels, respectively. The overall CH_4 elimination reaction starting with the C_2H_6 + $Ti^+(^4F)$ reactants is found to be endothermic by 11.0 and 17.0 kcal/mol, respectively.

Although once the complex **a** is formed, the quartet surface is not involved in the CH_4 elimination reaction, this path and the relevant structures are included for comparison purposes. The quartet $Ti(CH_3)_2^+$ species **c** exhibits a symmetry breaking as evident by the inequivalent Ti-C bonds (Fig. 4).[36] The quartet complex **i** is 9.4 (DFT) or 10.8 kcal/mol (CCSD(T)) less stable than the doublet analogue, which corresponds roughly to the doublet-quartet splitting for the $TiCH_2^+$ product discussed above.

E. Spin-orbit coupling

For all of the three approaches described in Section II and pictured on Figures 7-9 the spin-orbit coupling constant (defined as the square root of the sum of squares of the absolute values of H_{so} matrix elements) is found to be essentially the same at the crossing point that occurs along the reaction path from complex **a** to **d** and the value of C=50-55 cm^{-1} was obtained. The levels at the crossing are given in Figure 10. The value of C=52.5 cm^{-1} was normalised by the level degeneracy $C^2/(2S+1)$, S=1/2 and used for the square of the diabatic potential to estimate the Landau-Zener (Ref 2) transition probability. The probability is plotted in Figure 11. The value at room temperature is 13.4%.

The value of the spin-orbit coupling constant is smaller than can be expected for a compound containing an atom as heavy as titanium, however, it is large enough to alter the course of the otherwise energy forbidden reaction (at room temperature) to allow a channel of the quartet state of the reactants to proceed to the energetically accessible doublet surface. Interestingly, another two potential energy crossings appear to occur near the reactants. However they do not appear to affect the dynamics to a significant extent due to small energy

differences of the two surfaces.

IV. CONCLUSIONS

(i) We found that the $Ti^+ + C_2H_6 \longrightarrow TiC_2H_4^+ + H_2$ and $Ti^+ + C_2H_6 \longrightarrow TiCH_2^+ + CH_4$ elimination reactions start with formation of the η^3 coordinated $Ti^+\cdots C_2H_6$ electrostatic complex in the quartet state. Due to instability of the quartet C-H and C-C insertion products relative to the doublet counterparts, a spin crossing occurs next and the two reactions proceed on the low-spin surface.

(ii) The overall H_2 elimination reaction is calculated to be slightly exothermic by 1.2 (.3) kcal/mol at the DFT B3LYP (MCQDPT2) level and slightly endothermic (by 7.5 kcal/mol) at the CCSD(T) level. The C-H insertion TS (DFT B3LYP) or C-H insertion TS and H_2 elimination TS (CCSD(T)) are the highest energy points en route to the products, lying respectively 5.2, 9.0 and 9.5 kcal/mol above the ground-state reactants $C_2H_6 + Ti^+(\ ^4F)$. For the Co^+- and Fe^+-mediated elimination of H_2 from C_2H_6 studied recently,[37] the C-H insertion TS was located below the entrance channel and the H_2 loss TS was the rate determining step. The higher relative energy of the C-H insertion TS in the Ti^+ case results from the more shallow potential well of its initial complex as compared to the Co^+ and Fe^+ analogues. The actual depth of this well determines whether insertion barriers lie below or above the entrance channel.[38] Finally, consistent with the labelling experiments,[4] our results suggest the 1,2 H_2 elimination mechanism.

(iii) The overall CH_4 elimination reaction is predicted to be significantly endothermic, by 11.0 and 17.0 kcal/mol at the DFT B3LYP and CCSD(T) levels, respectively. Although the C-C insertion product, $Ti(CH_3)_2^+$, is a low energy intermediate (the global minimum at DFT B3LYP), a high C-C insertion barrier of 16.7 kcal/mol (DFT B3LYP) or 25 kcal/mol (CCSD(T)) above $C_2H_6 + Ti^+(\ ^4F)$ prevents from observing this species under thermal

conditions. Based on the calculated energy profiles we suggest the initial complex $Ti^{+}\cdots C_2H_6$ in the quartet state to be a likely candidate for the adduct ion stabilized in the flow tube experiments.[3,6]

References

(1) (a) van Koppen, P.A.M.; Kemper, P.R.; Bowers, M.T. In *Organometallic Ion Chemistry*; Freiser, B.S., Ed.; Kluwer Academic Publishers: Dordrecht, The Netherlands,1996; p 157. (b) Armentrout, P.B. In *Gas-Phase Inorganic Chemistry* ; Russell, D.H., Ed.; Plenum Press: New York,1989; p 1. (c) Armentrout, P.B. In *Selective Hydrocarbon Activation: Principles and Progress*, Davies, J.A.; Watson, P.L.; Liebman, J.; Greenberg, A., Eds.; VCH: New York,1990; p 467. (d) Weisshaar, J.C. In *Advances in Chemical Physics*, Ng, C., Ed.; Wiley Interscience: New York,1992; Vol.82, pp 213-261.

(2) Byrd, G.D.; Burnier, R.C.; Freiser, B.S. *J.Am.Chem.Soc.* **1982**,104,3565.

(3) (a) Tonkyn, R.; Weisshaar, J.C. *J.Phys.Chem.* **1986**,90,2305. (b) Tonkyn, R.; Ronan, M.; Weisshaar, J.C. *J.Phys.Chem.* **1988**,92,92.

(4) Tolbert, M.A.; Beauchamp, J.L. *J.Am.Chem.Soc.* **1986**,108,7509.

(5) Sunderlin, L.S.; Armentrout, P.B. *Int.J.Mass Spectrom. Ion Processes* **1989**,94,149.

(6) MacTaylor, R.S.; Vann, W.D.; Castleman, Jr., A.W. *J.Phys.Chem.* **1996**,100,5329.

(7) Parr, R.G.; Yang, W. *Density Functional Theory of Atoms and Molecules* ; Oxford University Press: Oxford, U.K.,1989.

(8) *Density Functional Methods in Chemistry* ; Labanowski, J.K.; Andzelm, J.W., Eds.; Springer: Berlin,1991.

(9) Becke, A.D. *Phys.Rev. A* **1988**,38,3098.

(10) (a) Becke, A.D. *J.Chem.Phys.* **1993**,98,1372. (b) Becke, A.D. *J.Chem.Phys.***1993**,98,5648.

(11) Stevens, P.J.; Devlin, F.J.; Chabalowski, C.F.; Frisch, M.J. *J.Phys.Chem.* **1994**,98,11623.

(12) Lee, C.; Yang, W.; Parr, R.G. *Phys. Rev. B* **1988**,37,785.

(13) Vosko, S.H.; Wilk, L.; Nusair, M. *Can.J.Phys.* **1980**,58,1200.

(14) (a) Fukui, K. *Acc.Chem.Res.* **1981**,14,363. (b) Ishida, K.; Morokuma, K.; Komornicki, A. *J.Chem.Phys.* **1977**,66,2153. (c) Schmidt, M.W.; Gordon, M.S.; Dupuis, M. *J.Am.Chem.Soc.* **1985**,107,2585. (d) Garrett, B.C.; Redmon, M.J.; Steckler, R.; Truhlar, D.G.; Baldridge, K.K.; Bartol, D.; Schmidt, M.W.; Gordon, M.S. *J.Chem.Phys.* **1988**,92,1476. (e) Baldridge, K.K.; Gordon, M.S.; Steckler, R.; Truhlar, D.G.

J.Chem.Phys. **1989**,93,5107.
(15) (a) Gonzalez, C.; Schlegel, H.B. *J.Chem.Phys.* **1989**,90,2154. (b) Gonzalez, C.; Schlegel, H.B. *J.Phys.Chem.* **1990**,94,5523.
(16) Wachters, A.J.H. *J.Chem.Phys.* **1970**,52,1033.
(17) Rappé, A.K.; Smedley, T.A.; Goddard III, W.A. *J.Phys.Chem.* **1981**,85, 2607.
(18) The standard modifications implemented in the GAMESS code;[26] the resulting basis set is stored as TZV.
(19) Dunning, T.H. *J.Chem.Phys.* **1971**,55,716.
(20) Huzinaga, S. *J.Chem.Phys.* **1965**,42,1293.
(21) (a) Cizek, J. *Adv. Chem.Phys.* **1969**,14,35. (b) Purvis, G.D.; Bartlett, R.J. *J.Chem.Phys.* **1982**,76,1910. (c) Scuseria, G.E.; Janssen, C.L.; Schaefer, H.F. III, *J.Chem.Phys.* **1988**,89,7382. (d) Raghavachari, K.; Trucks, G.W.; Pople, J.A.; Head-Gordon, M. *Chem.Phys.Lett.* **1989**,157,479. (e) Scuseria, G.E.; Schaefer, H.F. III, *J.Chem.Phys.* **1989**,90,3700. (f) Watts, J.D.; Gauss, J.; Bartlett, R.J. *J.Chem.Phys.* **1993**,98,8718. (g) Pople, J.A.; Head-Gordon, M.; Raghavachari, K. *J.Chem.Phys.* **1987**,87,5968.
(22) (a) Frisch M.J.; Trucks G.W.; Schlegel H.B.; Gill P.M.W.; Johnson B.G.; Robb M.A.; Cheeseman J.R.; Keith T.A.; Petersson G.A.; Montgomery J.A.; Raghavachari K.; Al-Laham M.A.; Zakrzewski V.G.; Ortiz J.V.; Foresman J.B.; Cioslowski J.; Stefanov B.B.; Nanayakkara A.; Challacombe M.; Peng C.Y.; Ayala P.Y.; Chen W.; Wong M.W.; Andres J.L.; Replogle E.S.; Gomperts R.; Martin R.L.; Fox D.J.; Binkley J.S.; Defrees D.J; Baker J.; Stewart J.P.; Head-Gordon M.; Gonzalez C.; Pople J.A., Gaussian 94, Gaussian, Inc., Pittsburgh, PA,1995.
(b) Frisch, M.J.; Trucks, G.W.; Head-Gordon, M.; Gill, P.M.W. ; Wong, M.W.; Foresman, J.B.; Johnson, B.G.; Schlegel, H.B.; Robb, M.A.; Replogle, E.S.; Gomperts, R.; Andres, J.L.; Raghavachari, K.; Binkley, J.S.; Gonzalez, C.; Martin, R.L.; Fox, D.J.; DeFrees, D.J.; Baker, J.; Stewart, J.J.P.; Pople, J.A. Gaussian 92/DFT, Gaussian, Inc., Pittsburgh, PA,1993. 'INT=FineGrid' option was used througout.
(23) Raghavachari, K.; Trucks, G.W. *J.Chem.Phys.* **1989**,91,1062.
(24) Hay, P.J. *J.Chem.Phys.* **1977**,66,4377.
(25) The final Ti basis of the form (15s11p6d2f)/[10s7p4d2f] was used in conjunction with the standard Pople's 6-311+G(2d,2p) basis sets for C and H atoms. For the latter basis see, Frisch, M.J.; Pople, J.A.; Binkley, J.S. *J.Chem.Phys.* **1984**,80,3265.
(26) GAMESS (General Atomic and Molecular Electronic Structure System): Schmidt, M.W.; Baldridge, K.K.; Boatz, J.A.; Elbert, S.T.; Gordon, M.S.; Jensen, J.H.; Koseki, S.; Matsunaga, N.; Nguyen, K.A.; Su, S.; Windus, T.L.; Dupuis, M.; Montgomery, Jr., J.A. *J.Comput.Chem.* **1993**,14,1347.
(27) Sugar, J.; Corioliss, C. *J.Phys.Chem.Ref. Data* **1985**,14, Suppl. No. 2.

(28) A recent review article comparing performance of the DFT B3LYP approach against the traditional ab initio methods for transition metal systems can be mentioned here: Siegbahn, P.E.M. In *Advances in Chemical Physics*, Prigogine, I.; Rice, S.A., Eds.; John Wiley & Sons, Inc.: New York, 1996; Vol. XCIII, pp 333-386.
(29) Hehre, W.J.; Radom, L.; Schleyer, P.v.R.; Pople, J.A. *Ab Initio Molecular Orbital Theory* ; John Wiley & Sons, Inc. : New York,1986.
(31) Baker, J.; Muir, M.; Andzelm, J. *J.Chem.Phys.* **1995**,102,2063.
(32) Sodupe, M.; Bauschlicher, C.W.; Langhoff, S.R.; Partridge, H. *J.Phys.Chem.* **1992**,96,2118. Note that the state referred to as $^4B_1$ in the present work is denoted $^4B_2$ by Sodupe et al.
(33) (a) Ricca, A.; Bauschlicher, C.W. *Chem.Phys.Lett.* **1995**,245,150.
(b) Holthausen, M.C.; Koch, W. *Chem.Phys.Lett.* **1995**,240,245.
(c) Bauschlicher, C.W.; Partridge, H.; Sheehy, J.A.; Langhoff, S.R.; Rosi, M. *J.Phys.Chem.* **1992**,96,6969.
(34) We did not find a stationary point corresponding to the η^1 C-H coordination.
(35) The C_{2v} structure with the perpendicular H_2 unit and corresponding to the $^4A_1$ state was 0.6 kcal/mol higher in energy and showed a small imaginary frequency.
(36) This is related to the corresponding spin density distribution of ca. 2.2 and 0.8 on the Ti and C atoms, the latter atom connected to Ti with the longer bond of 2.46 Å. The symmetry breaking related to the insufficient correlation level for the Co analogue, $Co(CH_3)_2^+$, was reported by Perry et al. Perry, J.K.; Goddard III, W.A.; Ohanessian, G. *J.Chem.Phys.* **1992**,97,7560.
(37) (a) Holthausen, M.C.; Fiedler, A.; Schwarz, H.; Koch, W. *J.Phys.Chem.* **1996**,100,6236. (b) Holthausen, M.C.; Koch, W. *J.Am.Chem.Soc.* **1996**,118,9932. DFT B3LYP method was used by these authors for both geometry optimization and energetics.
(38) Perry, J.K.; Ohanessian, G.; Goddard III, W.A. *J.Phys.Chem.* **1993**,97,5238.
(39) H. A. Bethe, E. E. Salpeter, Quantum Mechanics of the one and two electron atoms (Plenum, New York, 1977).
(40) H.Nakamura, J. Chem. Phys. 87, 4031(1987).

Table 1. Relative energies (in kcal/mol) of the Ti^+ (^4F) and Ti^+ (^2F) terms

Method	Ti^+ (^4F, $3d^24s^1$)	Ti^+ (^2F, $3d^24s^1$)
CCSD(T)	0.0	4.0
CASSCF[a,b]	0.0	16.6
DFT B3LYP	0.0	14.3
MCQDPT2	0.0	13.6
Exp.[c]	0.0	13.2

[a]The active space corresponds to the Ti 3d and 4s orbitals. [b]The same basis set was used as in the DFT B3LYP calculations. [c]Ref.27; averaged over J states.

Table 2. Relative energies for the H_2 elimination reaction (in kcal/mol)[a]

	DFT B3LYP	CCSD(T)	MCQDPT2
	$Ti^+ + C_2H_6 \longrightarrow TiC_2H_4^+ + H_2$		
	Doublet		
$Ti^+ + C_2H_6$	14.3		13.6
$Ti^+ \cdots C_2H_6$ (**a**)	-6.2		1.2
C-H ins. TS (**d**)	5.2	9.0	8.0
$HTiC_2H_5^+$ (**e**)	-11.0	-1.7	-10.1
Ti-H rot. TS (**f**)	-6.9	1.9	-10.1
$HTiC_2H_5^+$ (**g**)	-6.8	2.1	-8.2
H_2 elim. TS (**j**)	1.5	9.5	-2.2
$TiC_2H_4^+ \cdots H_2$ (**k**)	-1.8	6.2	-3.6
$TiC_2H_4^+ + H_2$	0.6	7.5	-.3
	Quartet		
$Ti^+ + C_2H_6$	0.0	0.0	0.0
$Ti^+ \cdots C_2H_6$ (**a**)	-20.1	-15.6	-18.1
C-H ins. TS (**d**)	17.3	23.1	17.0
$HTiC_2H_5^+$ (**e**)	17.1	22.1	20.4
Ti-H rot. TS (**f**)	17.1	21.6	
$HTiC_2H_5^+$ (**g**)	16.2	20.6	
H_2 elim. TS (**j**)	21.8	30.9	
$TiC_2H_4^+ \cdots H_2$ (**k**)	-6.8	3.1	-10.4
$TiC_2H_4^+ + H_2$	-1.2	7.7	2.8

[a]All energies are relative to the Ti^+ (^4F) + C_2H_6 ground-state reactants and include the ZPVE corrections.

Table 3. Relative energies for the CH_4 elimination reaction (in kcal/mol)[a]

	DFT B3LYP	CCSD(T)
$Ti^+ + C_2H_6 \longrightarrow TiCH_2^+ + CH_4$		
	Doublet	
$Ti^+ + C_2H_6$	14.3	
$Ti^+ \cdots C_2H_6$ (**a**)	-6.2	
C-H ins. TS (**d**)	5.2	9.0
$HTiC_2H_5^+$ (**e**)	-11.0	-1.7
C-C ins. TS (**b**)	16.7	25.0
$Ti(CH_3)_2^+$ (**c**)	-22.1	-11.6
1,3 H shift TS (**h**)	8.1	15.1
$TiCH_2^+ \cdots CH_4$ (**i**)	-3.4	1.9
$TiCH_2^+ + CH_4$	11.0	17.0
	Quartet	
$Ti^+ + C_2H_6$	0.0	0.0
$Ti^+ \cdots C_2H_6$ (**a**)	-20.1	-15.6
$Ti(CH_3)_2^+$ (**c**)	11.0	18.3
1,3 H shift TS (**h**)	26.9	36.0
$TiCH_2^+ \cdots CH_4$ (**i**)	6.0	12.7
$TiCH_2^+ + CH_4$	19.4	25.6

[a]All energies are relative to the Ti^+ (^4F) + C_2H_6 ground-state reactants and include the ZPVE corrections.

Captions to Figures

Figure 1.

Structures of (a) C_2H_6 reactant, (b) H_2 elimination products, and (c) CH_4 elimination products of C_2H_6 by Ti^+ (bond lengths in Å, bond angles in degrees). H bend denotes the out-of-plane bending angle of the hydrogen atoms (zero for the isolated C_2H_4). Values in parentheses are from experiment (taken from Ref. 29).

Figure 2.

Plausible structures of the electrostatic complex $Ti^+\cdots C_2H_6$ formed in the first step of the reaction between Ti^+ and C_2H_6 (bond lengths in Å, bond angle in degrees).

Figure 3.

Doublet structures for the reaction between Ti^+ and C_2H_6 (bond lengths in Å, bond angles in degrees).

Figure 4.

Quartet structures for the reaction between Ti^+ and C_2H_6 (bond lengths in Å, bond angles in degrees).

Figure 5.

The energy profiles for the $Ti^+ + C_2H_6 \longrightarrow TiC_2H_4^+ + H_2$ reaction calculated at the (a) DFT B3LYP and (b) CCSD(T) level.

Figure 6.

The energy profiles for the $Ti^+ + C_2H_6 \longrightarrow TiCH_2^+ + CH_4$ reaction calculated at the (a) DFT

B3LYP and (b) CCSD(T) level.

Figure 7.

Energy and SOCC along the doublet IRC from the complex **d** in the direction of complex **a**.

Figure 8.

Energy and SOCC along the quartet IRC from the complex **d** in the direction of complex **a**.

Figure 9.

Energy and SOCC along the averaged IRC from the complex **d** in the direction of complex **a**.

Figure 10.

Energy levels at the crossing (along the averaged IRC), r_{C-H}=1.698Å.

Figure 11.

Transition probability at the doublet/quartet crossing.

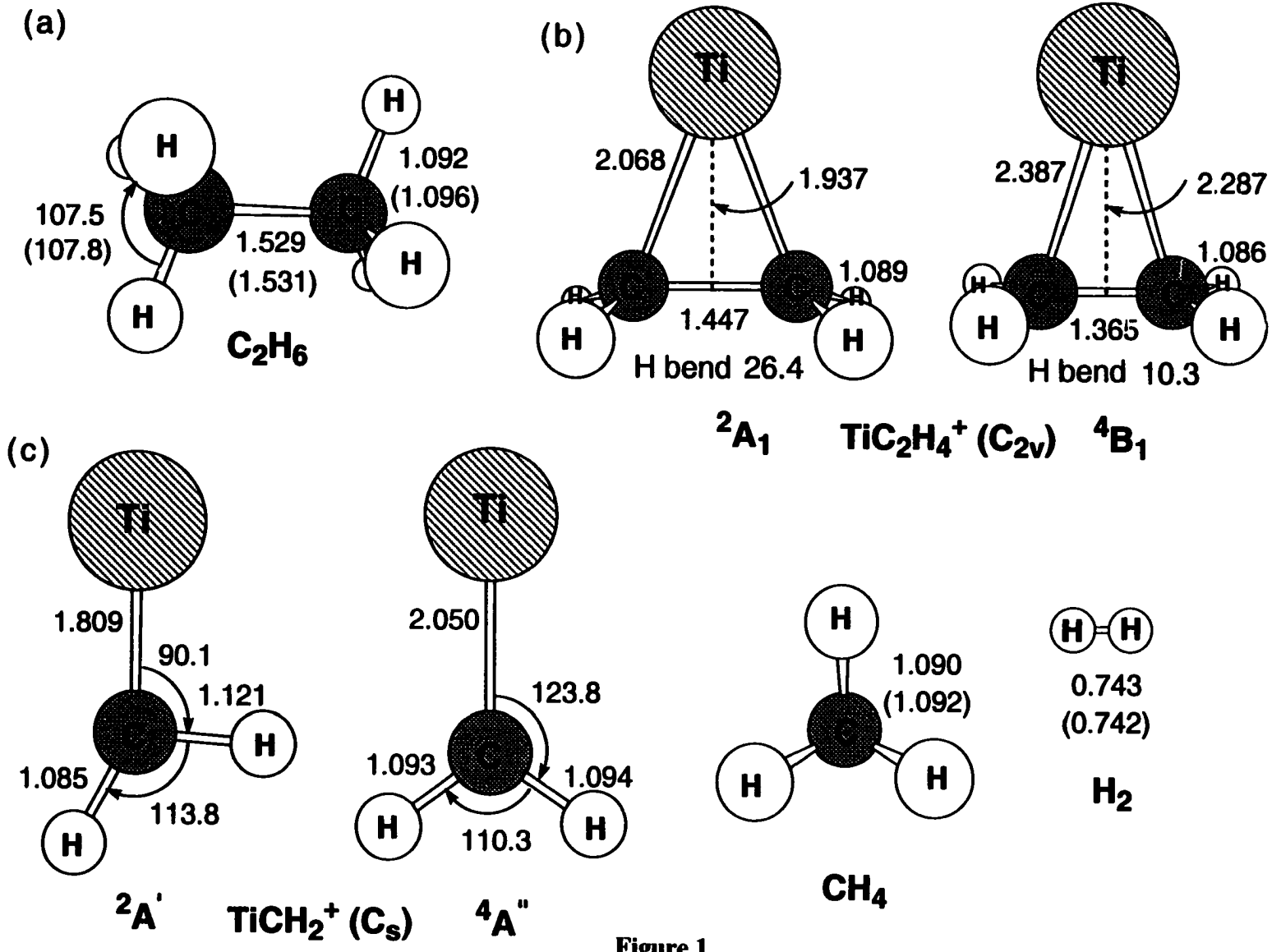
(a)
H
H
H
H
1.092
(1.096)
107.5
(107.8)
1.529
(1.531)
C2H6
(b)
Ti
2.068
1.937
1.089
1.447
H
H
H bend 26.4
2A1
Ti
2.387
2.287
1.086
H
H
1.365
H
H bend 10.3
TiC2H4+ (C2v)
4B1
(c)
Ti
1.809
90.1
1.121
H
1.085
113.8
H
2A'
TiCH2+ (Cs)
Ti
2.050
123.8
1.093
1.094
H
H
110.3
4A"
H
H
1.090
(1.092)
H
H
CH4
H H
0.743
(0.742)
H2

Figure 1.

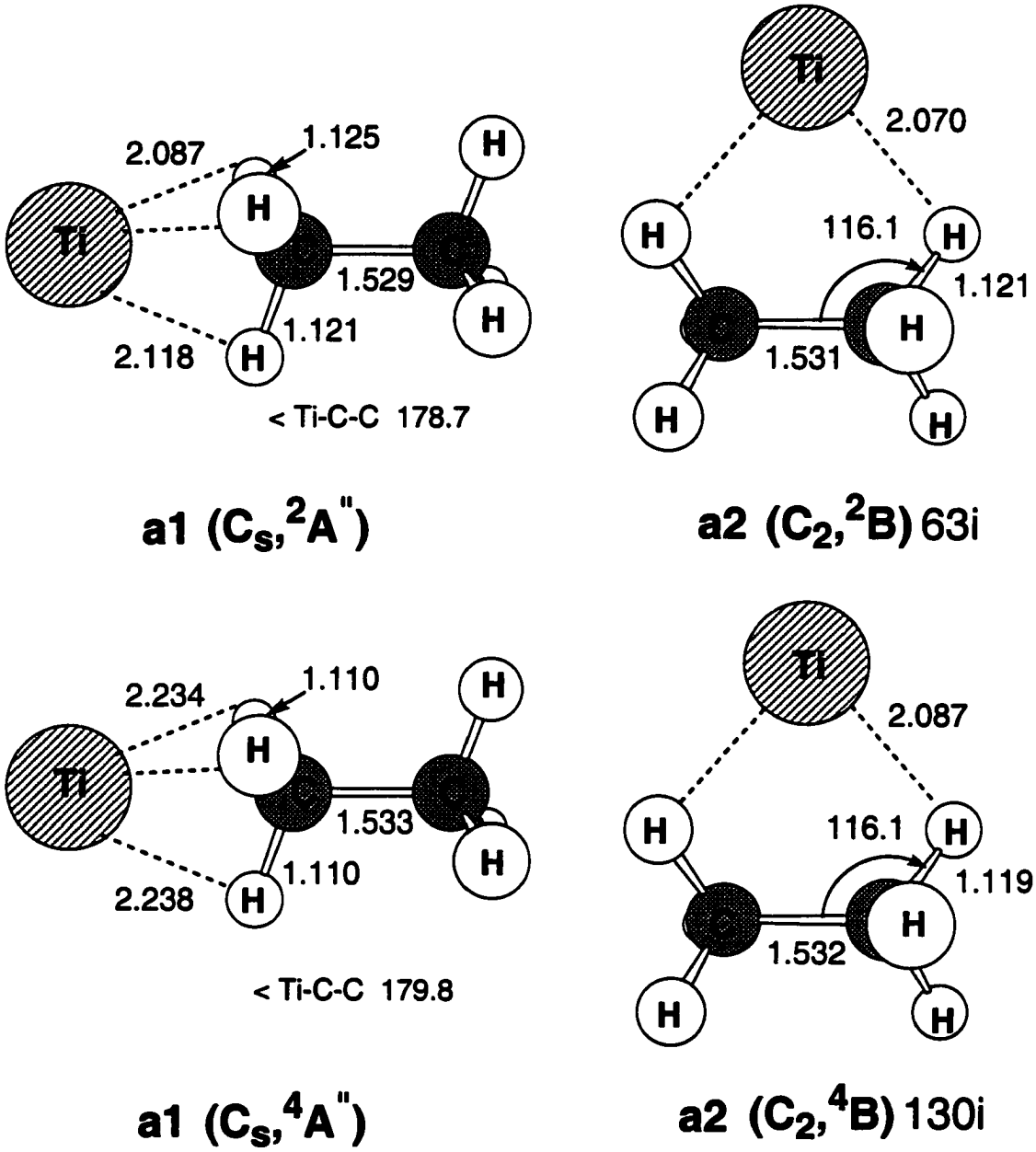
2.087
1.125
H
Ti
H
1.529
H
1.121
2.118
H
< Ti-C-C 178.7
a1 (C_s,^{2}A")
Ti
2.070
H
116.1
H
1.121
H
1.531
H
H
a2 (C_2,^{2}B) 63i
2.234
1.110
H
Ti
H
1.533
H
1.110
2.238
H
< Ti-C-C 179.8
a1 (C_s,^{4}A")
Ti
2.087
H
116.1
H
1.119
H
1.532
H
H
a2 (C_2,^{4}B) 130i

Figure 2.

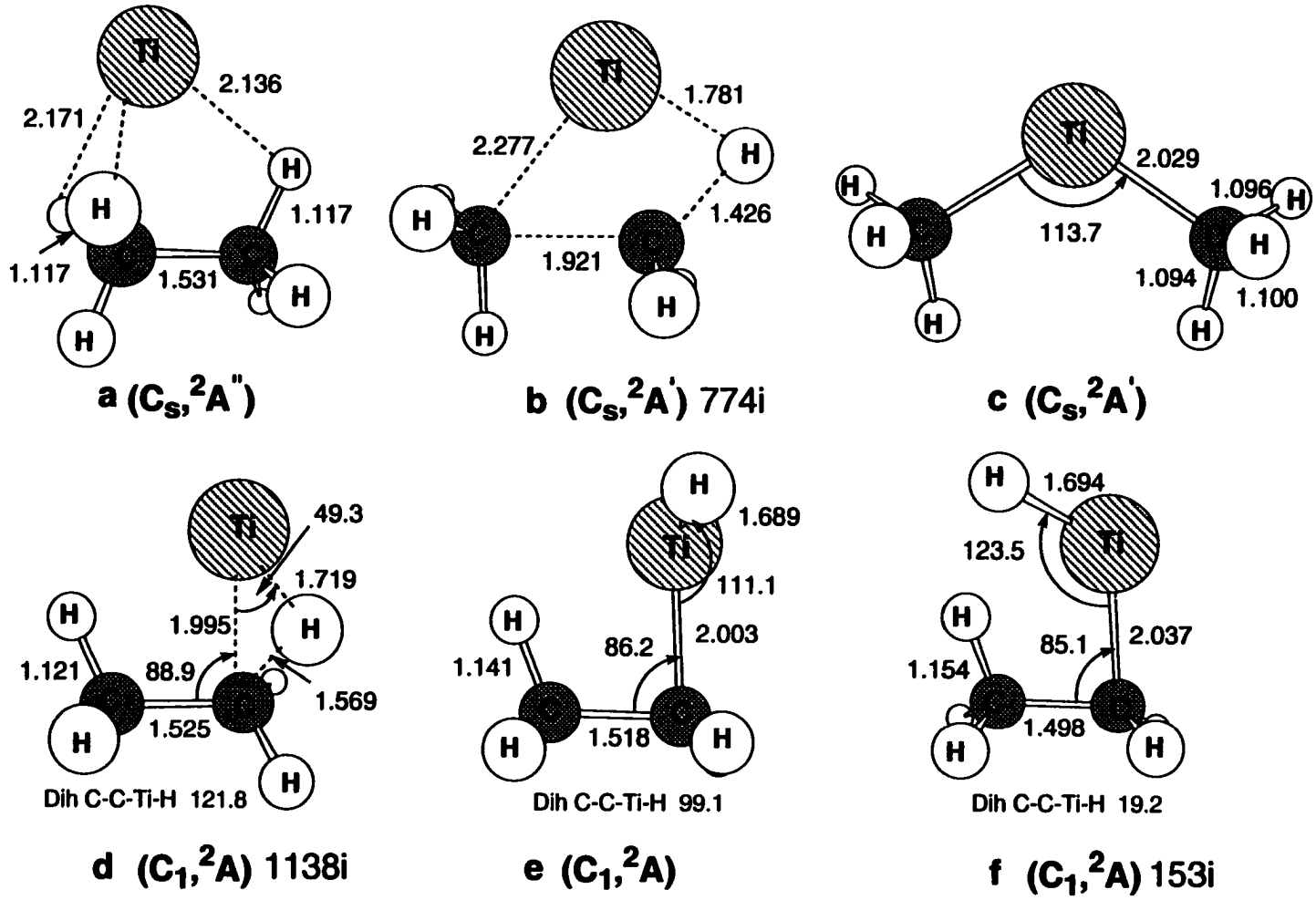
Ti
2.136
2.171
H
1.117
1.117
1.531
H
H
a (C_s,^{2}A")
Ti
1.781
2.277
H
1.426
H
1.921
H
H
b (C_s,^{2}A') 774i
Ti
2.029
H
1.096
H
113.7
H
H
1.094
1.100
H
c (C_s,^{2}A')
Ti
49.3
1.719
1.995
H
H
1.121
88.9
1.569
1.525
H
H
Dih C-C-Ti-H 121.8
d (C_1,^{2}A) 1138i
H
1.689
Ti
111.1
H
86.2
2.003
1.141
H
1.518
H
Dih C-C-Ti-H 99.1
e (C_1,^{2}A)
H
1.694
123.5
Ti
H
85.1
2.037
1.154
1.498
H
H
Dih C-C-Ti-H 19.2
f (C_1,^{2}A) 153i

Figure 3.

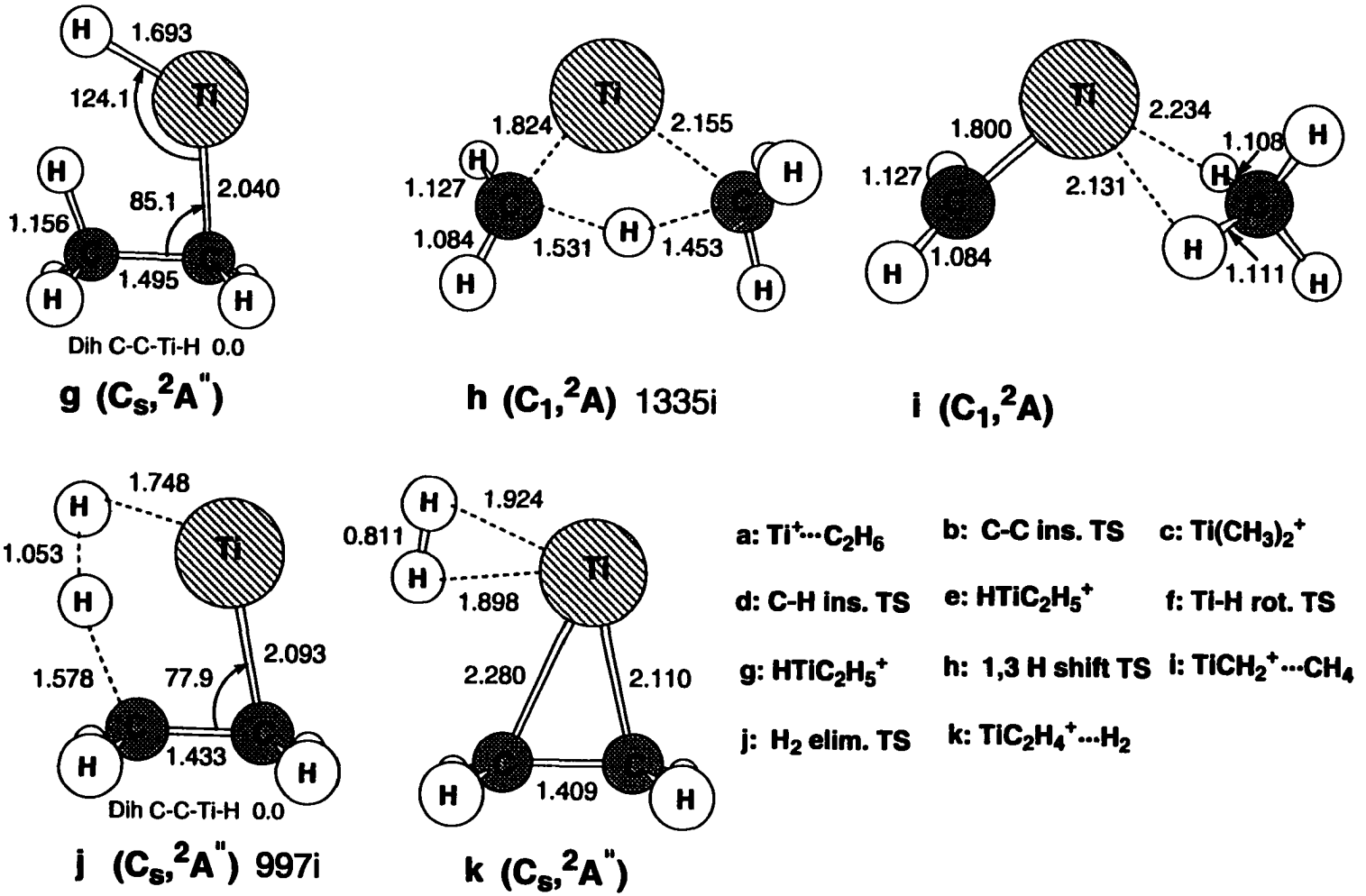

Figure 3 (continued).

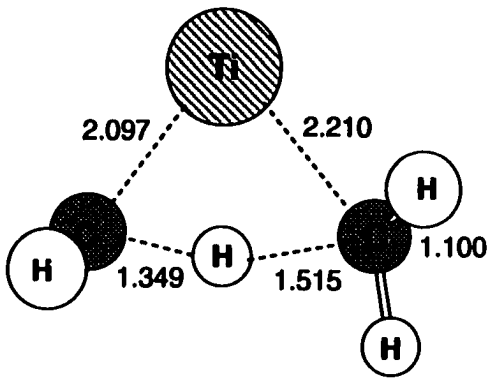

h (C_s,$^4A''$) 1130i

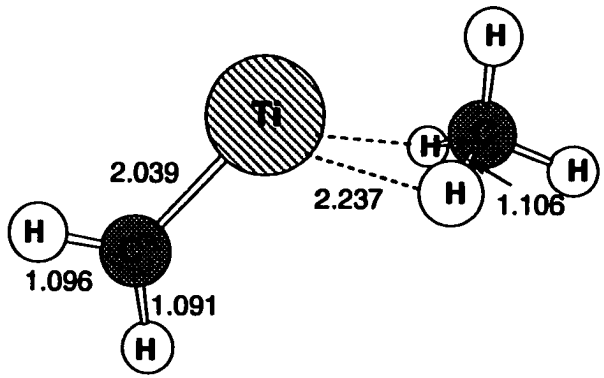

i (C_s,$^4A''$)

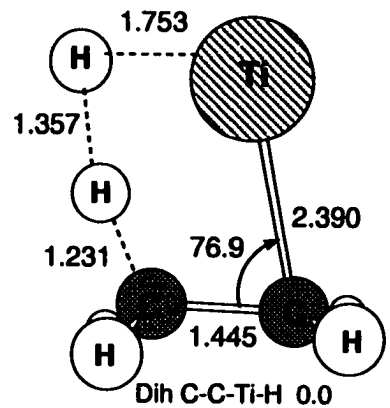

j (C_s,$^4A''$) 840i

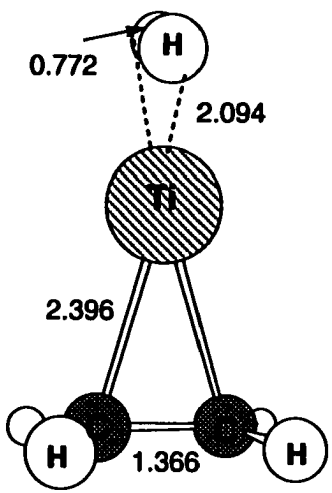

k (C_{2v},$^4A_2$)

a: $Ti^+\cdots C_2H_6$ c: $Ti(CH_3)_2^+$ d: C-H ins. TS

e: $HTiC_2H_5^+$ f: Ti-H rot. TS g: $HTiC_2H_5^+$

h: 1,3 H shift TS i: $TiCH_2^+\cdots CH_4$ j: H_2 elim. TS

k: $TiC_2H_4^+\cdots H_2$

Figure 4 (continued).

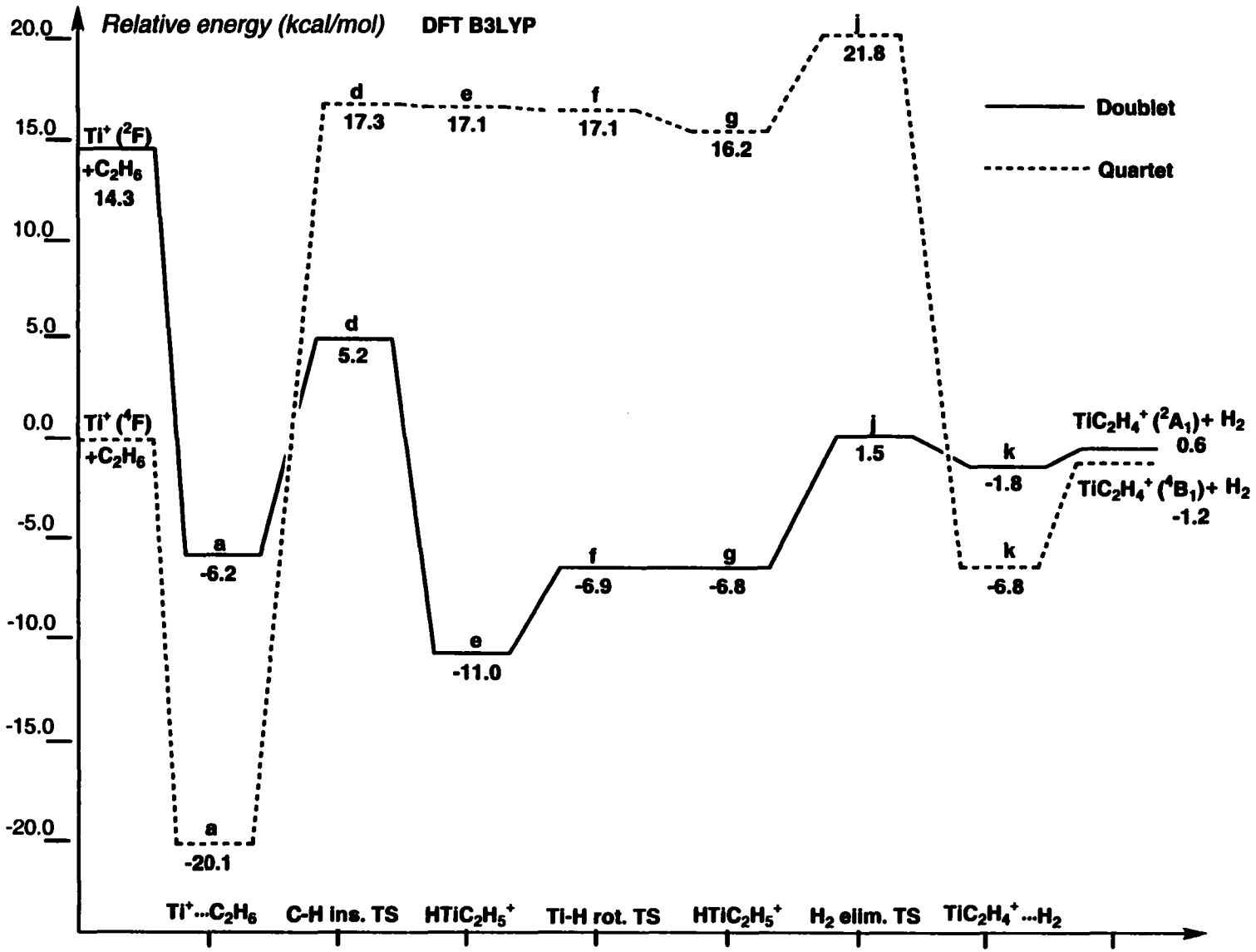
Relative energy (kcal/mol)
DFT B3LYP
20.0
15.0
10.0
5.0
0.0
-5.0
-10.0
-15.0
-20.0
Doublet
Quartet
Ti+ (2F)
+C2H6
14.3
Ti+ (4F)
+C2H6
a
-6.2
a
-20.1
d
17.3
d
5.2
e
17.1
e
-11.0
f
17.1
f
-6.9
g
16.2
g
-6.8
i
21.8
i
1.5
k
-1.8
k
-6.8
TiC2H4+ (2A1)+ H2
0.6
TiC2H4+ (4B1)+ H2
-1.2
Ti+...C2H6
C-H ins. TS
HTiC2H5+
Ti-H rot. TS
HTiC2H5+
H2 elim. TS
TiC2H4+...H2

Figure 5a.

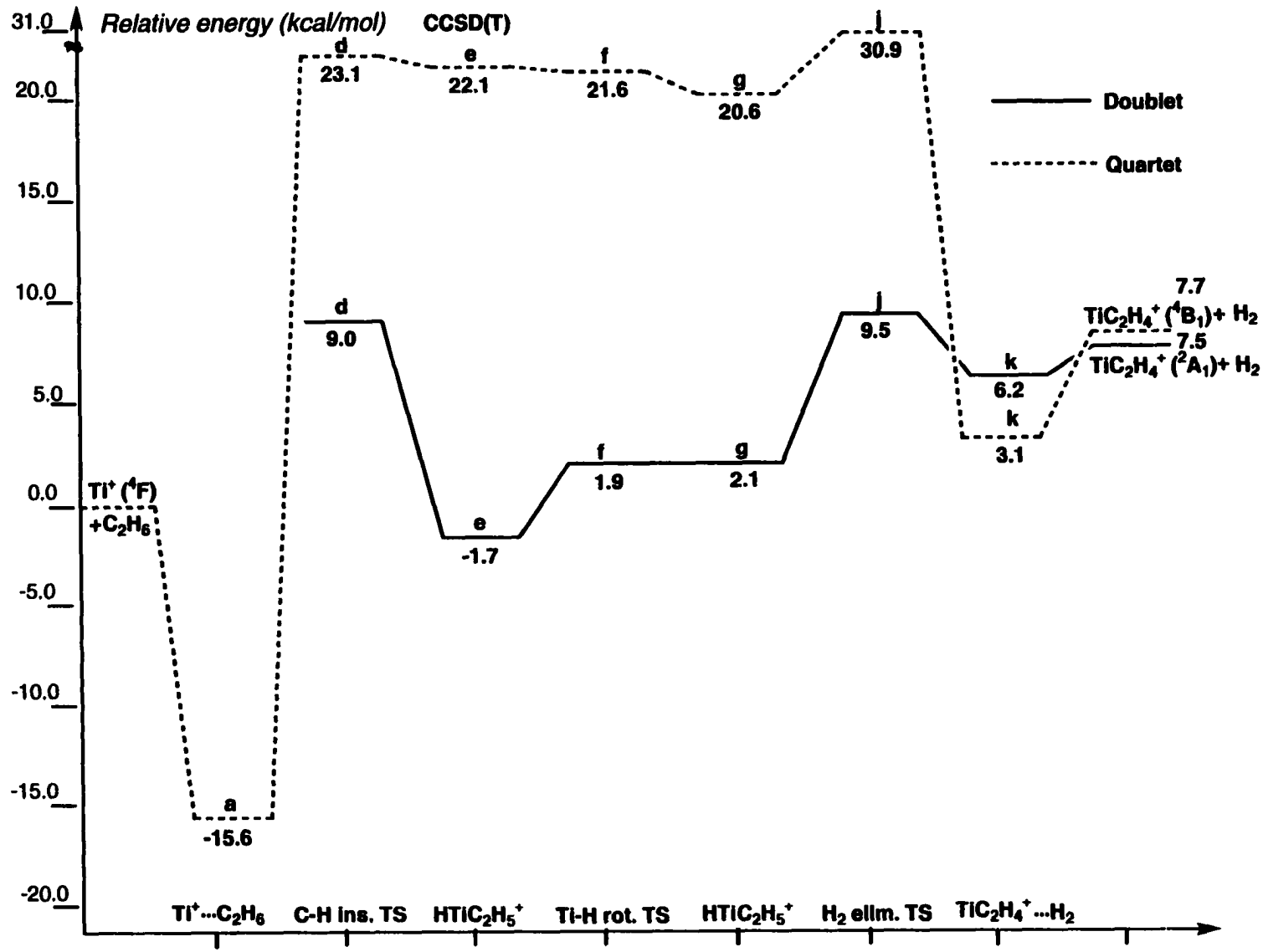
Relative energy (kcal/mol) CCSD(T)
31.0
20.0
15.0
10.0
5.0
0.0
-5.0
-10.0
-15.0
-20.0
Doublet
Quartet
Ti+ (4F)
+C2H6
a
-15.6
d
23.1
e
22.1
f
21.6
g
20.6
l
30.9
d
9.0
e
-1.7
f
1.9
g
2.1
l
9.5
k
6.2
k
3.1
7.7
TiC2H4+ (4B1)+ H2
7.5
TiC2H4+ (2A1)+ H2
Ti+···C2H6
C-H ins. TS
HTiC2H5+
Ti-H rot. TS
HTiC2H5+
H2 elim. TS
TiC2H4+···H2

Figure 5b.

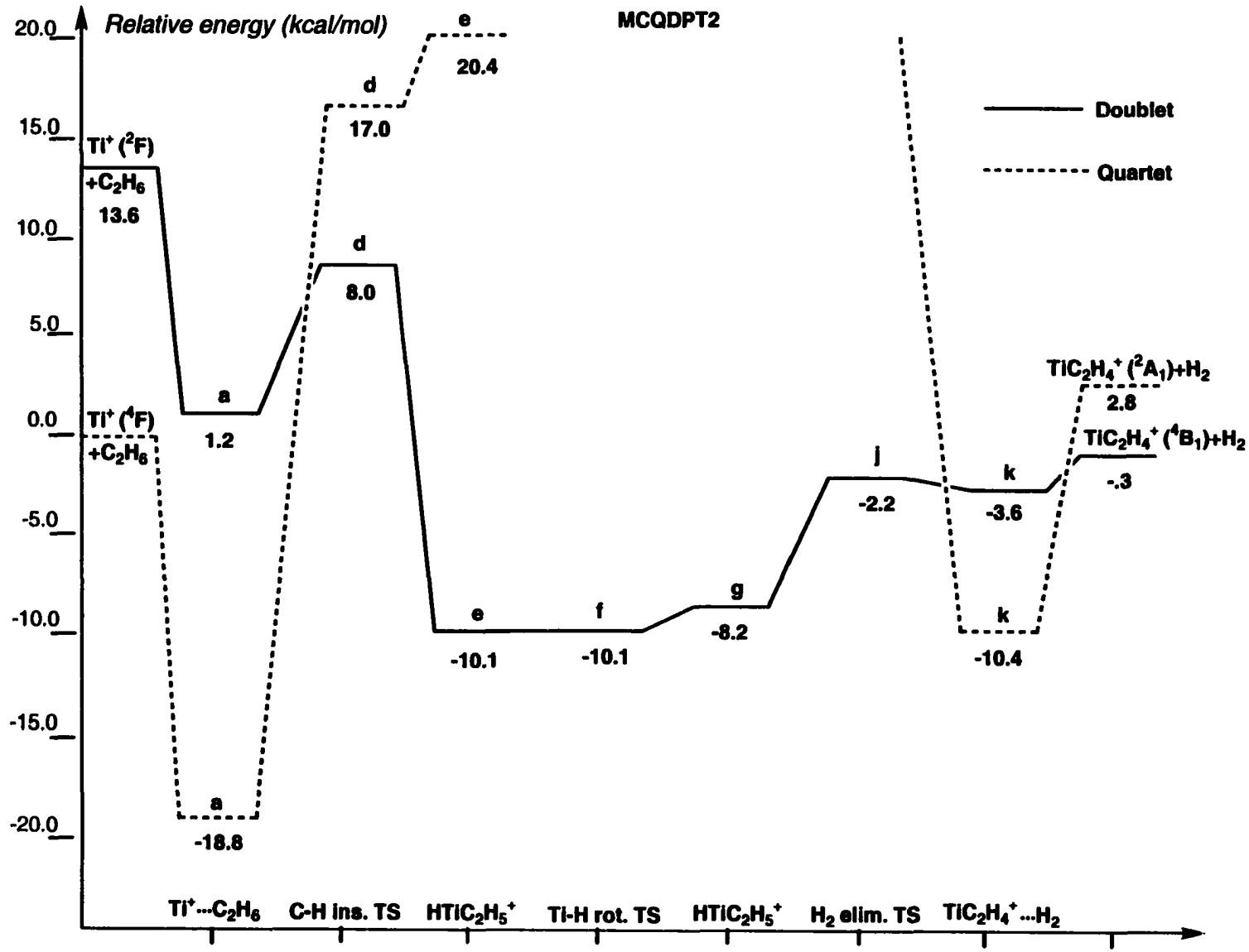
Relative energy (kcal/mol)
MCQDPT2
Doublet
Quartet
20.0
15.0
10.0
5.0
0.0
-5.0
-10.0
-15.0
-20.0
Ti+ (2F)
+C2H6
13.6
Ti+ (4F)
+C2H6
a
1.2
a
-18.8
d
17.0
e
20.4
d
8.0
e
-10.1
f
-10.1
g
-8.2
j
-2.2
k
-3.6
k
-10.4
TiC2H4+ (2A1)+H2
2.8
TiC2H4+ (4B1)+H2
-.3
Ti+...C2H6
C-H ins. TS
HTiC2H5+
Ti-H rot. TS
HTiC2H5+
H2 elim. TS
TiC2H4+...H2

Figure 5c.

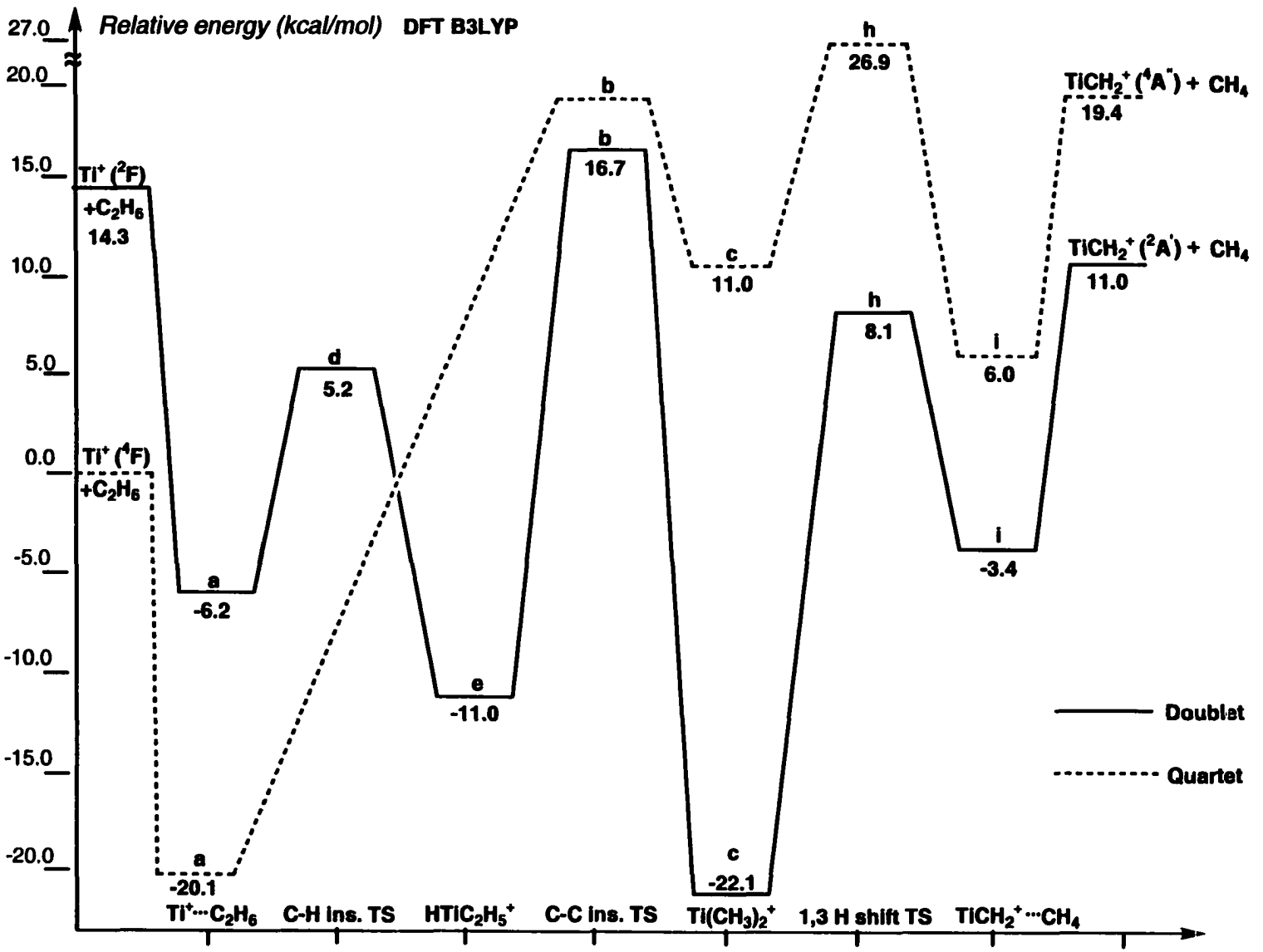
Relative energy (kcal/mol) DFT B3LYP
27.0
20.0
15.0
10.0
5.0
0.0
-5.0
-10.0
-15.0
-20.0
Ti+ (2F)
+C2H6
14.3
Ti+ (4F)
+C2H6
a
-6.2
a
-20.1
d
5.2
e
-11.0
b
16.7
b
c
11.0
c
-22.1
h
26.9
h
8.1
i
6.0
i
-3.4
TiCH2+ (4A") + CH4
19.4
TiCH2+ (2A') + CH4
11.0
Doublet
Quartet
Ti+···C2H6
C-H ins. TS
HTiC2H5+
C-C ins. TS
Ti(CH3)2+
1,3 H shift TS
TiCH2+···CH4

Figure 6a.

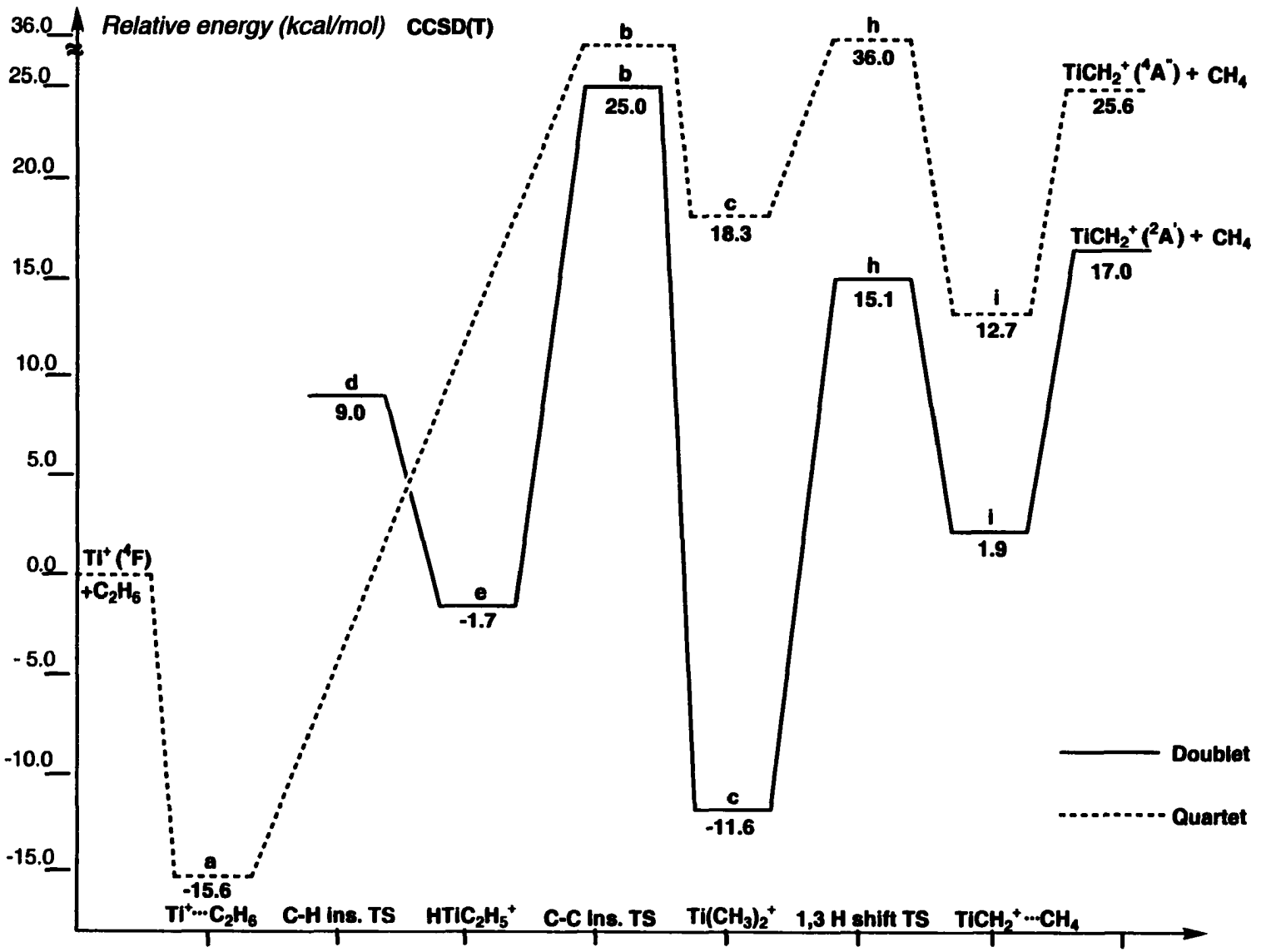
Relative energy (kcal/mol) CCSD(T)
36.0
25.0
20.0
15.0
10.0
5.0
0.0
- 5.0
-10.0
-15.0
Ti+ (4F)
+C2H6
a
-15.6
b
25.0
b
c
18.3
d
9.0
e
-1.7
c
-11.6
h
15.1
h
36.0
i
12.7
i
1.9
TiCH2+ (4A") + CH4
25.6
TiCH2+ (2A') + CH4
17.0
Doublet
Quartet
Ti+···C2H6
C-H ins. TS
HTiC2H5+
C-C ins. TS
Ti(CH3)2+
1,3 H shift TS
TiCH2+···CH4

Figure 6b.

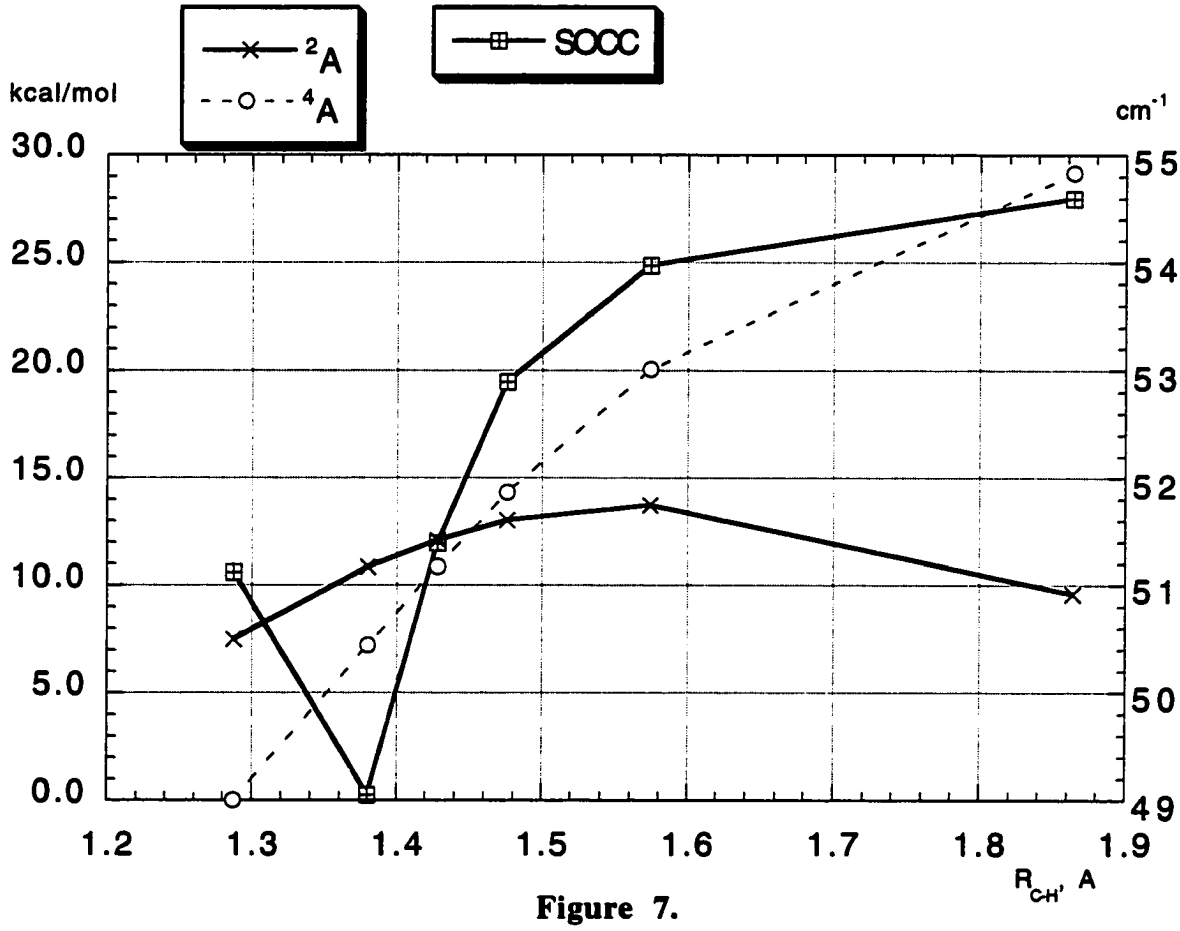
^2A
^4A
SOCC
kcal/mol
cm^{-1}
30.0
25.0
20.0
15.0
10.0
5.0
0.0
55
54
53
52
51
50
49
1.2
1.3
1.4
1.5
1.6
1.7
1.8
1.9
R_{C-H}, A

Figure 7.

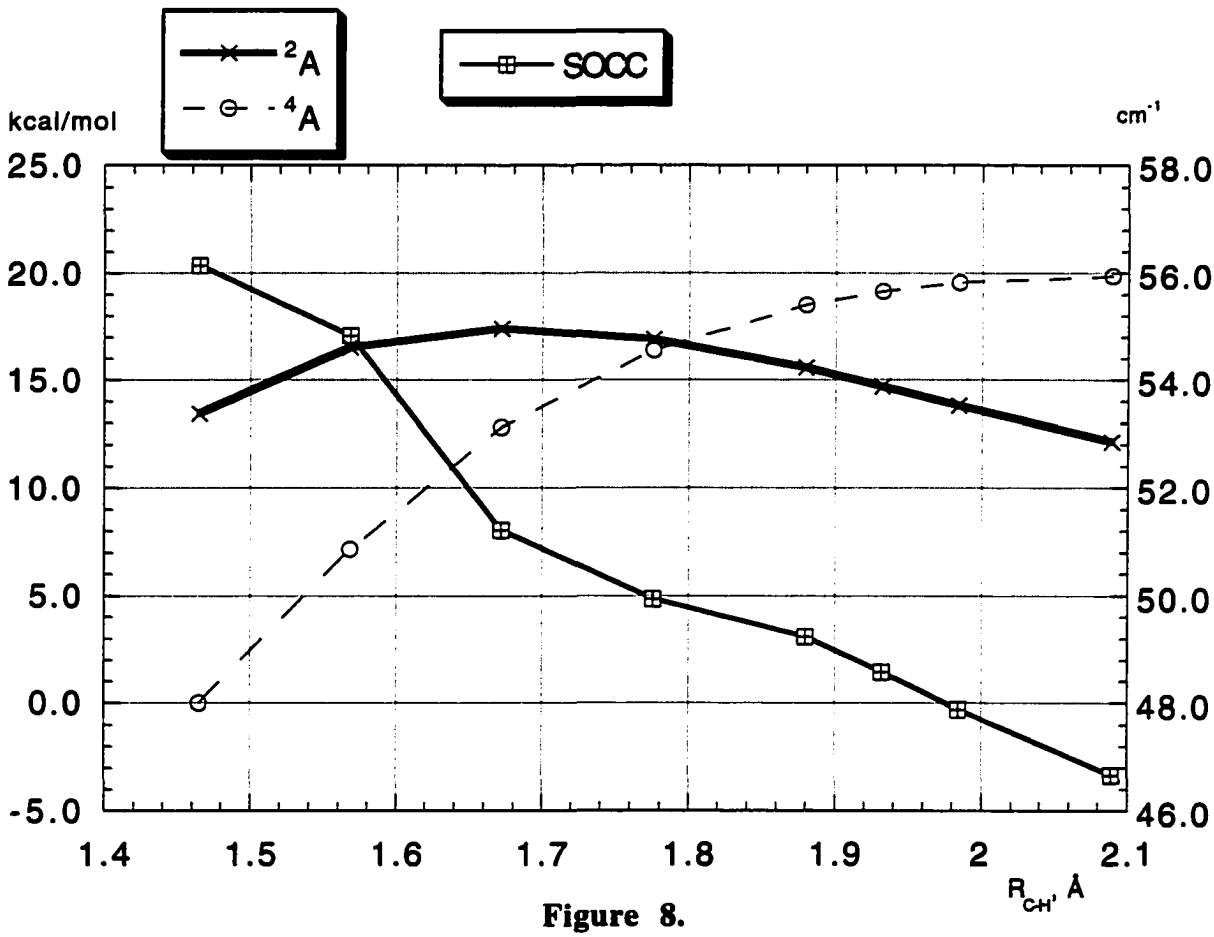
^{2}A
^{4}A
SOCC
kcal/mol
cm^{-1}
25.0
20.0
15.0
10.0
5.0
0.0
-5.0
58.0
56.0
54.0
52.0
50.0
48.0
46.0
1.4
1.5
1.6
1.7
1.8
1.9
2
2.1
$R_{C-H'}$ Å

Figure 8.

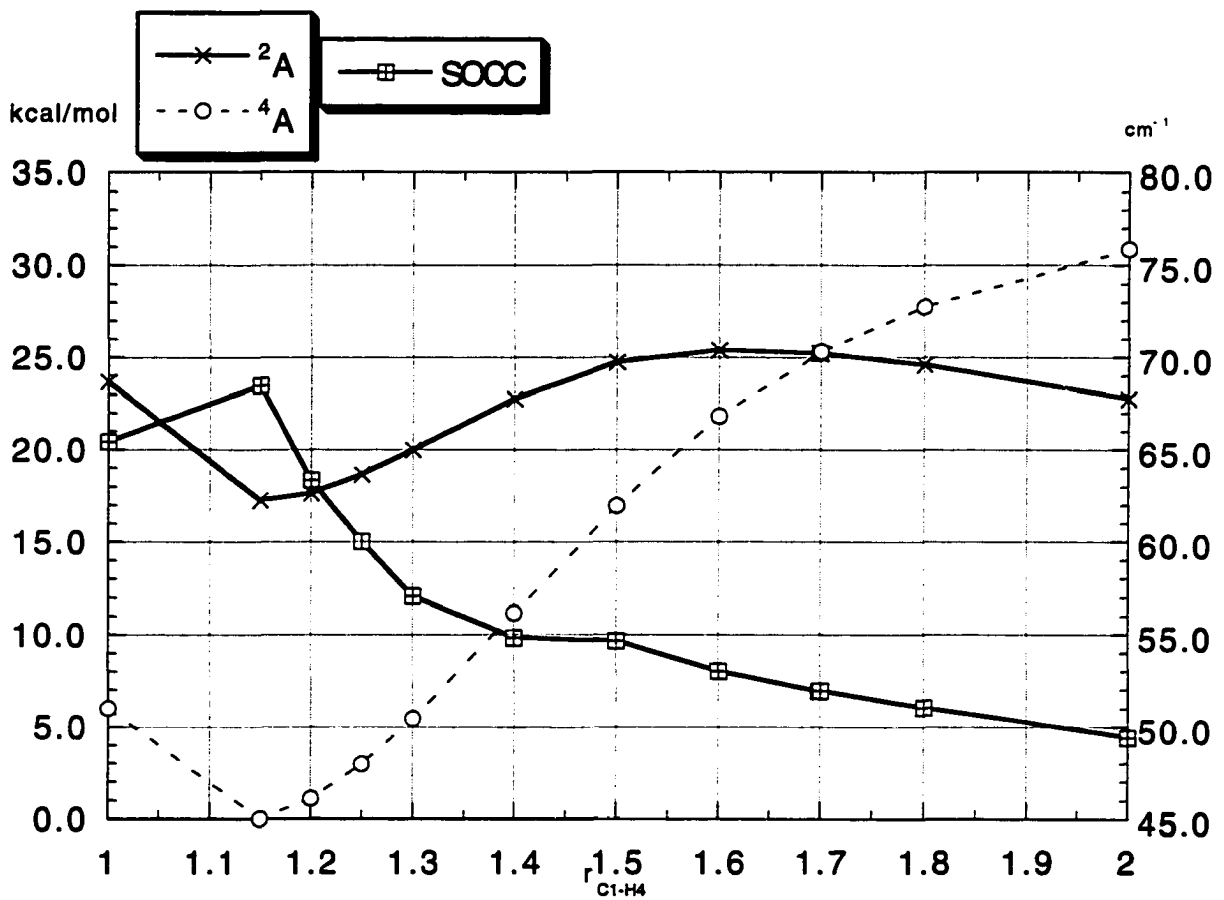
^{2}A
SOCC
^{4}A
kcal/mol
cm^{-1}
35.0
30.0
25.0
20.0
15.0
10.0
5.0
0.0
80.0
75.0
70.0
65.0
60.0
55.0
50.0
45.0
1
1.1
1.2
1.3
1.4
1.5
1.6
1.7
1.8
1.9
2
r C1-H4

Figure 9.

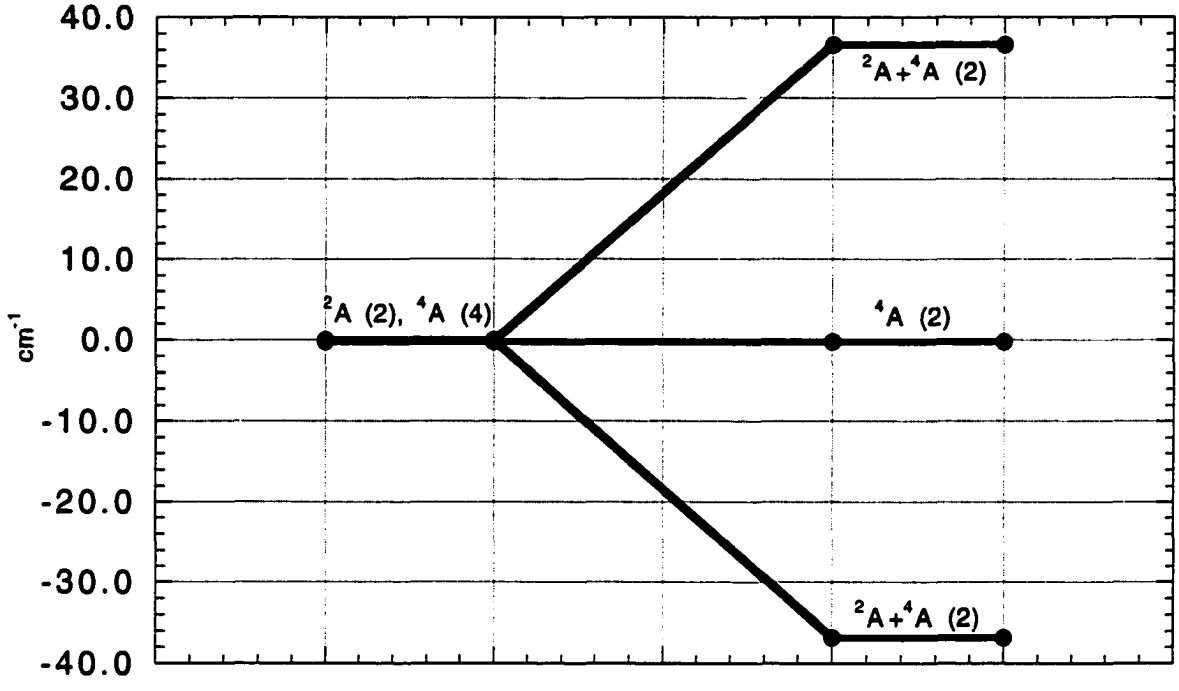

Figure 10.

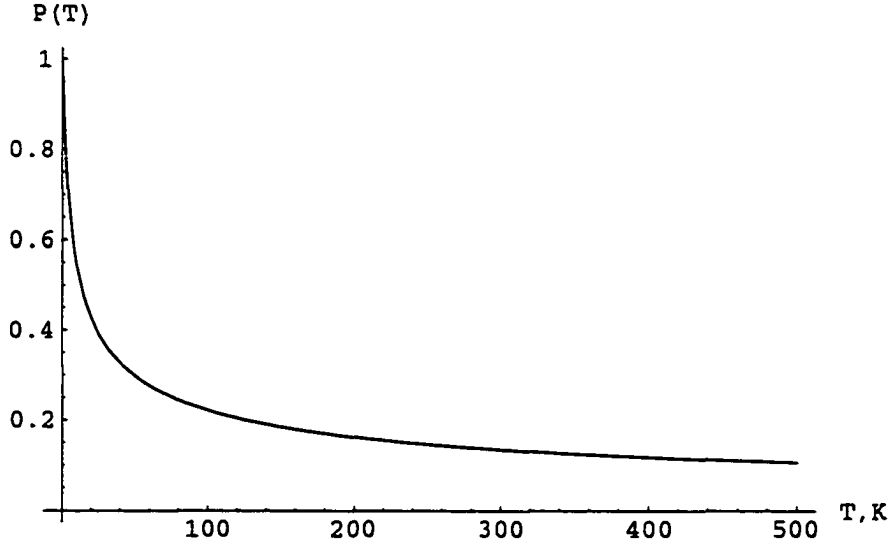

Figure 11.

CHAPTER VIII. GENERAL CONCLUSIONS

The theoretical models discussed in Chapter I have been developed to facilitate studies of spin-dependent processes in chemistry. The models have been put into the publicly available quantum chemistry package GAMESS in order to provide chemists with a convenient tool to study chemical problems without having to resort to solving complicated theoretical and programming difficulties. The models developed in Chapter II underwent laborious testing on a representative set of molecules in order to understand applicability and limitations of the developed models. These simple test cases are to serve as guidelines for future practical applications. Both theoretical models and the developed symmetry apparatus were found to provide satisfying results. The symmetry benefits discussed in Chapter III are very important from the point of view of a manifold increase in efficiency of the code and from the point of view of classification of the results, not an unimportant issue in itself.

A new mechanism for highly accurate studies of vibrational structure of molecular properties was proposed and discussed in Chapter IV. Chapter V summarises some relations and provides proofs for equations used in other parts of the thesis. Two chemically interesting applications were investigated in Chapter VI and VII, further confirming the validity and accuracy of the theoretical models. The future developments may involve developing a theoretical model and practical computational tools for studying the dynamics of molecular processing involving transitions between potential energy surfaces driven by spin-orbit coupling and other diabatic potentials. Undoubtedly a very desirable addition to the existing models would be an inclusion of spin-free relativistic corrections so that all-electron basis sets for transition and heavier main group elements may be used providing superior quality results as compared to widely used effective core potentials. These corrections would also facilitate the full one and two-electron spin-orbit coupling

calculations. The developed vibrational wavefunction mechanism can be used to couple vibrational and electronic wavefunction by the spin-orbit coupling potential so that finer features revealed from both experiments and simpler theoretical models. It is gratifying to be able to theoretically predict finer and finer structure of molecular properties as both theoretical models and computational capabilities improve.

A possible improvement in the future may be the addition of the scalar relativistic corrections to the non-relativistic calculations. This would provide a great improvement for the use of all-electron basis sets for heavier elements in the periodic table, as an alternative for the use of effective core potentials.